Self-Assembled Redox-Active Tetraruthenium Macrocycles with Large Intracyclic Cavities

Daniel Fink,[†] Nicole Orth,[‡] Viktoria Ebel,[†] Franciska S. Gogesch,[†] Anne Staiger,[†] Michael Linseis,[†] Ivana Ivanović-Burmazović[‡] and Rainer F. Winter*[,†]

[†] Fachbereich Chemie, Universität Konstanz, Universitätsstraße 10, 78457 Konstanz, Germany

[‡] Department Chemie und Pharmazie, Friedrich-Alexander-Universität Erlangen-Nürnberg, Egerlandstraße 1, 91058 Erlangen, Germany

Supporting Information

NMR Spectra

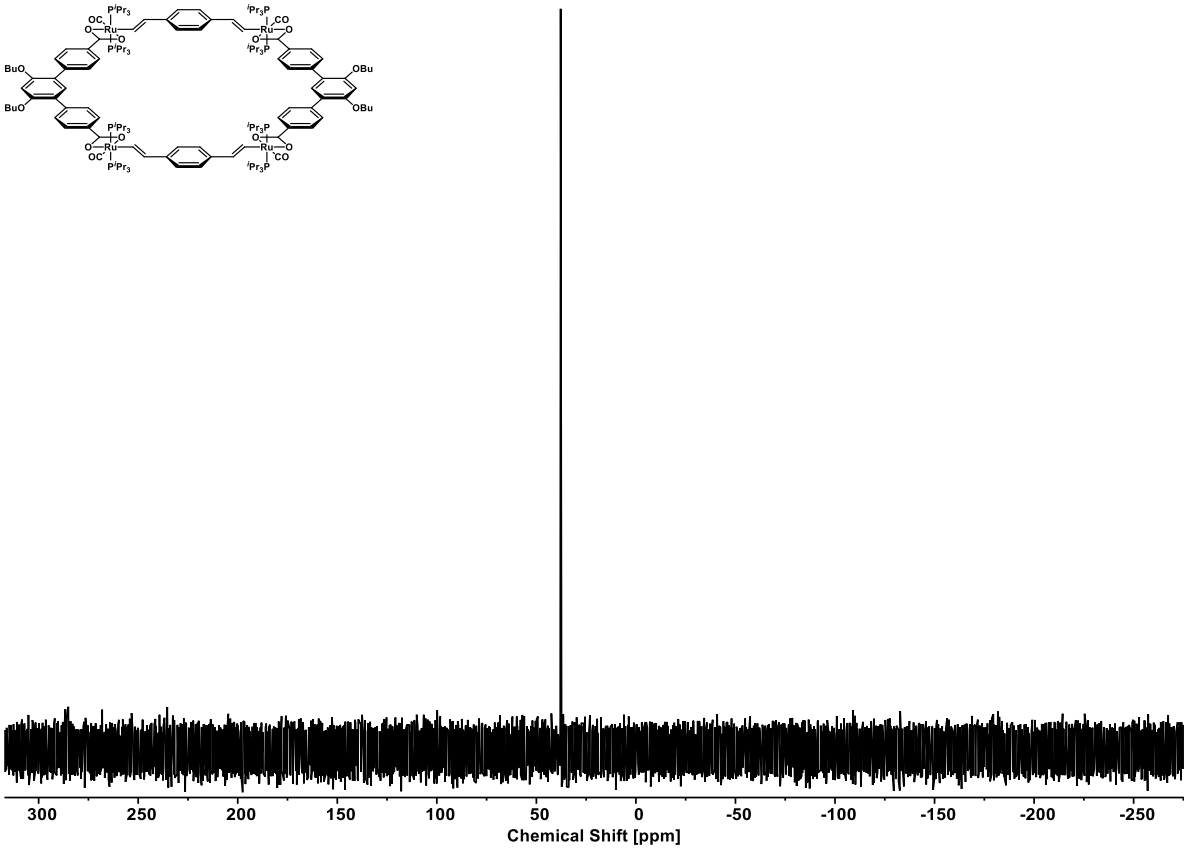

Figure S1. $^{31}P\{^{1}H\}$ NMR spectrum of macrocycle **2-BT**.

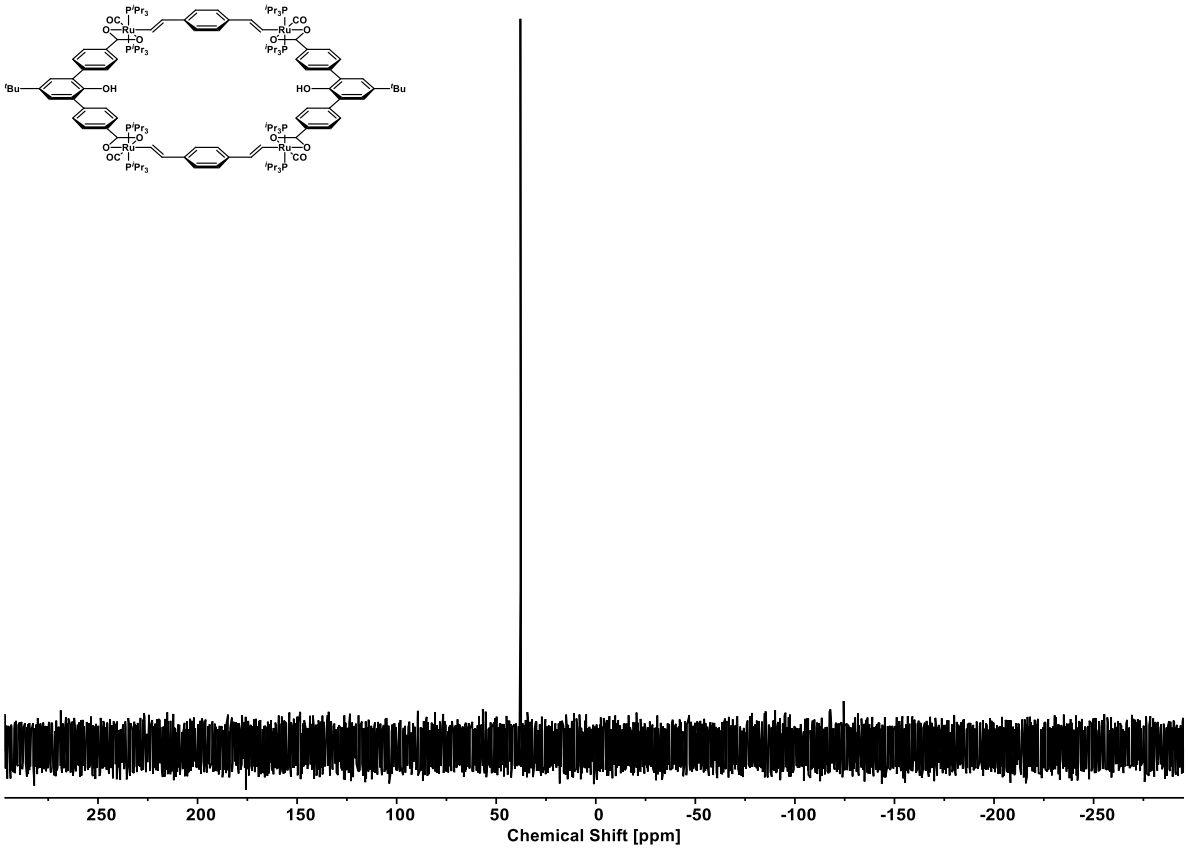

Figure S2. $^{31}P\{^{1}H\}$ NMR spectrum of macrocycle **2-BTO**.

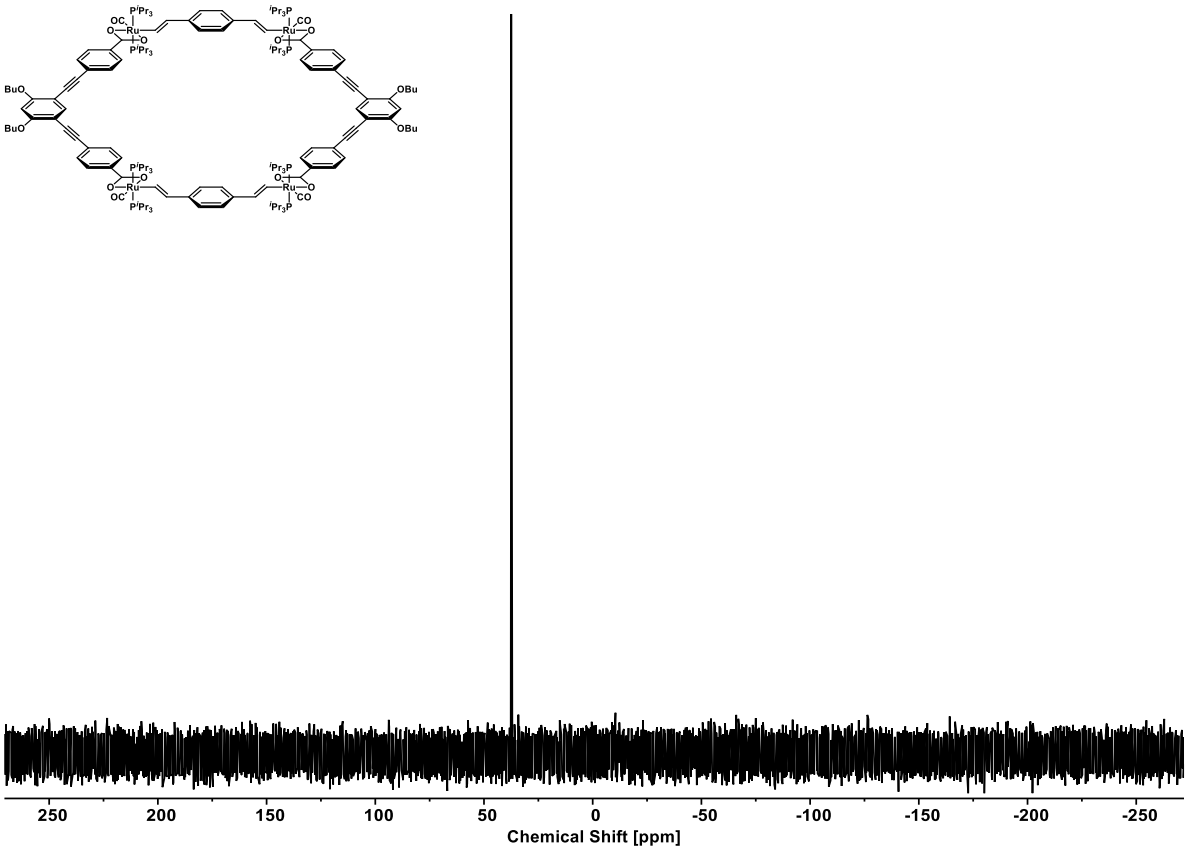

Figure S3. $^{31}P\{^{1}H\}$ NMR spectrum of macrocycle **2-BTE**.

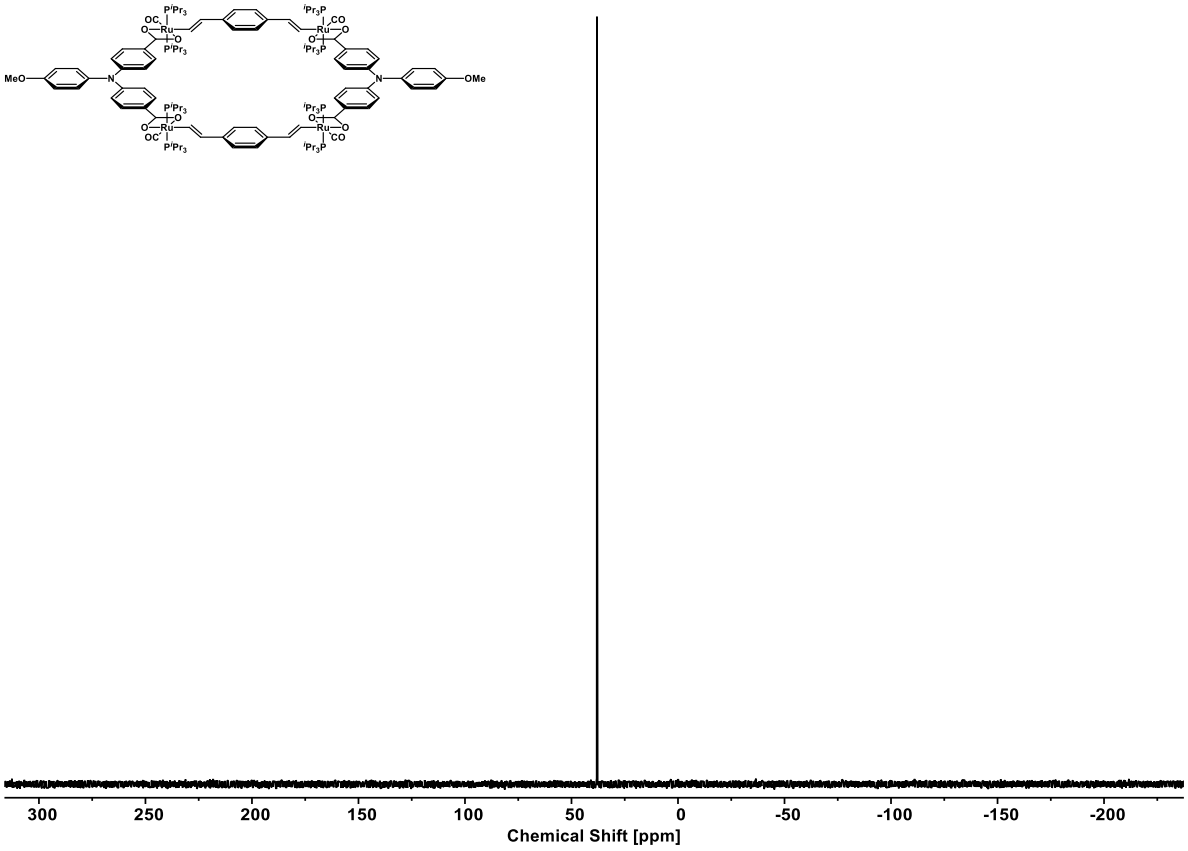

Figure S4. $^{31}P\{^{1}H\}$ NMR spectrum of macrocycle **2-BN**.

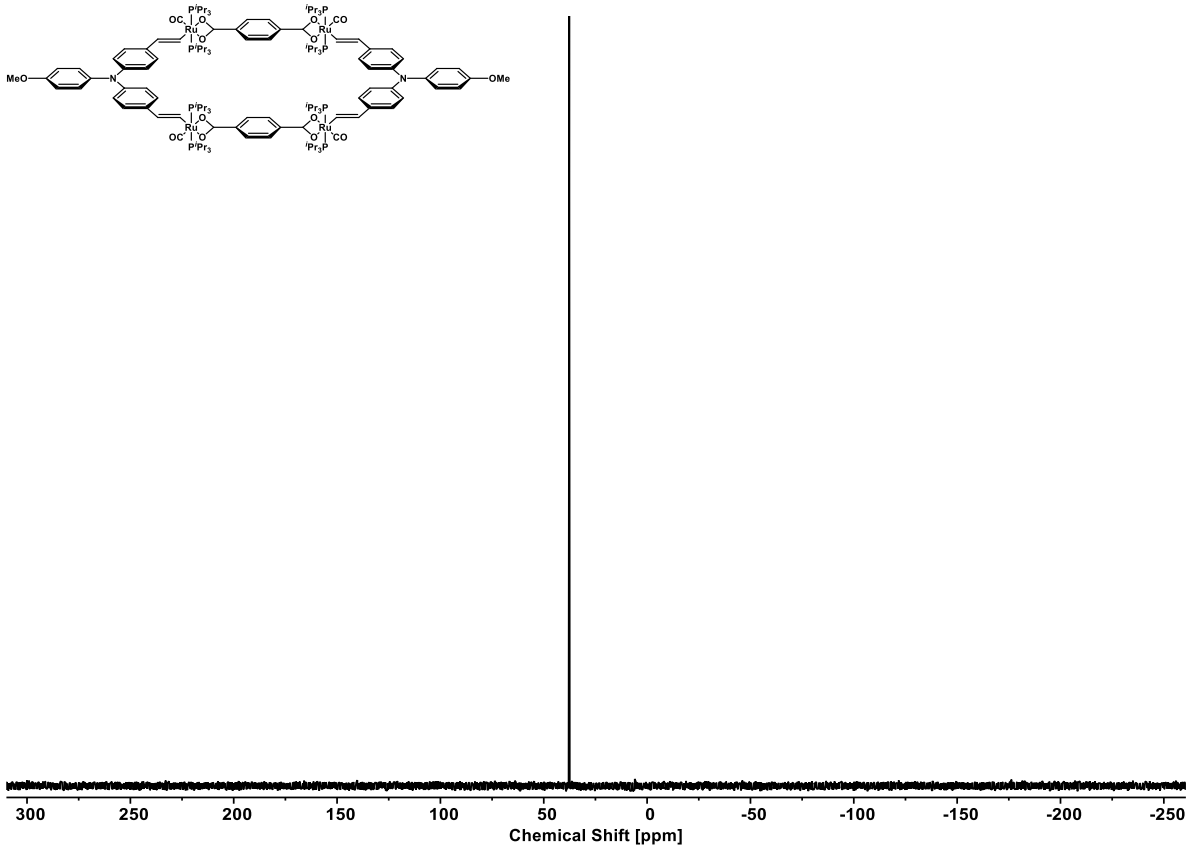

Figure S5. $^{31}P\{^{1}H\}$ NMR spectrum of macrocycle **2-NB**.

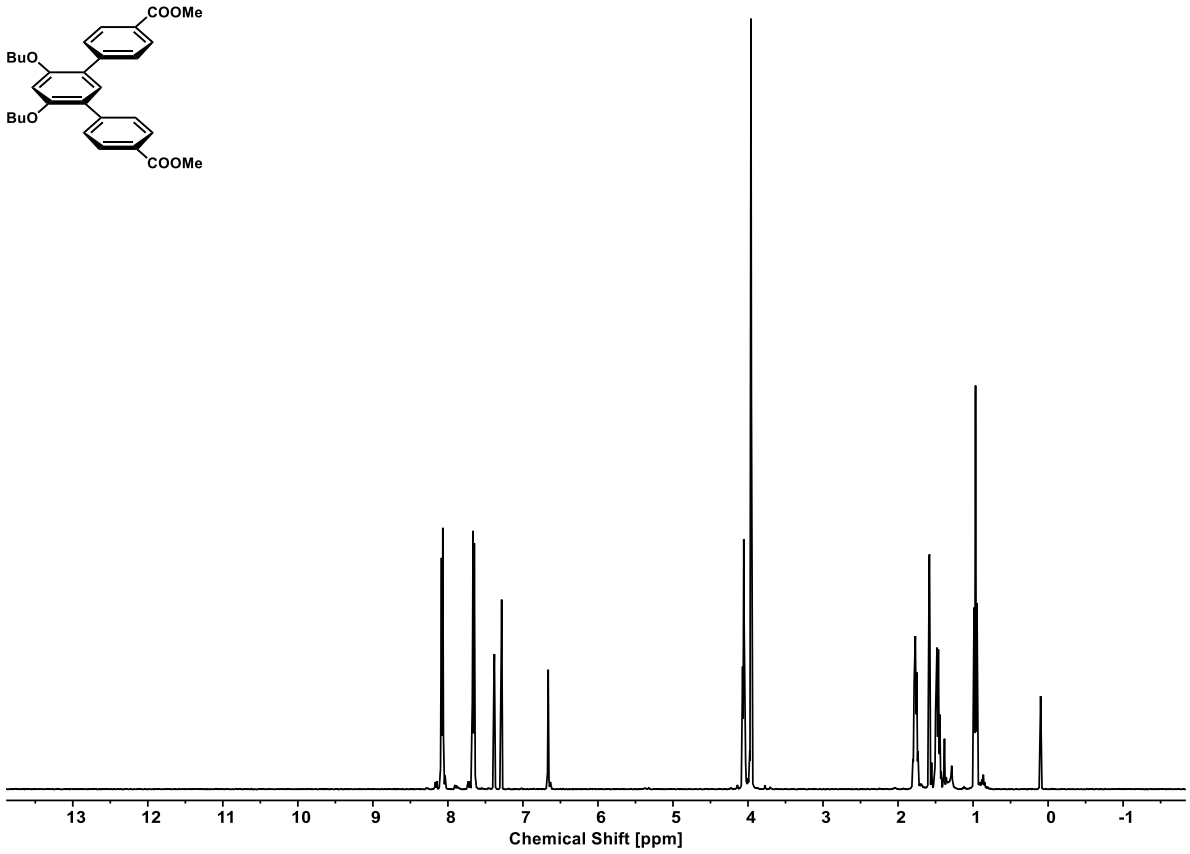

Figure S6. ^{1}H NMR spectrum of organic ligand **L-T$_{Me}$**.

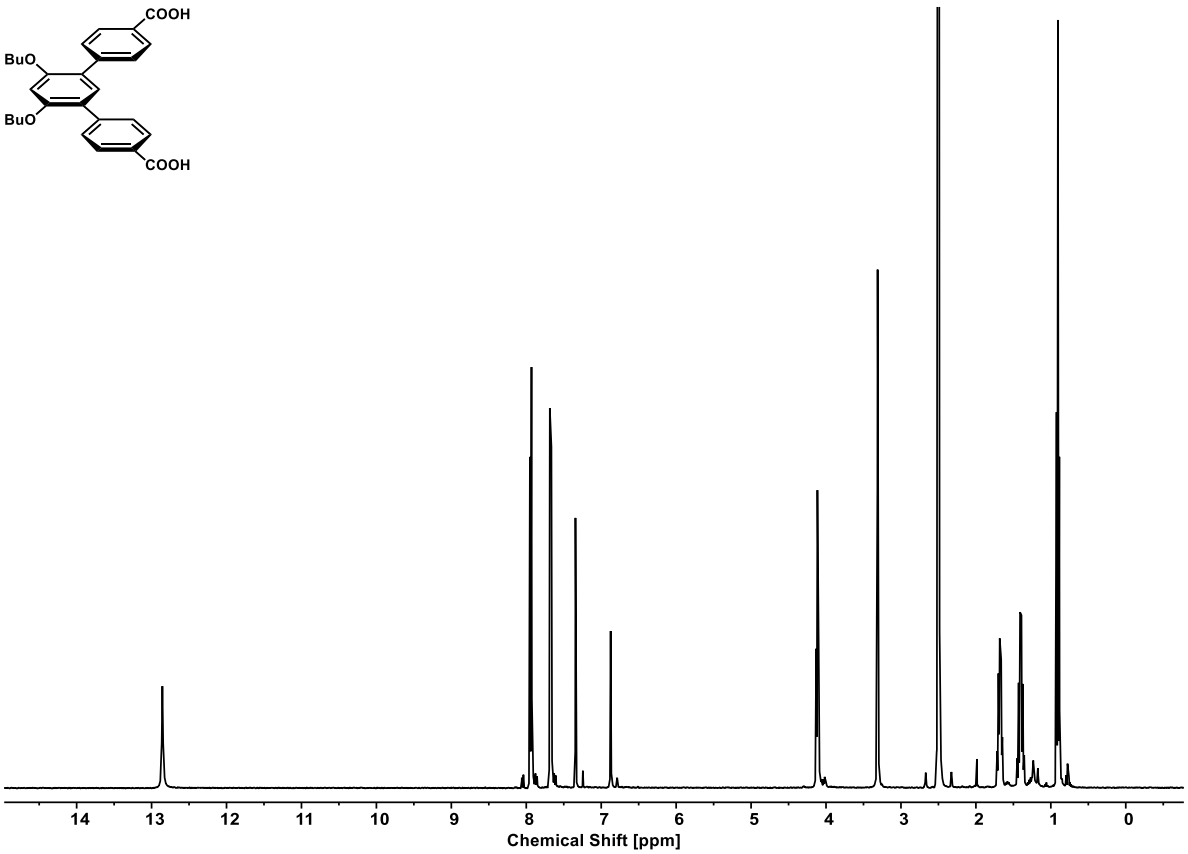

Figure S7. ^{1}H NMR spectrum of organic ligand **L-T$_{H}$**.

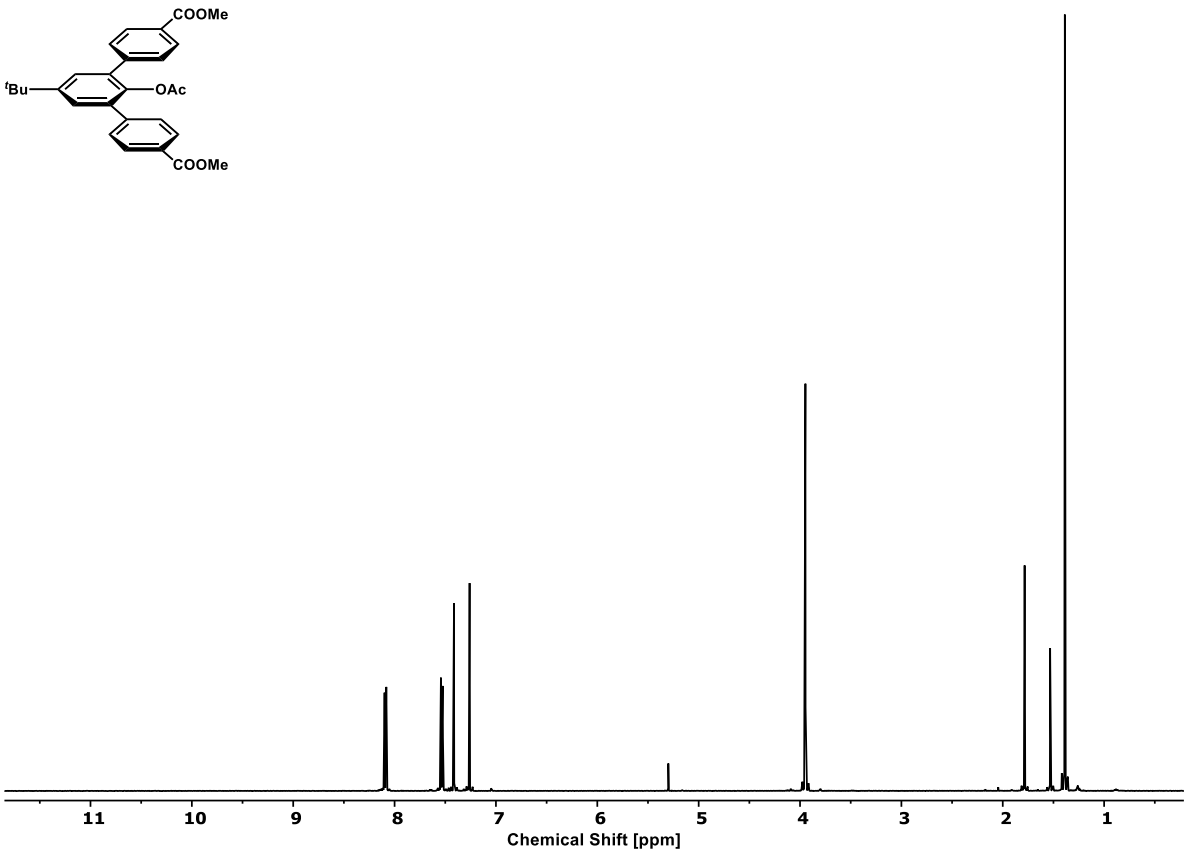

Figure S8. ^{1}H NMR spectrum of organic ligand **L-TO$_{Me}$**.

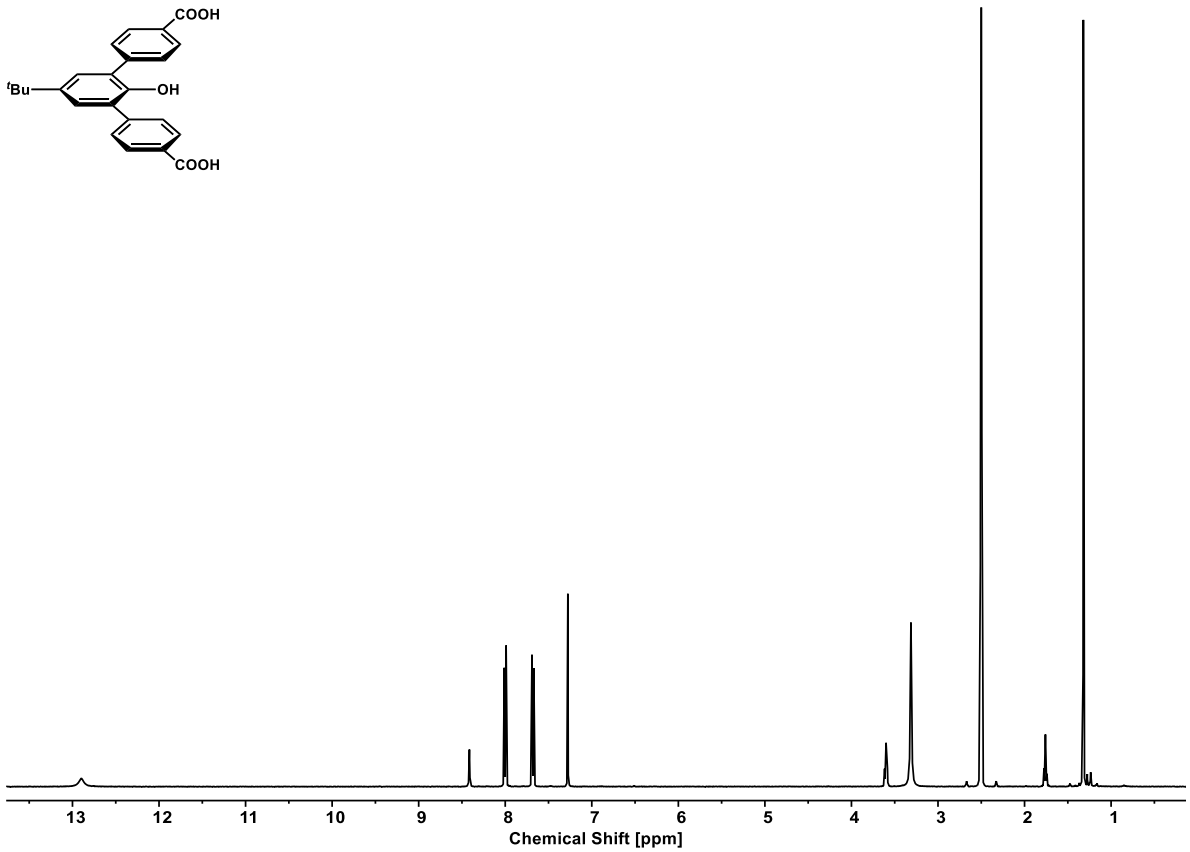

Figure S9. ^{1}H NMR spectrum of organic ligand **L-TO$_{H}$.**

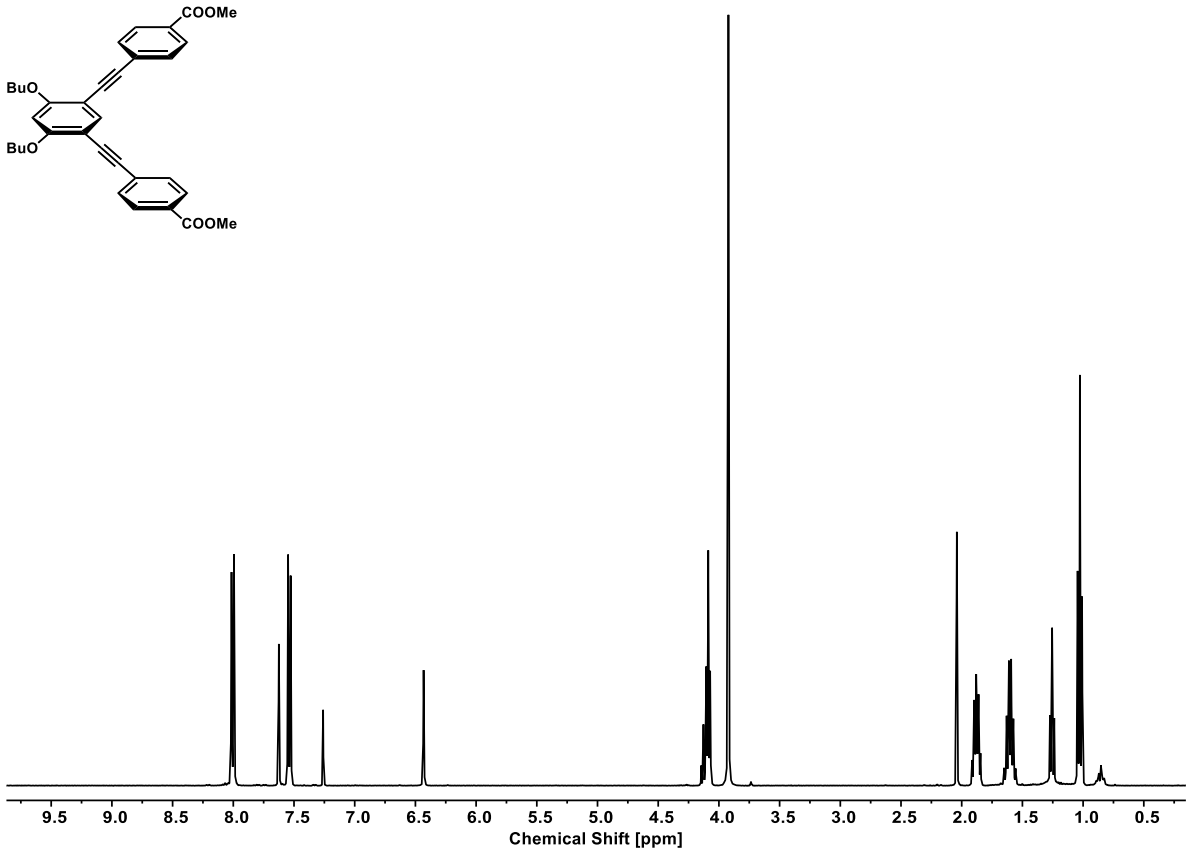

Figure S10. ^{1}H NMR spectrum of organic ligand **L-TE$_{Me}$.**

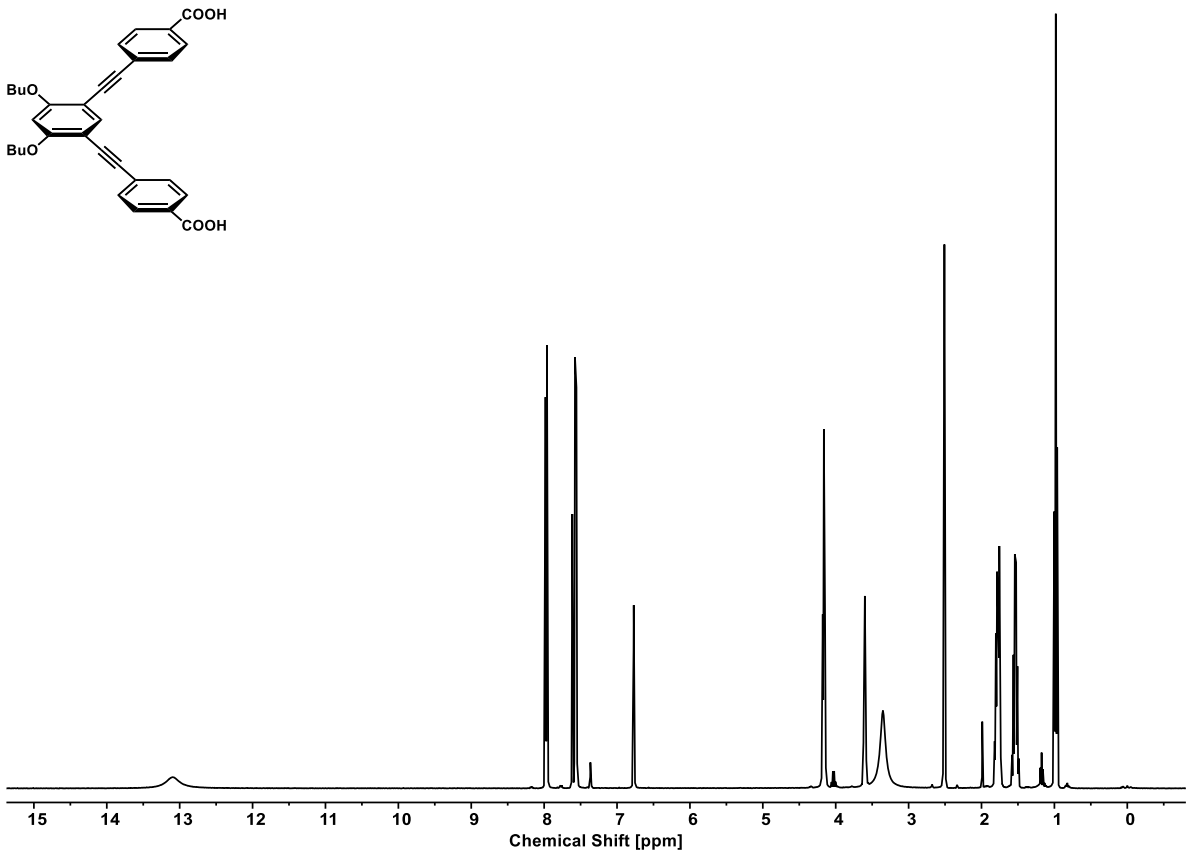

Figure S11. ^{1}H NMR spectrum of organic ligand **L-TE$_{H}$**.

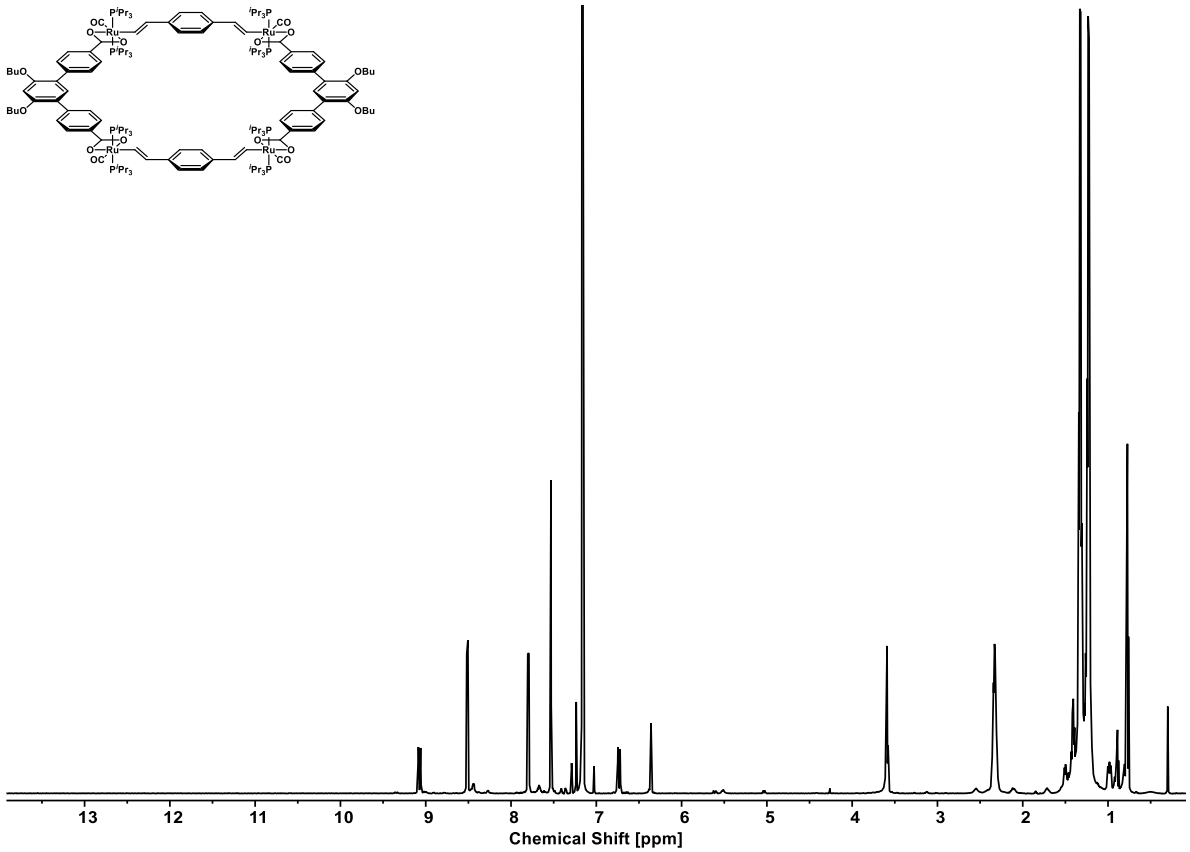

Figure S12. ^{1}H NMR spectrum of macrocycle **2-BT**.

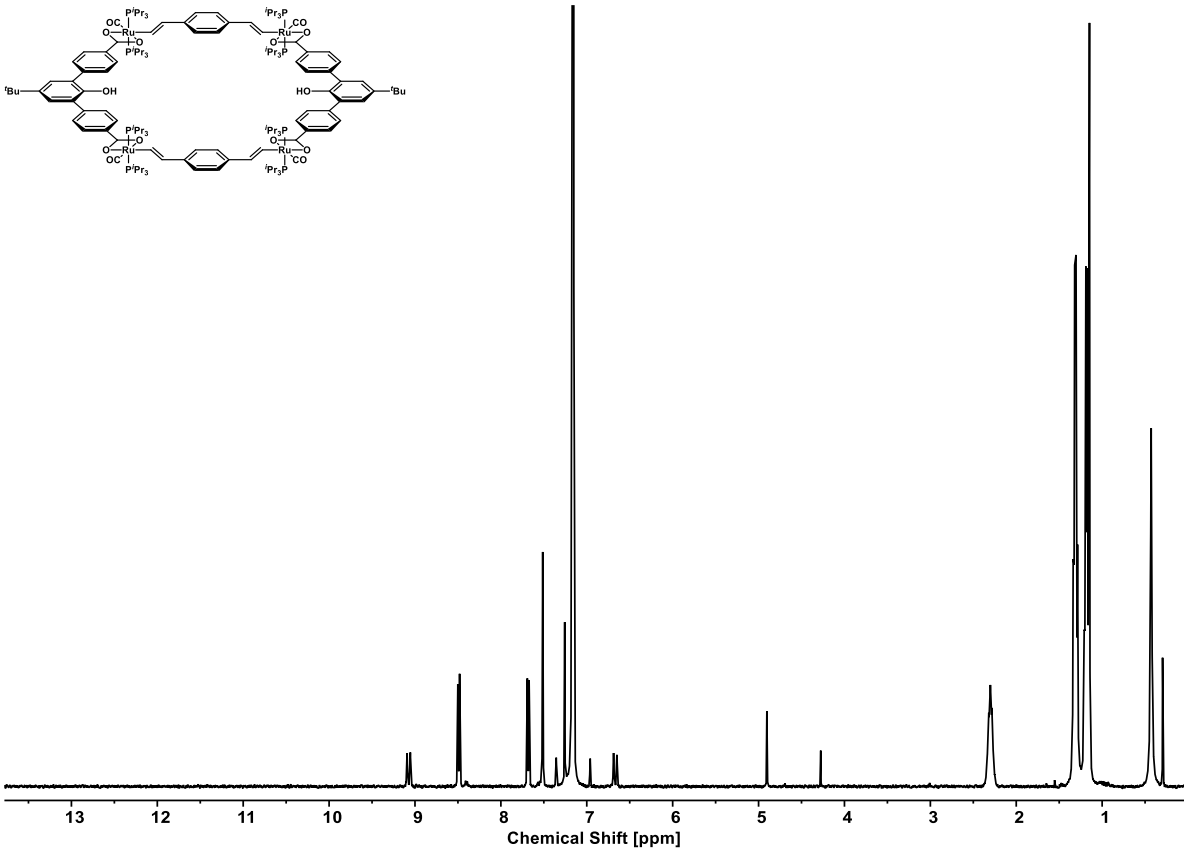

Figure S13. ^{1}H NMR spectrum of macrocycle **2-BTO**.

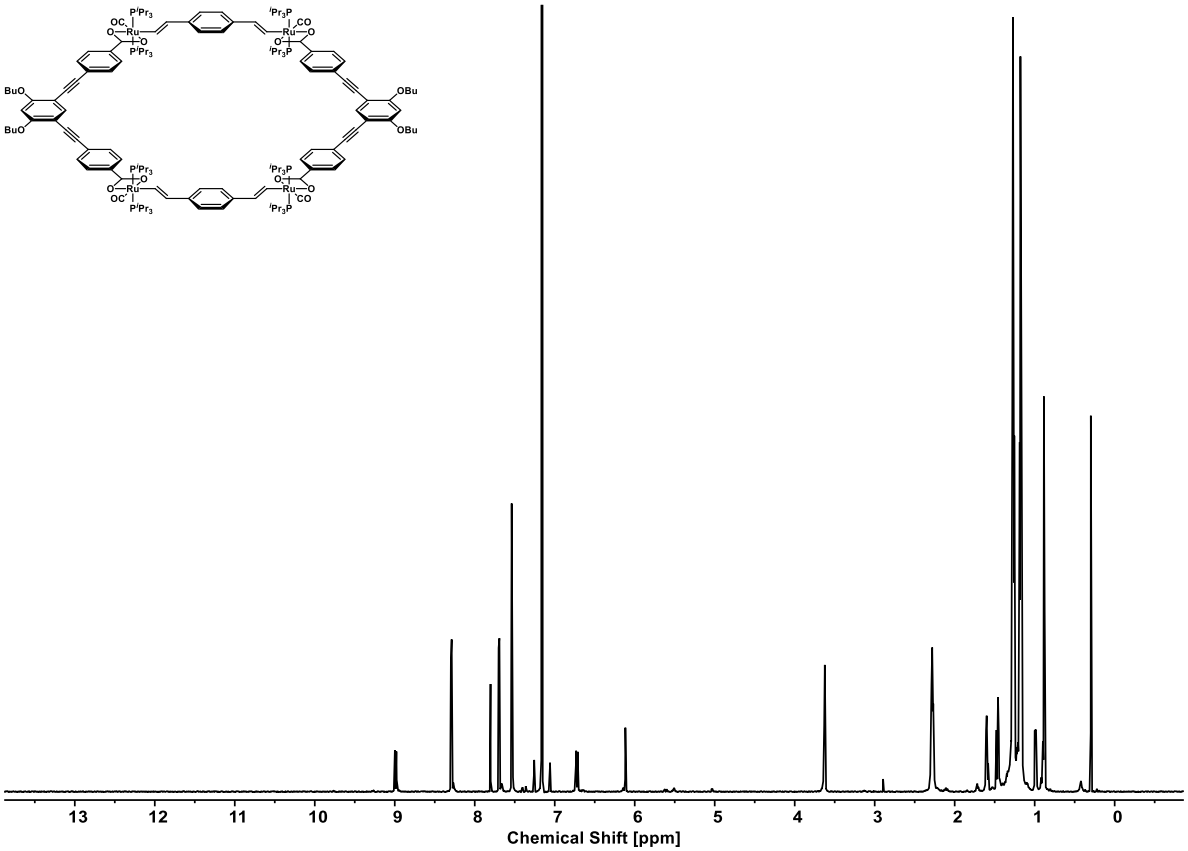

Figure S14. ^{1}H NMR spectrum of macrocycle **2-BTE**.

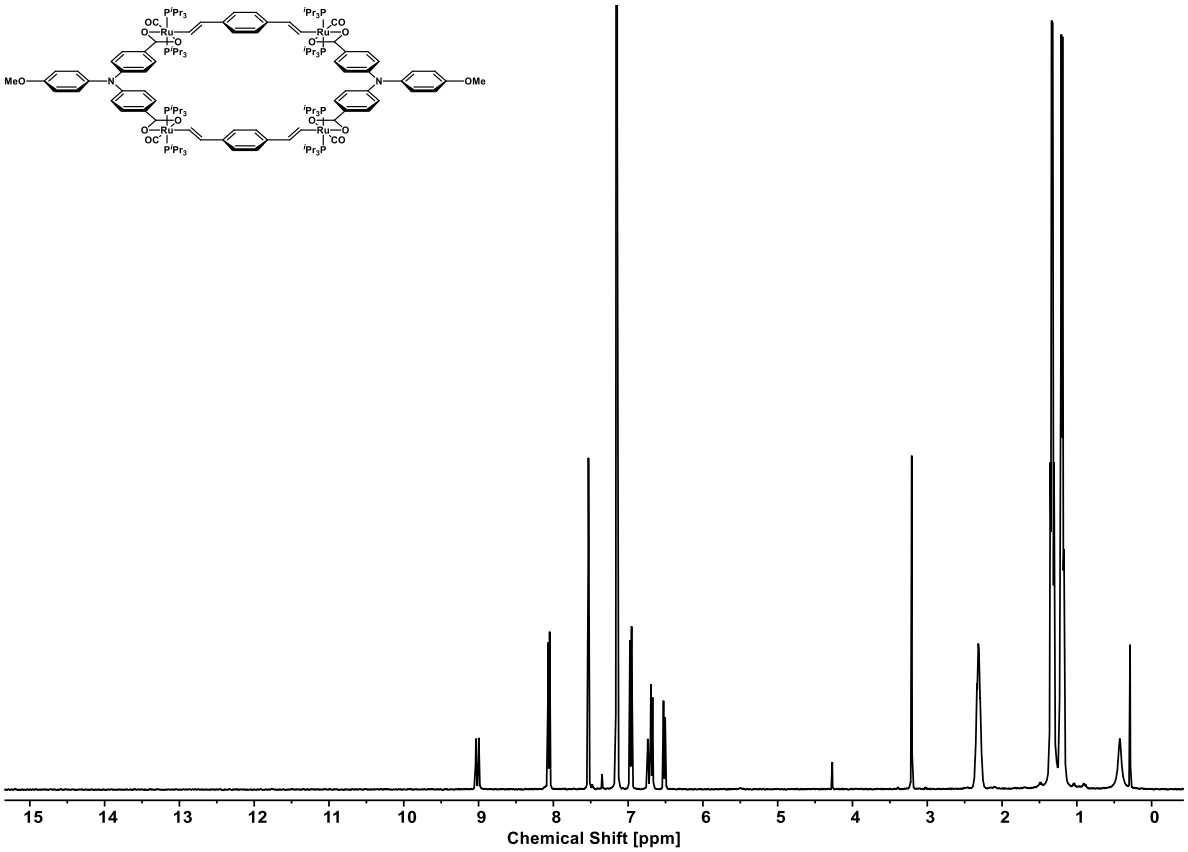

Figure S15. ^{1}H NMR spectrum of macrocycle **2-BN**.

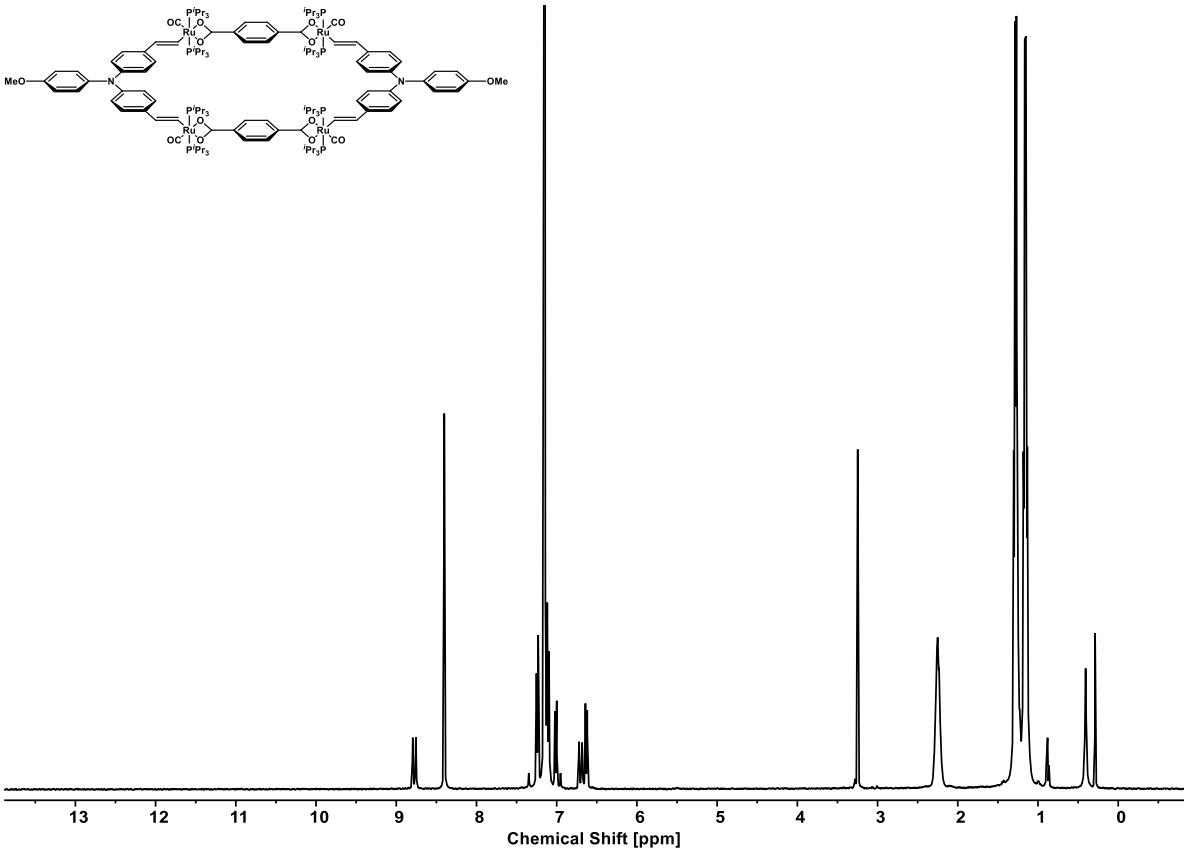

Figure S16. ^{1}H NMR spectrum of macrocycle **2-NB**.

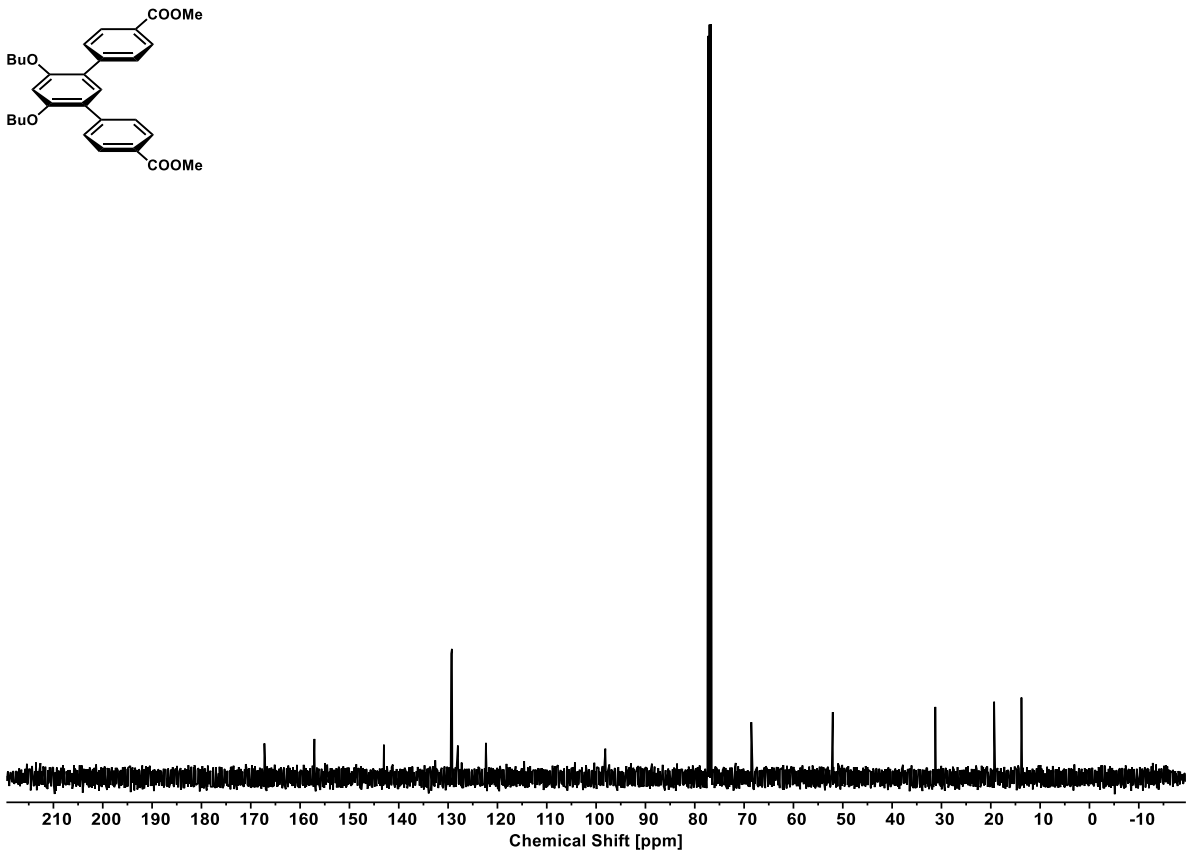

Figure S17. $^{13}C\{^{1}H\}$ NMR spectrum of organic ligand **L-T_{Me}**.

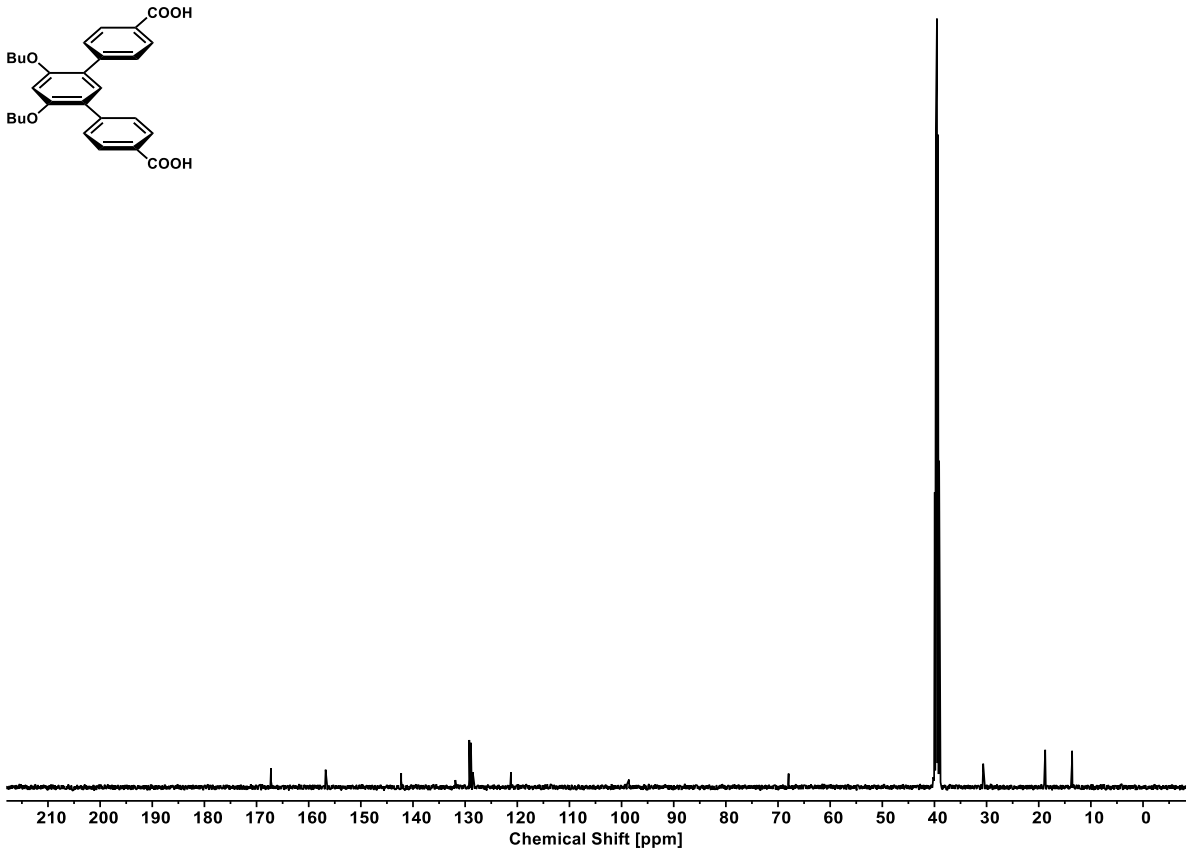

Figure S18. $^{13}C\{^{1}H\}$ NMR spectrum of organic ligand **L-T_{H}**.

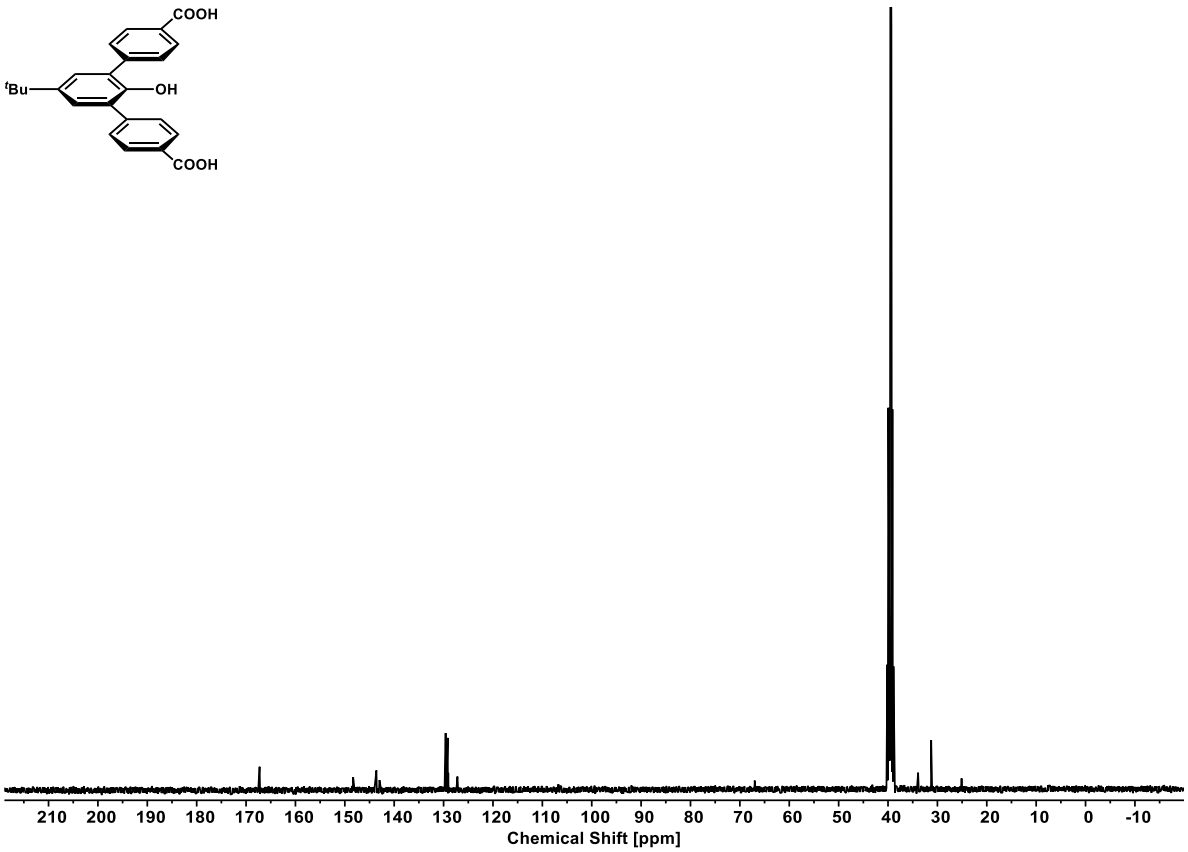

Figure S19. $^{13}C\{^{1}H\}$ NMR spectrum of organic ligand **L-TO$_{H}$**.

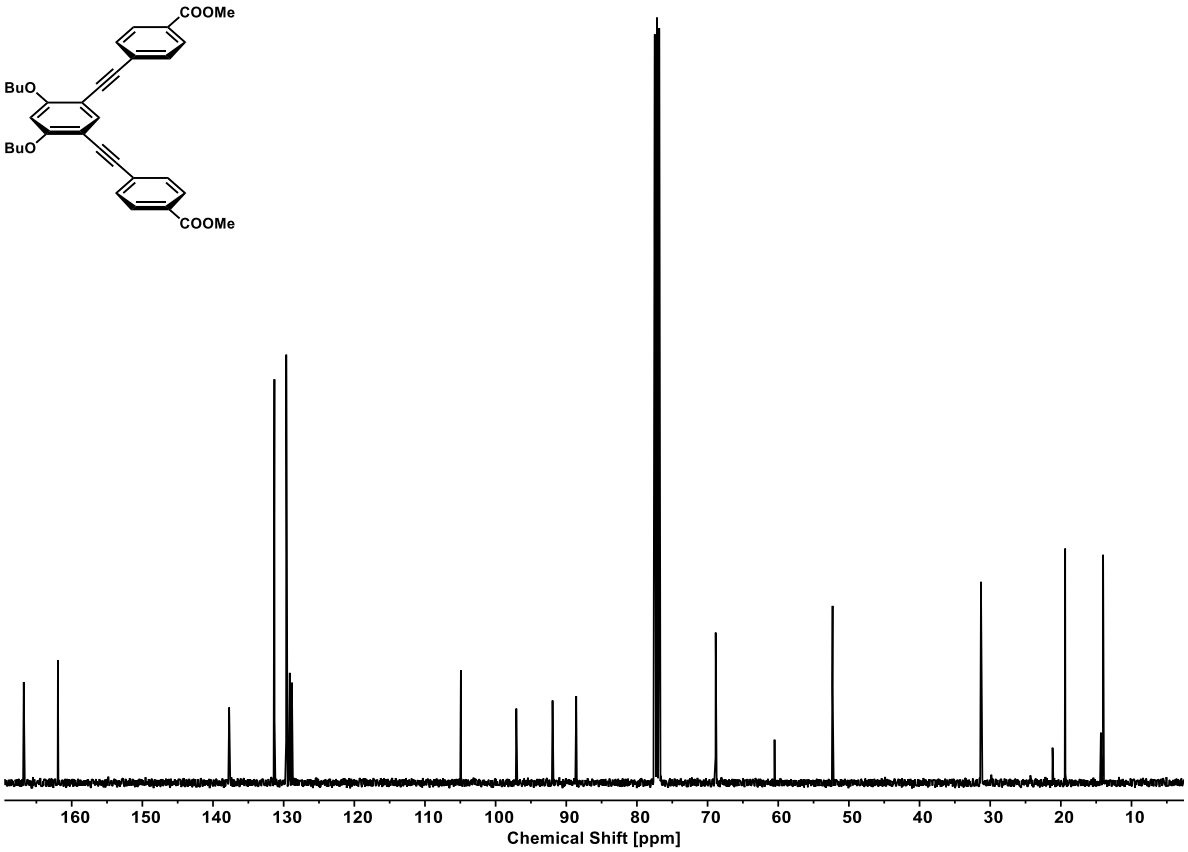

Figure S20. $^{13}C\{^{1}H\}$ NMR spectrum of organic ligand **L-TE$_{Me}$**.

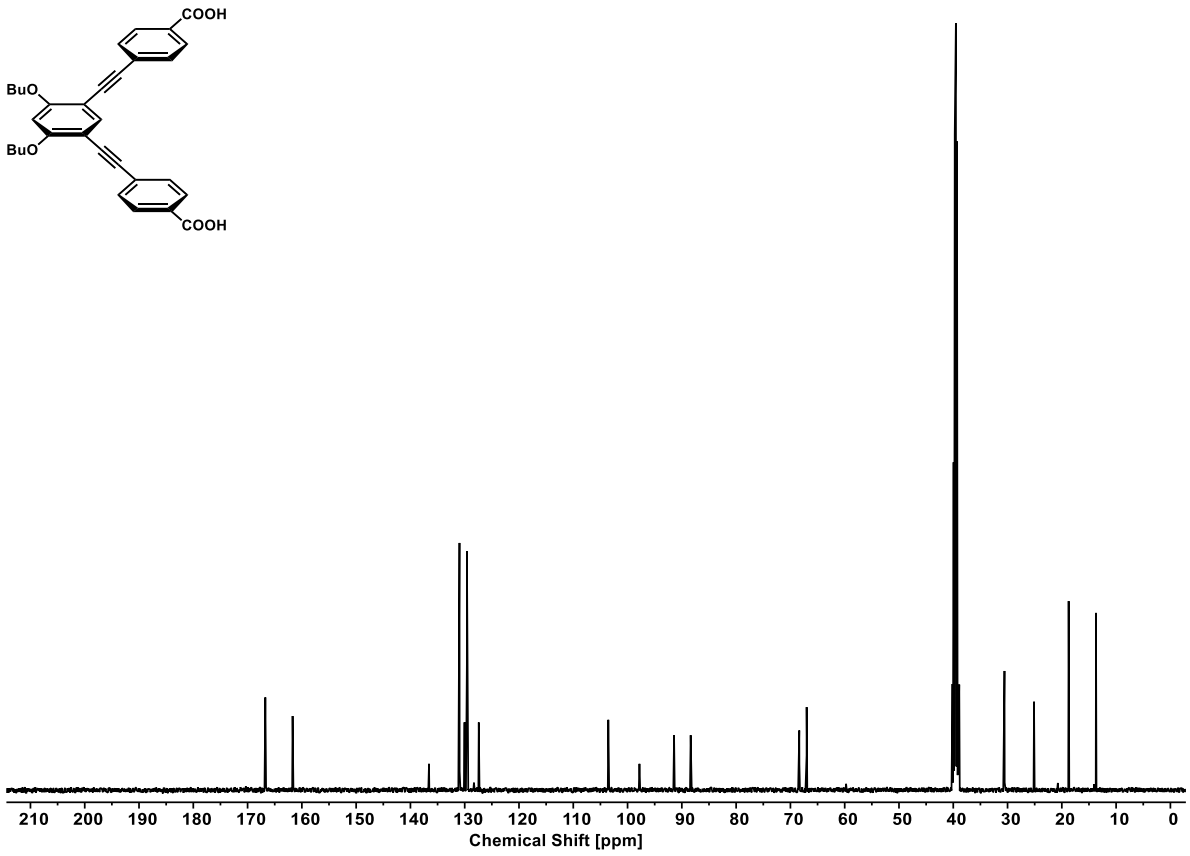

Figure S21. $^{13}C\{^{1}H\}$ NMR spectrum of organic ligand **L-TE$_H$**.

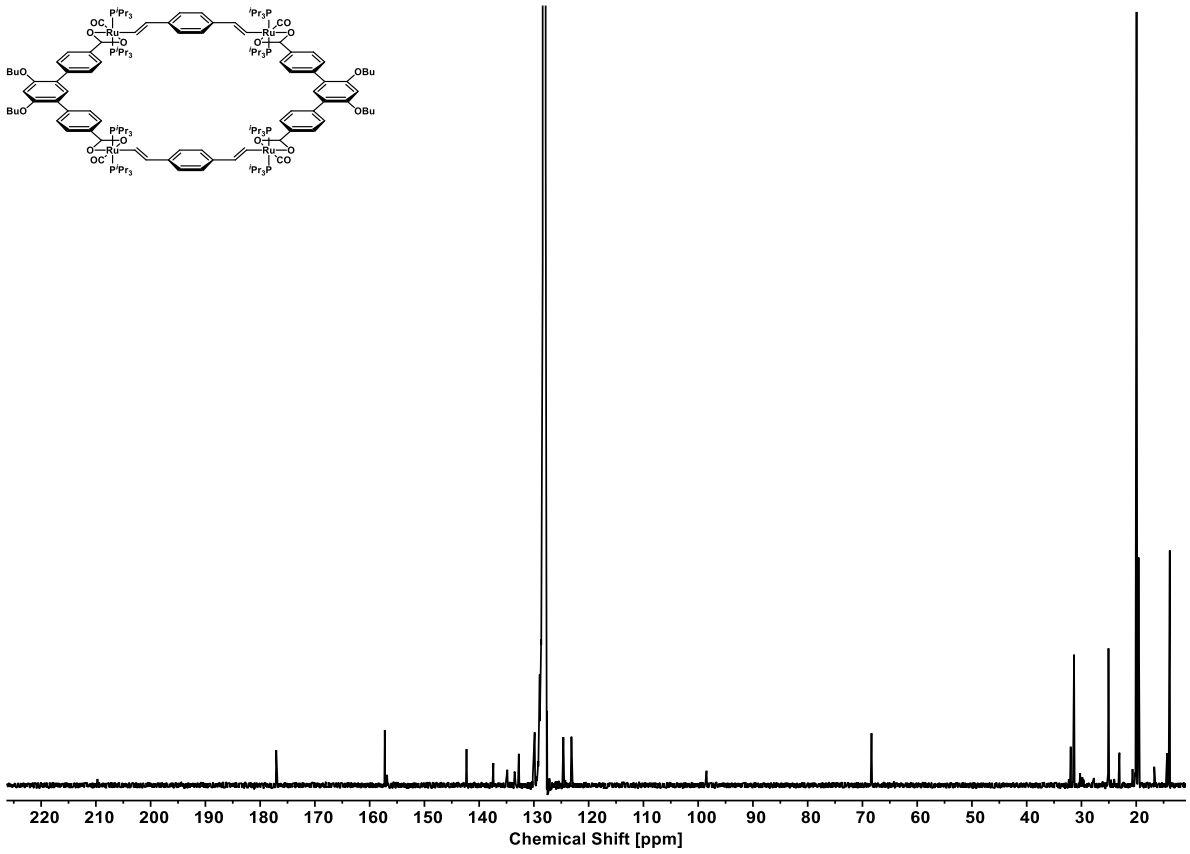

Figure S22. $^{13}C\{^{1}H\}$ NMR spectrum of macrocycle **2-BT**.

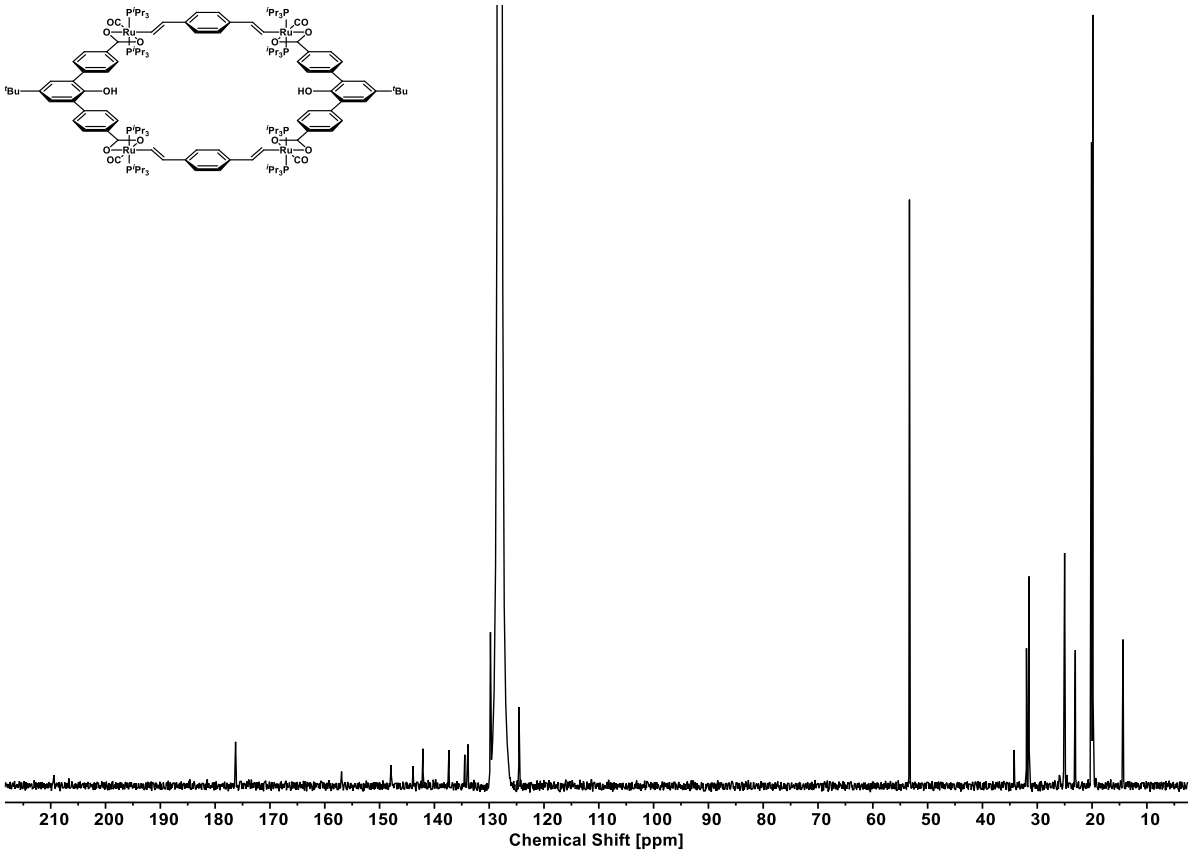

Figure S23. $^{13}C\{^{1}H\}$ NMR spectrum of macrocycle **2-BTO**.

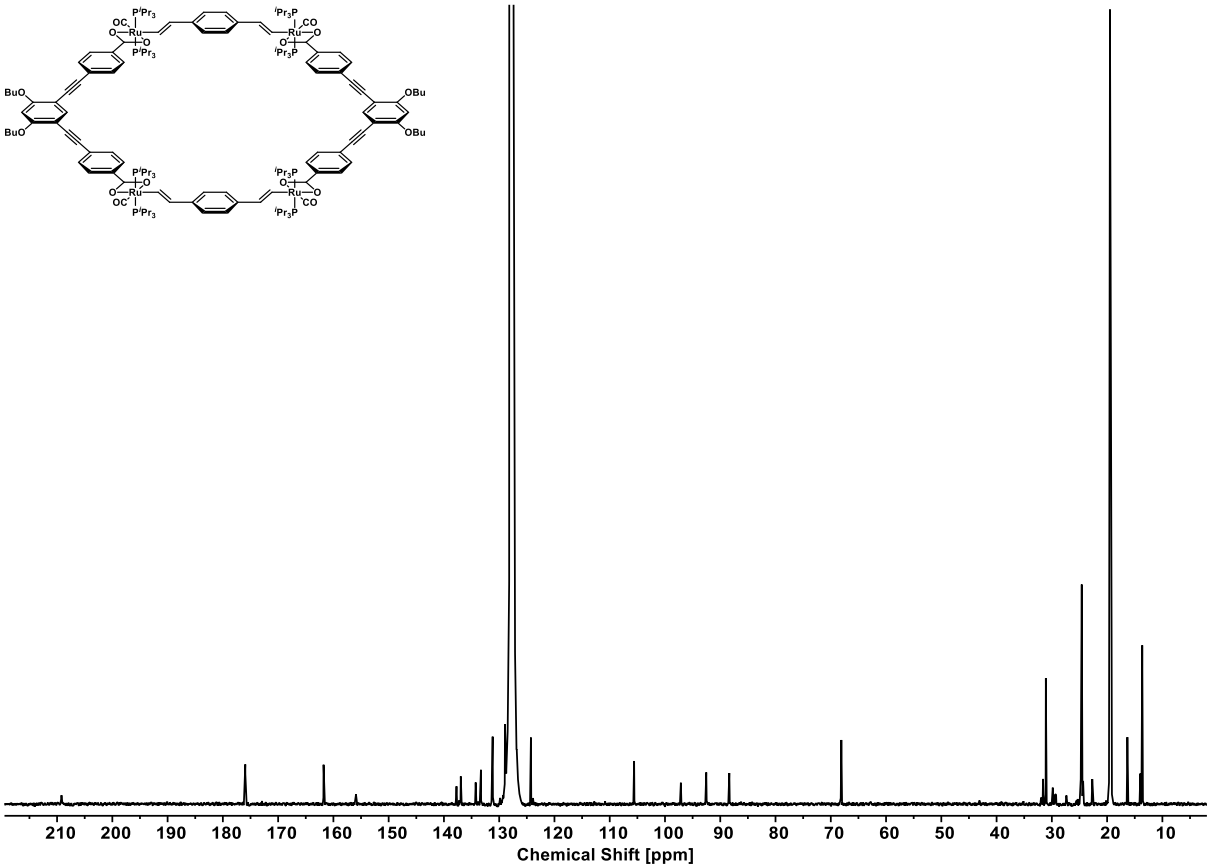

Figure S24. $^{13}C\{^{1}H\}$ NMR spectrum of macrocycle **2-BTE**.

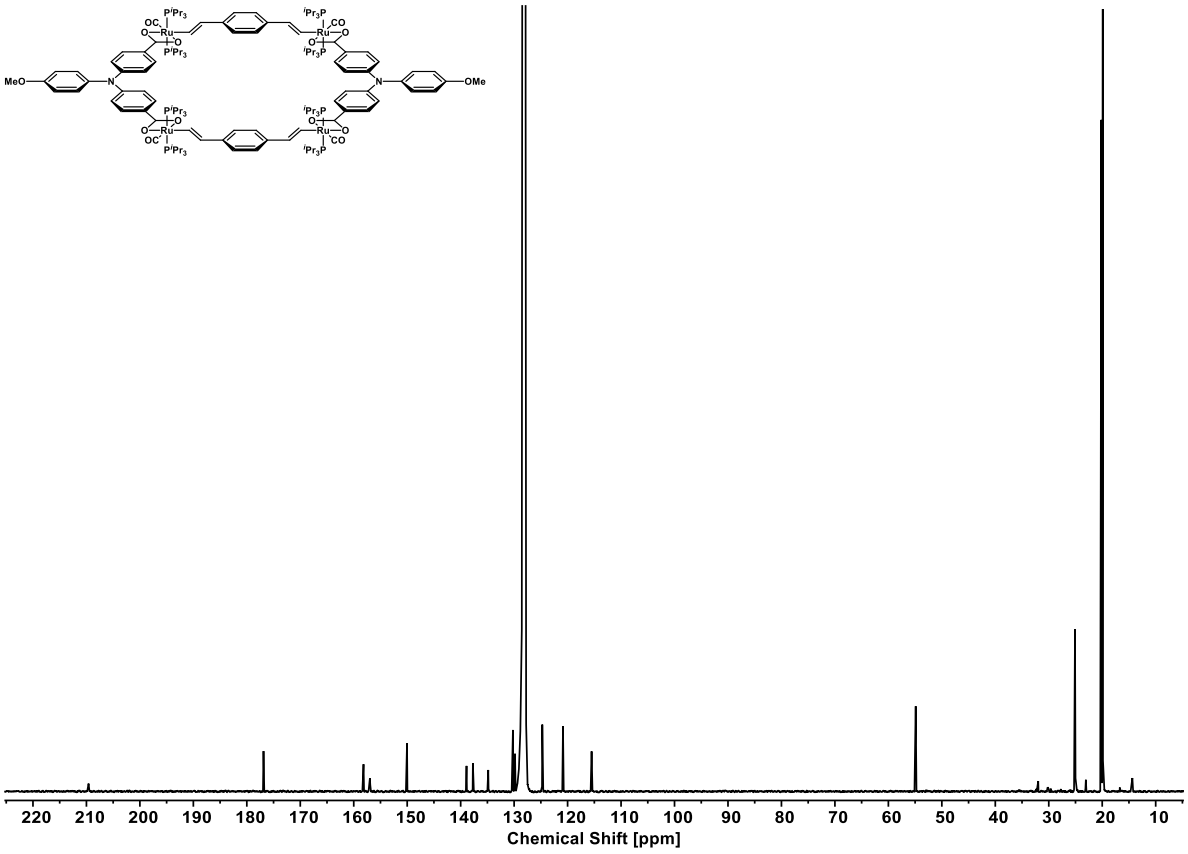

Figure S25. $^{13}C\{^{1}H\}$ NMR spectrum of macrocycle **2-BN**.

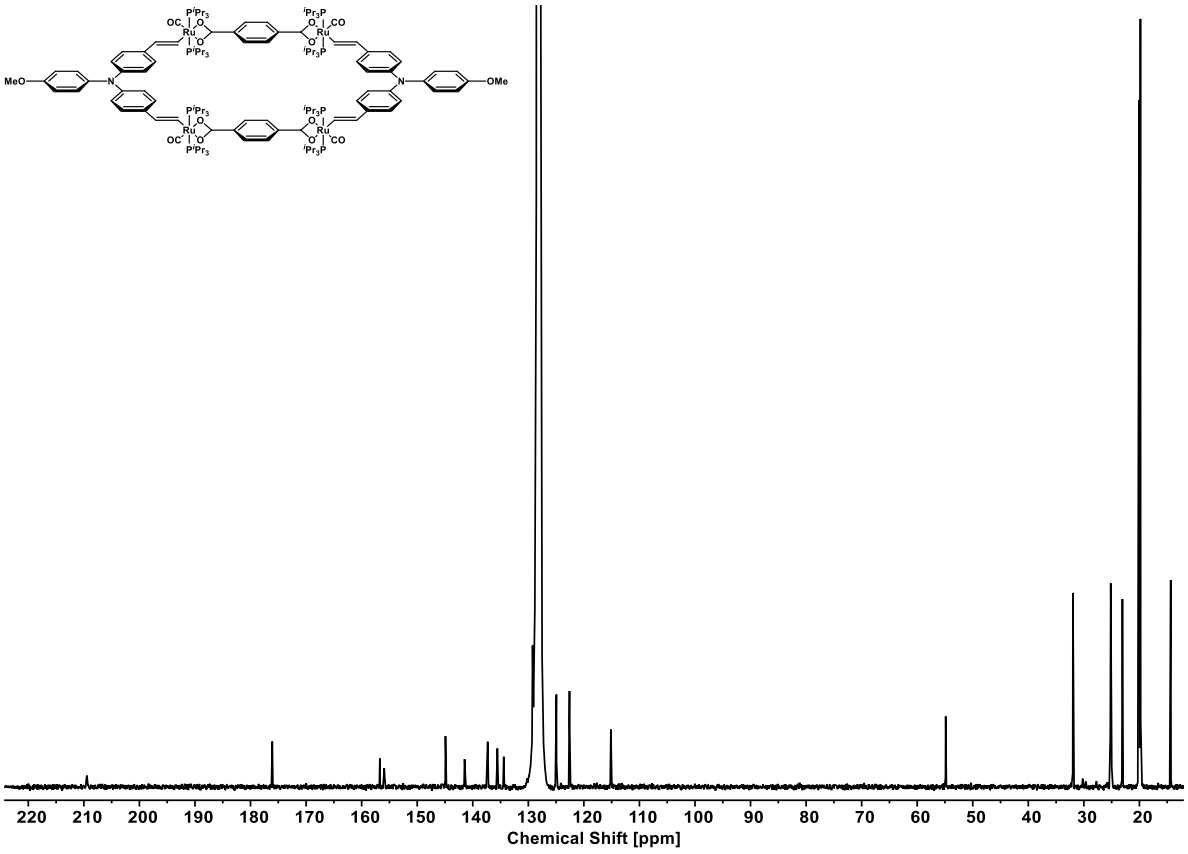

Figure S26. $^{13}C\{^{1}H\}$ NMR spectrum of macrocycle **2-NB**.

ESI MS

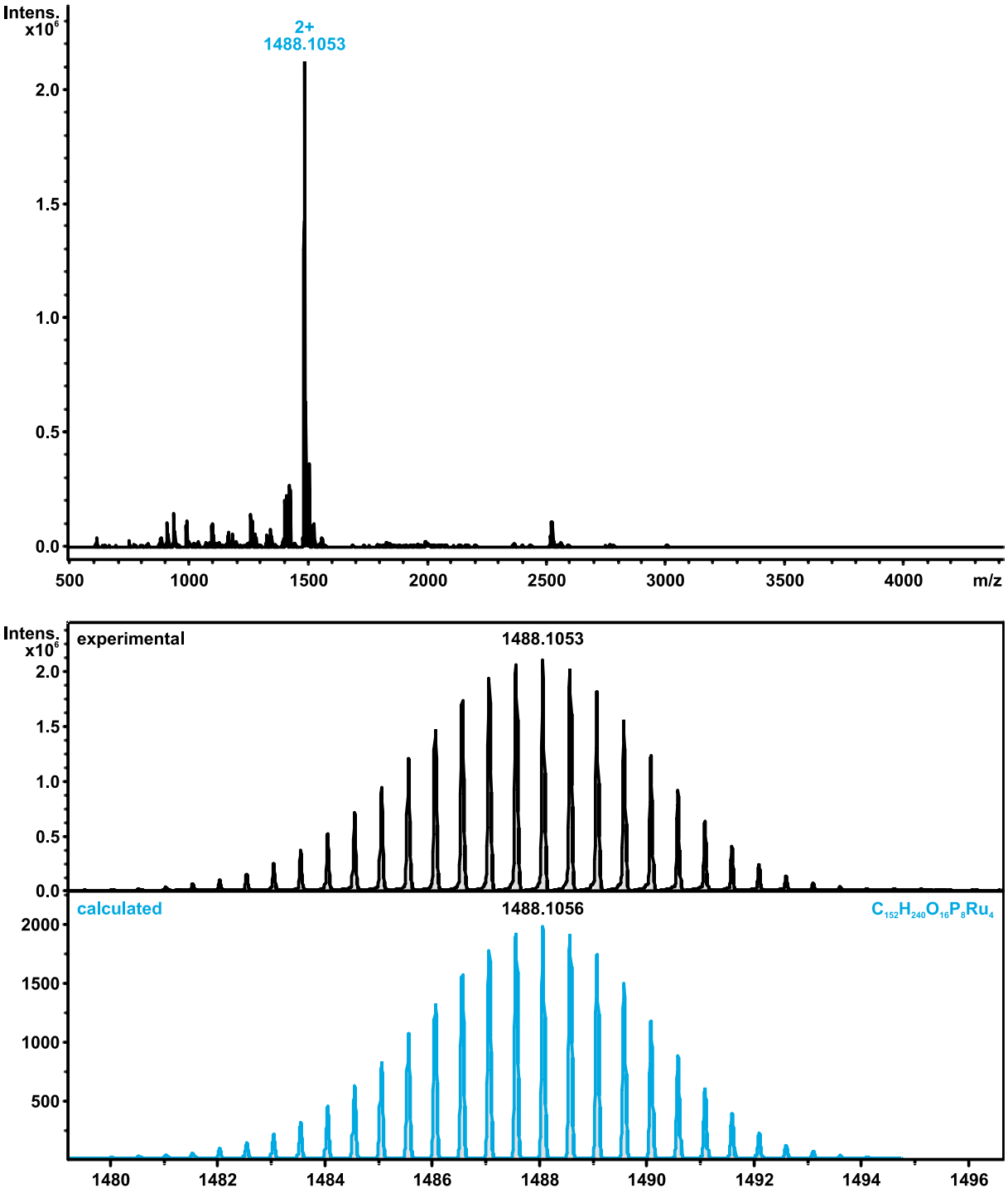

Figure S27. ESI Mass spectrum of macrocycle **2-BT** (top); magnification of $[M]^{2+}$ peak with calculated isotopic pattern (bottom).

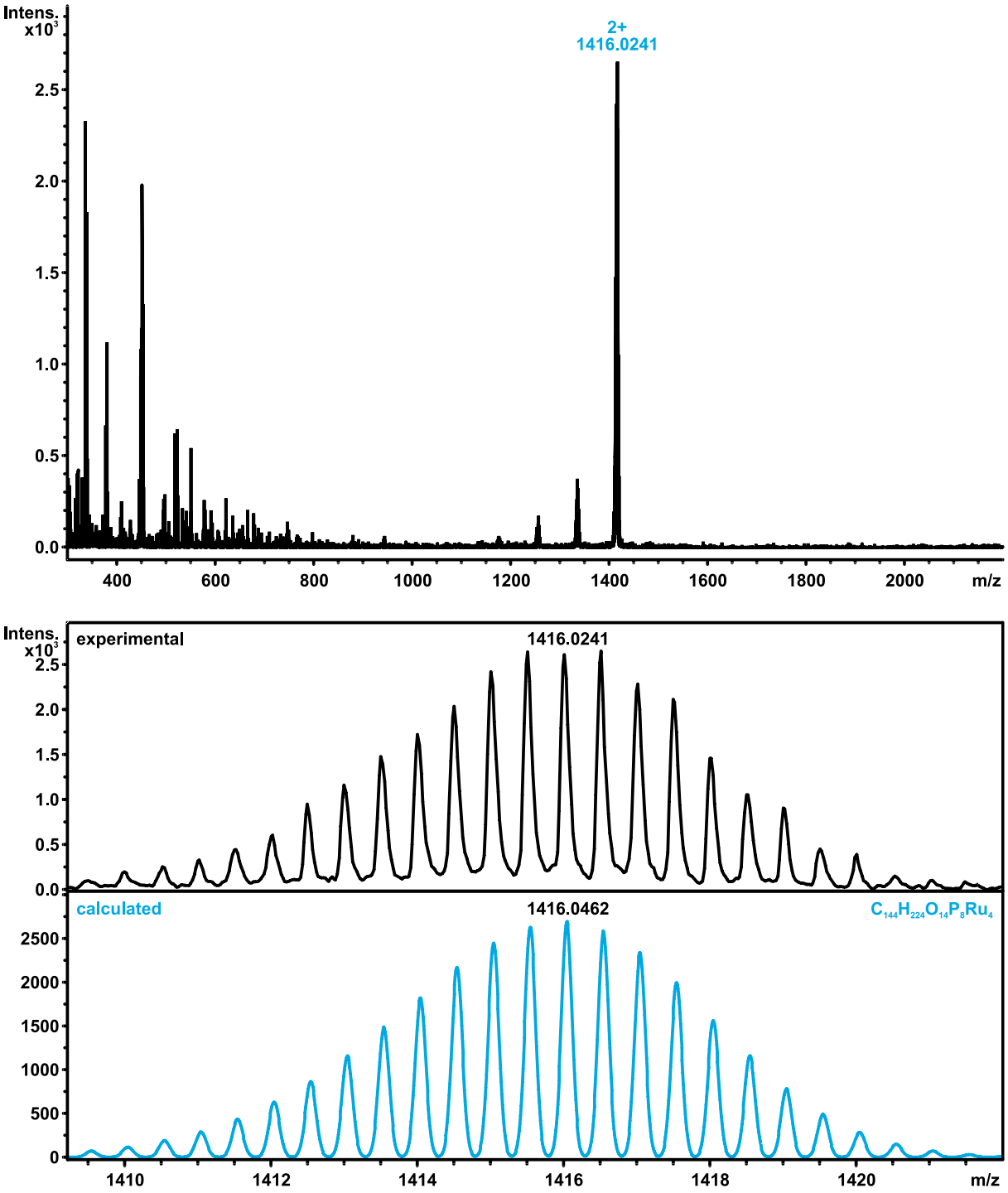

Figure S28. ESI Mass spectrum of macrocycle **2-BTO** (top), magnification of $[M]^{2+}$ peak with calculated isotopic pattern (bottom).

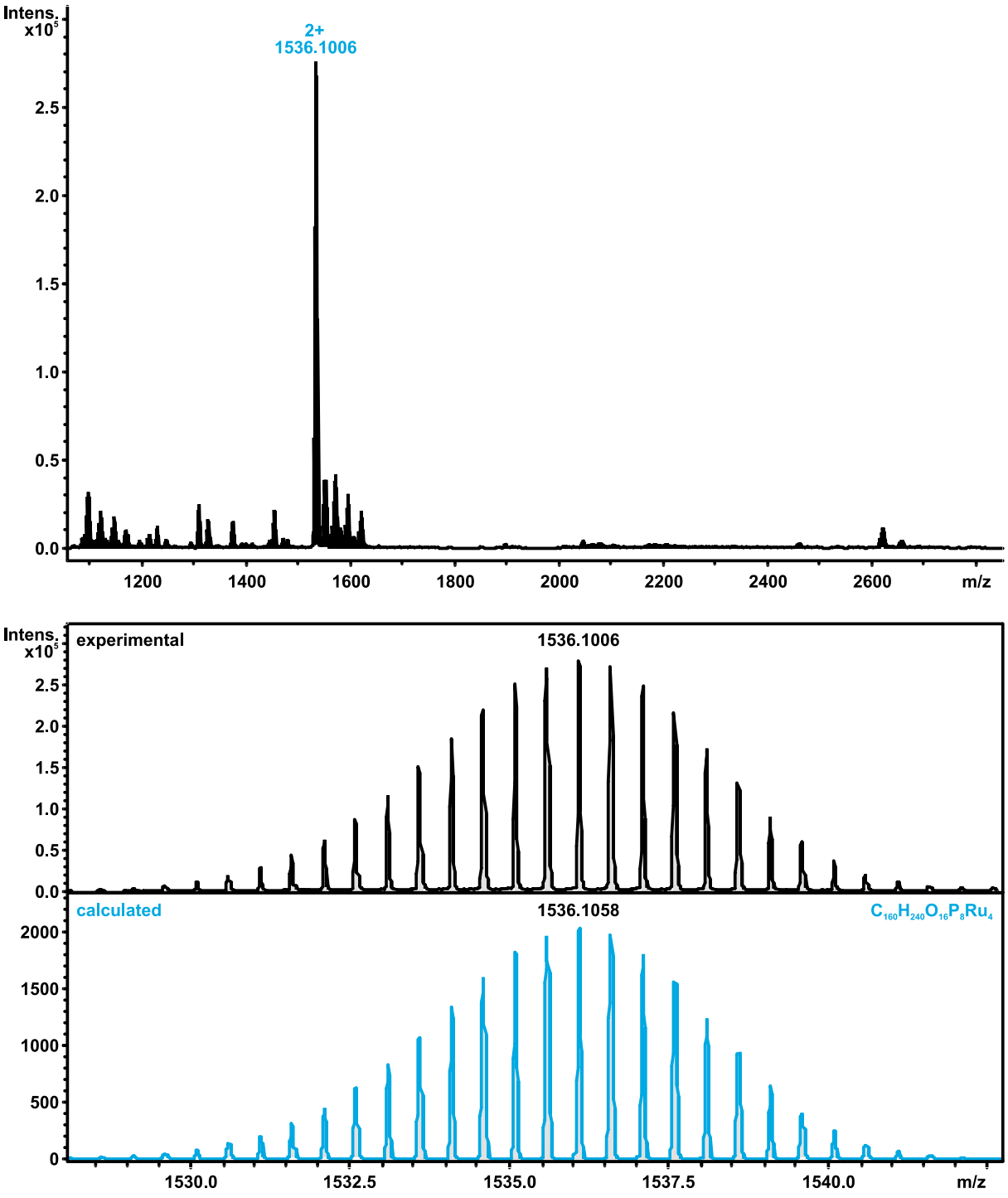

Figure S29. ESI Mass spectrum of macrocycle **2-BTE** (top), magnification of $[M]^{2+}$ peak with calculated isotopic pattern (bottom).

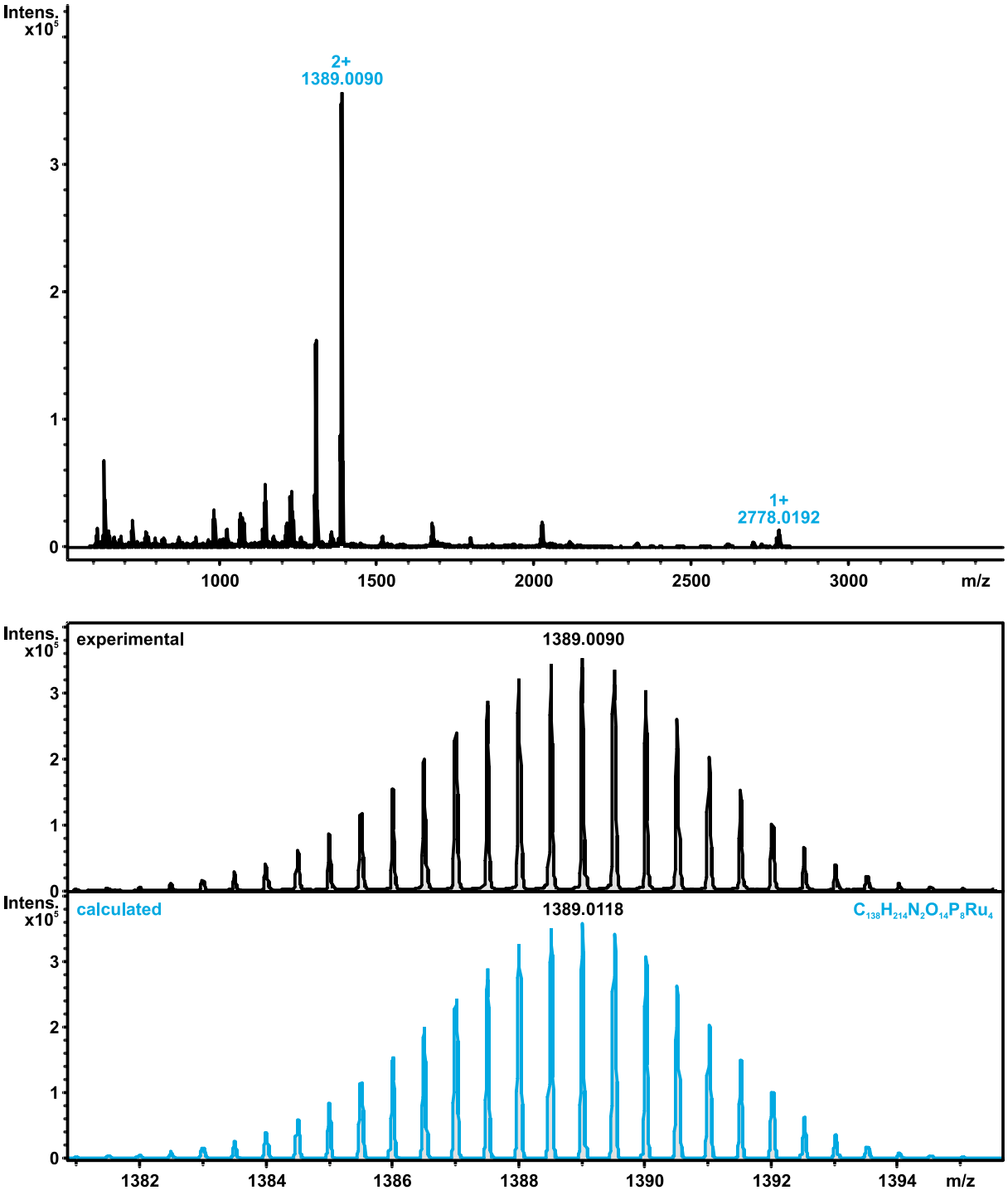

Figure S30. ESI Mass spectrum of macrocycle **2-BN** (top), magnification of $[M]^{2+}$ peak with calculated isotopic pattern (bottom).

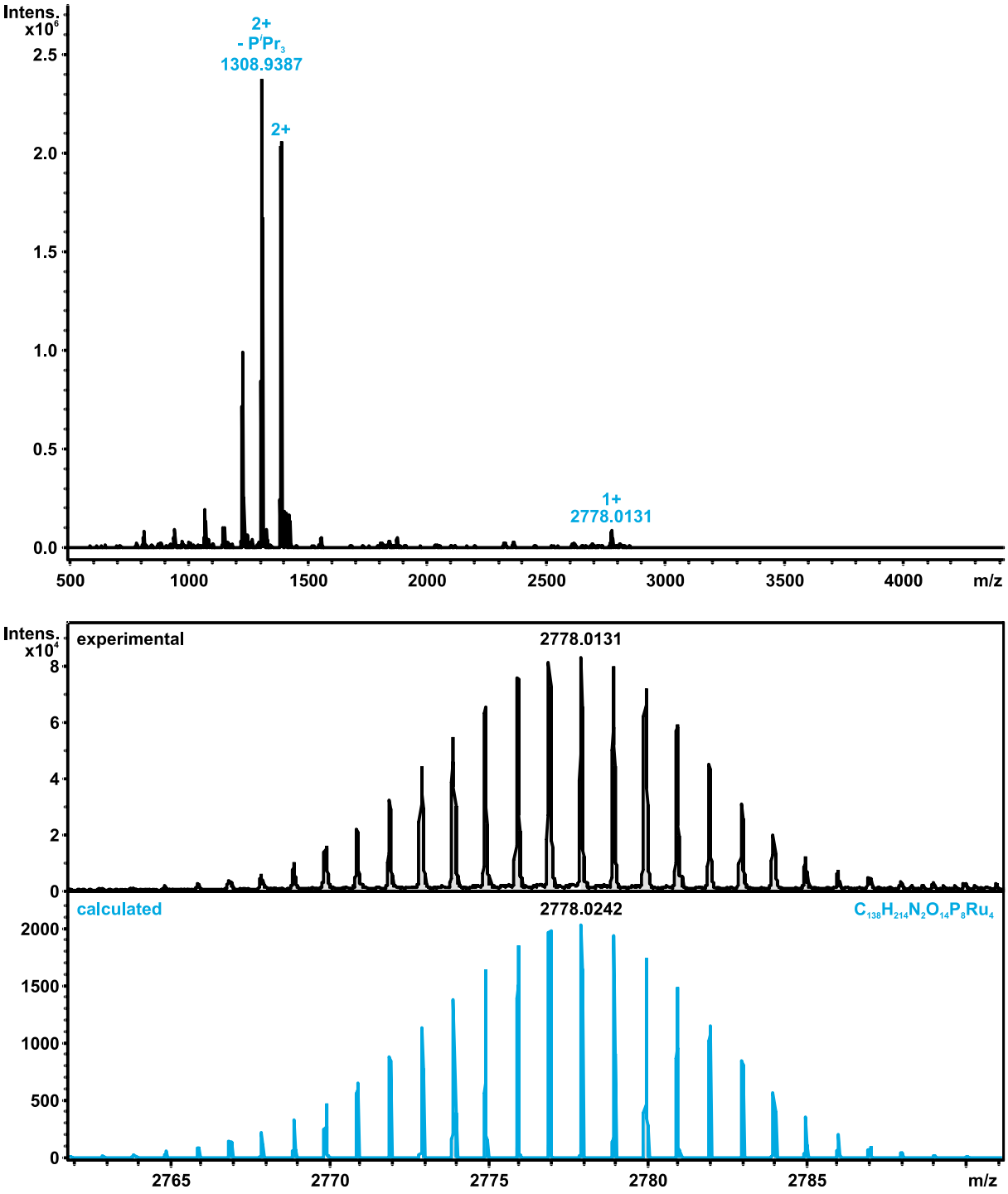

Figure S31. ESI Mass spectrum of macrocycle **2-NB** (top), magnification of $[M]^{2+}$ peak with calculated isotopic pattern (bottom).

X-ray Crystallography

Compound 2-BT:

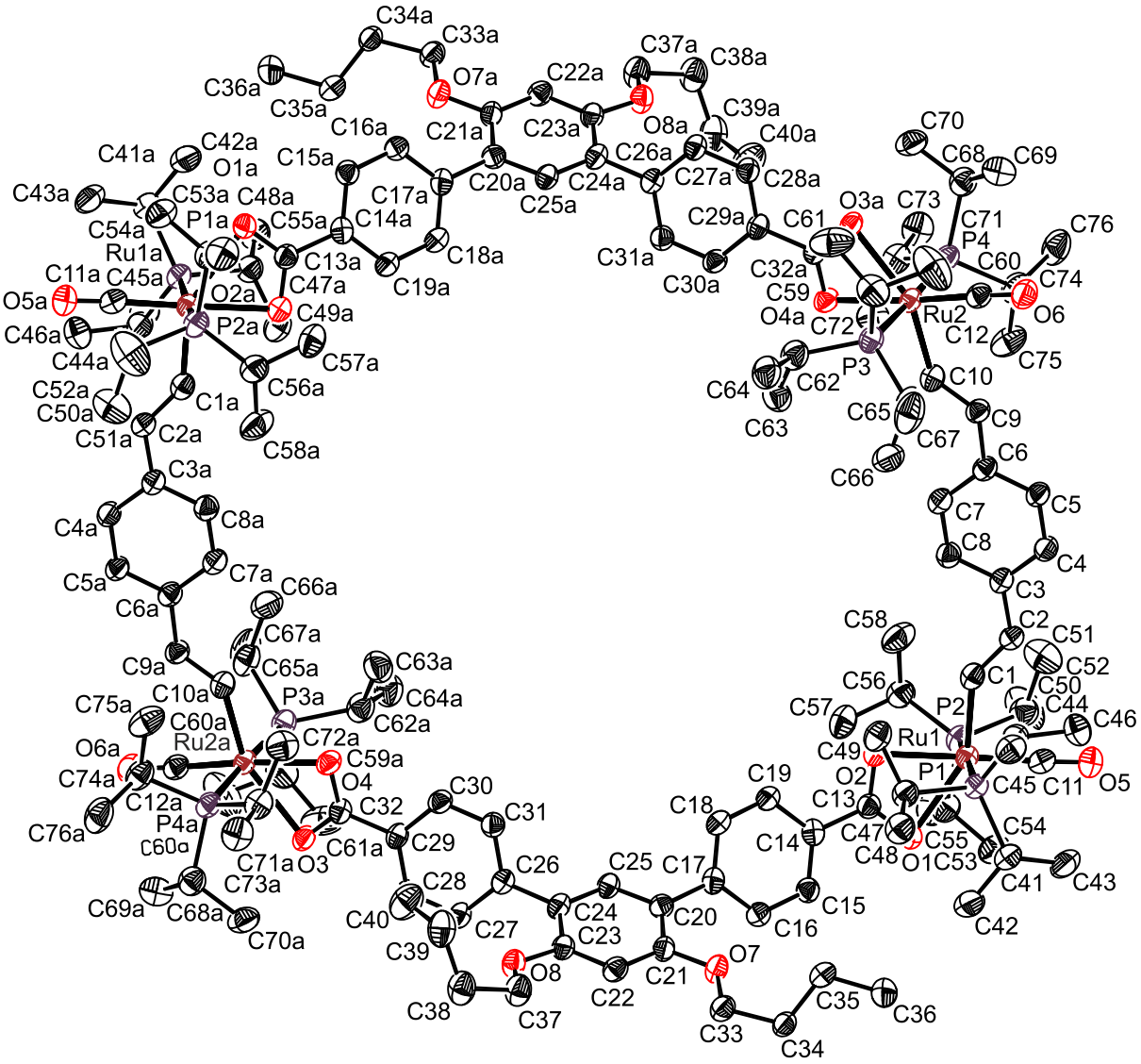

Figure S32. Structure of macrocycle **2-BT** as the benzene hexadecasolvate with atom numbering. Benzene solvate molecules as well as hydrogen atoms have been removed for clarity reasons. Ellipsoids are drawn at a 50% probability level.

Experimental. Single crystals of **2-BT** were obtained as yellow blocks by slow diffusion of methanol into a solution of compound **2-BT** in benzene. A suitable crystal was selected and mounted on a STOE IPDS-II diffractometer. The crystal was kept at 100.15 K during data collection. Using **Olex2**[1], the structure was solved with the **ShelXT**[2] structure solution program using Intrinsic Phasing and refined with the **ShelXL**[3] refinement package using Least Squares minimisation.

Table S1. Crystal data and structure refinement for macrocycle **2-BT·16C_6H_6**.

Empirical formula	$C_{200}H_{288}O_{16}P_8Ru_4$	
Formula weight	3600.33	
Temperature	100.15 K	
Wavelength	0.71073 Å	
Crystal system	Monoclinic	
Space group	$P2_1/n$	
Unit cell dimensions	a = 15.2041(12) Å	α = 90 °
	b = 34.499(3) Å	β = 107.200(5) °
	c = 22.5225(16) Å	γ = 90 °
Volume	11285.3(15) Å^3	
Z	2	
Density (calculated)	1.060 Mg/m^3	
Absorption coefficient	0.369 mm^{-1}	
F(000)	3824.0	
Crystal size	0.4 × 0.3 × 0.2 mm^3	
2Θ range for data collection	2.882 to 49.998°	
Index ranges	$-17 \leq h \leq 18$, $-40 \leq k \leq 40$, $-26 \leq l \leq 26$	
Reflections collected	88549	
Independent reflections	19767 [R_{int} = 0.0773, R_{sigma} = 0.0633]	
Refinement method	Full-matrix least-squares on F^2	
Data / restraints / parameters	19767/0/1054	
Goodness-of-fit on F^2	0.952	
Final R indices [$I \geq 2\sigma(I)$]	R_1 = 0.0515, wR_2 = 0.1186	
R indices (all data)	R_1 = 0.0780, wR_2 = 0.1289	
Largest diff. peak and hole	0.59 and -0.65 e Å^{-3}	

Table S2. Selected bond lengths [Å] for **2-BT·16C_6H_6**.

Ru(1) - P(1)	2.4313(10)	C(7) - C(8)	1.384(5)
Ru(1) - P(2)	2.4087(11)	C(9) - C(10)	1.343(5)
Ru(1) - O(1)	2.344(3)	C(13) - C(14)	1.496(5)
Ru(1) - O(2)	2.183(2)	C(14) - C(15)	1.385(5)
Ru(1) - C(1)	2.005(4)	C(14) - C(19)	1.401(5)
Ru(1) - C(11)	1.801(4)	C(15) - C(16)	1.392(5)
Ru(2) - P(3)	2.4244(11)	C(16) - C(17)	1.405(5)
Ru(2) - P(4)	2.4144(11)	C(17) - C(18)	1.393(5)
Ru(2) - O(3)	2.304(2)	C(17) - C(20)	1.494(5)
Ru(2) - O(4)	2.181(3)	C(18) - C(19)	1.389(6)
Ru(2) - C(10)	2.017(4)	C(20) - C(21)	1.399(5)
Ru(2) - C(12)	1.797(4)	C(20) - C(25)	1.395(5)
O(1) - C(13)	1.271(4)	C(21) - C(22)	1.397(5)
O(2) - C(13)	1.271(4)	C(22) - C(23)	1.397(5)
O(3) - C(32)	1.258(4)	C(23) - C(24)	1.395(5)
O(4) - C(32)	1.274(4)	C(24) - C(25)	1.392(5)
O(5) - C(11)	1.174(5)	C(24) - C(26)	1.495(5)
O(6) - C(12)	1.175(5)	C(26) - C(27)	1.395(5)
O(7) - C(21)	1.373(4)	C(26) - C(31)	1.388(5)
O(7) - C(33)	1.435(5)	C(27) - C(28)	1.393(5)
O(8) - C(23)	1.381(4)	C(28) - C(29)	1.387(5)
O(8) - C(37)	1.439(5)	C(29) - C(30)	1.393(5)
C(1) - C(2)	1.338(5)	C(29) - C(32)	1.496(5)
C(2) - C(3)	1.473(5)	C(30) - C(31)	1.391(5)
C(3) - C(4)	1.399(5)	C(33) - C(34)	1.518(5)
C(3) - C(8)	1.399(5)	C(34) - C(35)	1.520(6)
C(4) - C(5)	1.385(5)	C(35) - C(36)	1.529(6)
C(5) - C(6)	1.402(5)	C(37) - C(38)	1.519(6)
C(6) - C(7)	1.414(6)	C(38) - C(39)	1.526(7)
C(6) - C(9)	1.463(5)	C(39) - C(40)	1.497(7)

Table S3. Selected bond angles [°] for **2-BT·16C_6H_6**.

P(2) - Ru(1) - P(1)	173.41(4)	C(10) - C(9) - C(6)	127.1(4)
O(1) - Ru(1) - P(1)	86.88(7)	C(9) - C(10) - Ru(2)	135.2(3)
O(1) - Ru(1) - P(2)	88.14(7)	O(5) - C(11) - Ru(1)	177.1(3)
O(2) - Ru(1) - P(1)	91.38(7)	O(6) - C(12) - Ru(2)	177.4(3)
O(2) - Ru(1) - P(2)	89.64(7)	O(1) - C(13) - O(2)	119.8(3)
O(2) - Ru(1) - O(1)	57.99(9)	O(1) - C(13) - C(14)	120.5(3)
C(1) - Ru(1) - P(1)	89.88(11)	O(2) - C(13) - C(14)	119.4(3)
C(1) - Ru(1) - P(2)	96.62(11)	C(15) - C(14) - C(13)	120.4(3)
C(1) - Ru(1) - O(1)	148.22(12)	C(15) - C(14) - C(19)	119.2(3)
C(1) - Ru(1) - O(2)	90.53(13)	C(19) - C(14) - C(13)	120.0(3)
C(11) - Ru(1) - P(1)	90.69(12)	C(14) - C(15) - C(16)	120.5(3)
C(11) - Ru(1) - P(2)	88.08(12)	C(15) - C(16) - C(17)	120.8(4)
C(11) - Ru(1) - O(1)	120.19(13)	C(16) - C(17) - C(20)	121.5(3)
C(11) - Ru(1) - O(2)	177.14(14)	C(18) - C(17) - C(16)	118.1(3)
C(11) - Ru(1) - C(1)	91.44(16)	C(18) - C(17) - C(20)	120.4(3)
P(3) - Ru(2) - C(32)	87.95(9)	C(19) - C(18) - C(17)	121.1(3)
P(4) - Ru(2) - P(3)	177.47(3)	C(18) - C(19) - C(14)	120.3(4)
P(4) - Ru(2) - C(32)	89.85(8)	C(21) - C(20) - C(17)	121.8(3)
O(3) - Ru(2) - P(3)	88.60(7)	C(25) - C(20) - C(17)	120.9(3)
O(3) - Ru(2) - P(4)	88.87(7)	C(25) - C(20) - C(21)	117.2(3)
O(3) - Ru(2) - C(32)	29.06(10)	O(7) - C(21) - C(20)	116.2(3)
O(4) - Ru(2) - P(3)	88.79(7)	O(7) - C(21) - C(22)	122.3(3)
O(4) - Ru(2) - P(4)	89.92(7)	C(22) - C(21) - C(20)	121.5(3)
O(4) - Ru(2) - O(3)	58.47(9)	C(23) - C(22) - C(21)	119.2(4)
O(4) - Ru(2) - C(32)	29.41(10)	O(8) - C(23) - C(22)	122.5(3)
C(10) - Ru(2) - P(3)	90.23(11)	O(8) - C(23) - C(24)	116.6(3)
C(10) - Ru(2) - P(4)	92.09(11)	C(24) - C(23) - C(22)	120.9(3)
C(10) - Ru(2) - O(3)	155.37(13)	C(23) - C(24) - C(26)	120.4(3)
C(10) - Ru(2) - O(4)	96.92(13)	C(25) - C(24) - C(23)	118.1(3)
C(10) - Ru(2) - C(32)	126.31(14)	C(25) - C(24) - C(26)	121.3(3)

C(12) - Ru(2) - P(3)	91.55(13)	C(24) - C(25) - C(20)	123.1(4)
C(12) - Ru(2) - P(4)	89.58(13)	C(27) - C(26) - C(24)	121.2(3)
C(12) - Ru(2) - O(3)	117.49(13)	C(31) - C(26) - C(24)	120.1(3)
C(12) - Ru(2) - O(4)	175.94(13)	C(31) - C(26) - C(27)	118.8(3)
C(12) - Ru(2) - C(10)	87.13(16)	C(28) - C(27) - C(26)	120.4(3)
C(12) - Ru(2) - C(32)	146.55(14)	C(29) - C(28) - C(27)	120.0(4)
C(13) - O(1) - Ru(1)	87.2(2)	C(28) - C(29) - C(30)	120.1(3)
C(13) - O(2) - Ru(1)	94.5(2)	C(28) - C(29) - C(32)	120.5(3)
C(32) - O(3) - Ru(2)	88.1(2)	C(30) - C(29) - C(32)	119.4(3)
C(32) - O(4) - Ru(2)	93.3(2)	C(31) - C(30) - C(29)	119.3(3)
C(21) - O(7) - C(33)	119.2(3)	C(26) - C(31) - C(30)	121.3(4)
C(23) - O(8) - C(37)	117.0(3)	O(3) - C(32) - Ru(2)	62.80(18)
C(2) - C(1) - Ru(1)	139.7(3)	O(3) - C(32) - O(4)	120.0(3)
C(1) - C(2) - C(3)	126.5(3)	O(3) - C(32) - C(29)	120.6(3)
C(4) - C(3) - C(2)	120.2(3)	O(4) - C(32) - Ru(2)	57.24(17)
C(4) - C(3) - C(8)	116.8(3)	O(4) - C(32) - C(29)	119.4(3)
C(8) - C(3) - C(2)	123.0(4)	C(29) - C(32) - Ru(2)	176.4(3)
C(5) - C(4) - C(3)	121.4(3)	O(7) - C(33) - C(34)	106.7(3)
C(4) - C(5) - C(6)	122.4(4)	C(33) - C(34) - C(35)	113.3(3)
C(5) - C(6) - C(7)	115.8(3)	C(34) - C(35) - C(36)	112.1(3)
C(5) - C(6) - C(9)	121.0(4)	O(8) - C(37) - C(38)	109.3(3)
C(7) - C(6) - C(9)	123.2(3)	C(37) - C(38) - C(39)	114.1(4)
C(8) - C(7) - C(6)	121.6(3)	C(40) - C(39) - C(38)	114.5(4)
C(7) - C(8) - C(3)	121.9(4)		

Compound 2-NB:

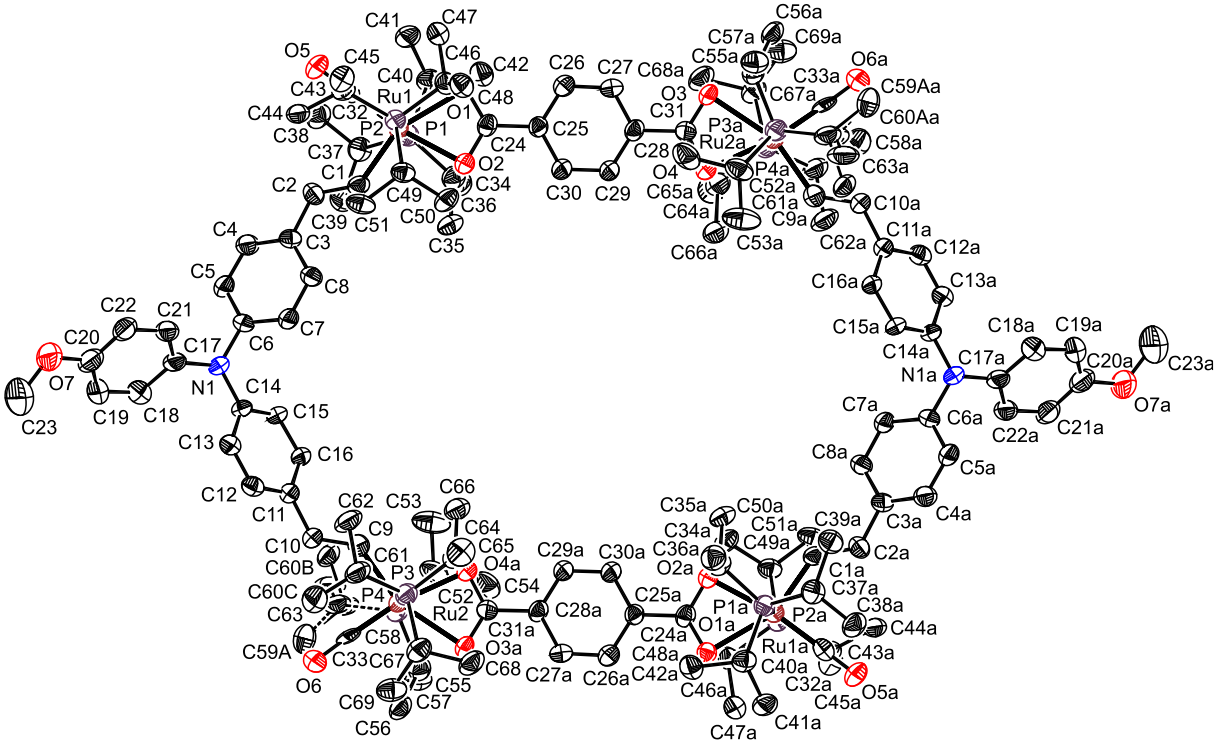

Figure S33. Structure of macrocycle **2-NB** as the benzene hexasolvate with atom numbering. Benzene solvate molecules as well as hydrogen atoms have been removed for clarity reasons. Ellipsoids are drawn at a 50% probability level.

Experimental. Single crystals of **2-NB** were obtained as yellow blocks by slow diffusion of methanol into a solution of compound **2-NB** in benzene. A suitable crystal was selected and mounted on a STOE IPDS-II diffractometer. The crystal was kept at 100.15 K during data collection. Using **Olex2**[1], the structure was solved with the **ShelXT**[2] structure solution program using Intrinsic Phasing and refined with the **ShelXL**[3] refinement package using Least Squares minimisation.

Table S4. Crystal data and structure refinement for macrocycle **2-NB·6C$_6$H$_6$**.

Empirical formula	$C_{138}H_{214}N_2O_{14}P_8Ru_4$	
Formula weight	2777.14	
Temperature	100.15 K	
Wavelength	0.71073 Å	
Crystal system	Triclinic	
Space group	*P* -1	
Unit cell dimensions	a = 11.0870(9) Å	α = 98.853(8) °
	b = 19.9232(17) Å	β = 100.783(8) °
	c = 21.192(2) Å	γ = 104.906(6) °
Volume	4342.0(7) Å^3	
Z	1	
Density (calculated)	1.062 Mg/m^3	
Absorption coefficient	0.462 mm^{-1}	
F(000)	1464.0	
Crystal size	0.1 x 0.2 x 0.3 mm^3	
2Θ range for data collection	3.874 to 51.996°	
Index ranges	$-13 \leq h \leq 13$, $-24 \leq k \leq 24$, $-26 \leq l \leq 26$	
Reflections collected	54977	
Independent reflections	17058 [R_{int} = 0.1729, R_{sigma} = 0.1343]	
Refinement method	Full-matrix least-squares on F^2	
Data / restraints / parameters	17058/3/787	
Goodness-of-fit on F^2	0.973	
Final R indices [I ≥ 2σ (I)]	R_1 = 0.1051, wR_2 = 0.2561	
R indices (all data)	R_1 = 0.1431, wR_2 = 0.2822	
Largest diff. peak and hole	2.42 and -1.84 e Å^{-3}	

Table S5. Selected bond lengths [Å] for **2-NB·6C$_6$H$_6$**.

Ru(1) - P(1)	2.410(2)	C(4) - C(5)	1.388(11)
Ru(1) - P(2)	2.428(2)	C(5) - C(6)	1.376(11)
Ru(1) - O(1)	2.271(5)	C(6) - C(7)	1.412(11)
Ru(1) - O(2)	2.191(5)	C(7) - C(8)	1.401(11)
Ru(1) - C(1)	2.022(7)	C(9) - C(10)	1.360(11)
Ru(1) - C(32)	1.797(8)	C(10) - C(11)	1.458(10)
Ru(2) - P(3)	2.401(3)	C(11) - C(12)	1.403(11)
Ru(2) - P(4)	2.435(2)	C(11) - C(16)	1.394(11)
Ru(2) - O(3)	2.309(5)	C(12) - C(13)	1.368(11)
Ru(2) - O(4)	2.189(5)	C(13) - C(14)	1.384(11)
Ru(2) - C(9)	2.021(8)	C(14) - C(15)	1.396(11)
Ru(2) - C(33)	1.760(8)	C(15) - C(16)	1.393(10)
O(1) - C(24)	1.240(9)	C(17) - C(18)	1.387(12)
O(2) - C(24)	1.298(9)	C(17) - C(22)	1.387(12)
O(3) - C(31)	1.255(9)	C(18) - C(19)	1.393(13)
O(4) - C(31)	1.274(9)	C(19) - C(20)	1.340(15)
O(5) - C(32)	1.186(10)	C(20) - C(21)	1.391(15)
O(6) - C(33)	1.223(10)	C(21) - C(22)	1.402(12)
O(7) - C(20)	1.405(12)	C(24) - C(25)	1.483(10)
O(7) - C(23)	1.451(19)	C(25) - C(26)	1.407(11)
N(1) - C(6)	1.443(10)	C(25) - C(30)	1.413(10)
N(1) - C(14)	1.412(9)	C(26) - C(27)	1.383(11)
N(1) - C(17)	1.441(11)	C(27) - C(28)	1.400(10)
C(1) - C(2)	1.341(11)	C(28) - C(29)	1.385(11)
C(2) - C(3)	1.469(10)	C(28) - C(31)	1.485(10)
C(3) - C(4)	1.369(11)	C(29) - C(30)	1.379(10)
C(3) - C(8)	1.399(11)		

Table S6. Selected bond angles [°] for **2-NB·6C$_6$H$_6$**.

P(1) - Ru(1) - P(2)	175.32(7)	C(8) - C(3) - C(2)	121.4(7)
P(1) - Ru(1) - C(24)	85.74(18)	C(3) - C(4) - C(5)	122.4(8)
P(2) - Ru(1) - C(24)	89.61(18)	C(6) - C(5) - C(4)	119.9(7)
O(1) - Ru(1) - P(1)	84.69(14)	C(5) - C(6) - N(1)	121.2(7)
O(1) - Ru(1) - P(2)	90.95(14)	C(5) - C(6) - C(7)	119.6(7)
O(1) - Ru(1) - C(24)	28.7(2)	C(7) - C(6) - N(1)	119.1(7)
O(2) - Ru(1) - P(1)	88.22(15)	C(8) - C(7) - C(6)	118.9(7)
O(2) - Ru(1) - P(2)	88.06(15)	C(3) - C(8) - C(7)	121.1(7)
O(2) - Ru(1) - O(1)	58.96(18)	C(10) - C(9) - Ru(2)	133.5(6)
O(2) - Ru(1) - C(24)	30.2(2)	C(9) - C(10) - C(11)	126.4(7)
C(1) - Ru(1) - P(1)	91.7(2)	C(12) - C(11) - C(10)	118.6(7)
C(1) - Ru(1) - P(2)	91.6(2)	C(16) - C(11) - C(10)	124.7(7)
C(1) - Ru(1) - O(1)	155.3(2)	C(16) - C(11) - C(12)	116.7(7)
C(1) - Ru(1) - O(2)	96.6(2)	C(13) - C(12) - C(11)	122.2(7)
C(1) - Ru(1) - C(24)	126.7(3)	C(12) - C(13) - C(14)	120.9(8)
C(32) - Ru(1) - P(1)	91.8(3)	C(13) - C(14) - N(1)	122.4(7)
C(32) - Ru(1) - P(2)	91.4(3)	C(13) - C(14) - C(15)	118.3(7)
C(32) - Ru(1) - O(1)	112.6(3)	C(15) - C(14) - N(1)	119.3(7)
C(32) - Ru(1) - O(2)	171.5(3)	C(16) - C(15) - C(14)	120.4(7)
C(32) - Ru(1) - C(1)	91.9(3)	C(15) - C(16) - C(11)	121.4(7)
C(32) - Ru(1) - C(24)	141.3(3)	C(18) - C(17) - N(1)	120.6(8)
P(3) - Ru(2) - P(4)	175.65(8)	C(22) - C(17) - N(1)	121.8(7)
P(3) - Ru(2) - C(31)	89.6(2)	C(22) - C(17) - C(18)	117.3(8)
P(4) - Ru(2) - C(31)	86.1(2)	C(17) - C(18) - C(19)	120.8(9)
O(3) - Ru(2) - P(3)	89.19(16)	C(20) - C(19) - C(18)	120.8(9)
O(3) - Ru(2) - P(4)	86.98(15)	C(19) - C(20) - O(7)	123.6(10)
O(3) - Ru(2) - C(31)	29.0(2)	C(19) - C(20) - C(21)	120.9(9)
O(4) - Ru(2) - P(3)	89.34(16)	C(21) - C(20) - O(7)	115.5(9)
O(4) - Ru(2) - P(4)	86.90(16)	C(20) - C(21) - C(22)	117.9(9)

O(4) - Ru(2) - O(3)	58.46(19)	C(17) - C(22) - C(21)	122.1(8)
O(4) - Ru(2) - C(31)	29.5(2)	O(1) - C(24) - Ru(1)	61.7(4)
C(9) - Ru(2) - P(3)	91.1(3)	O(1) - C(24) - O(2)	119.8(6)
C(9) - Ru(2) - P(4)	91.7(3)	O(1) - C(24) - C(25)	121.7(7)
C(9) - Ru(2) - O(3)	158.6(3)	O(2) - C(24) - Ru(1)	58.1(3)
C(9) - Ru(2) - O(4)	100.1(3)	O(2) - C(24) - C(25)	118.5(6)
C(9) - Ru(2) - C(31)	129.6(3)	C(25) - C(24) - Ru(1)	176.4(6)
C(33) - Ru(2) - P(3)	91.8(3)	C(26) - C(25) - C(24)	120.2(7)
C(33) - Ru(2) - P(4)	91.6(3)	C(26) - C(25) - C(30)	119.2(7)
C(33) - Ru(2) - O(3)	111.7(2)	C(30) - C(25) - C(24)	120.6(7)
C(33) - Ru(2) - O(4)	170.1(2)	C(27) - C(26) - C(25)	119.3(7)
C(33) - Ru(2) - C(9)	89.7(3)	C(26) - C(27) - C(28)	121.0(7)
C(33) - Ru(2) - C(31)	140.7(3)	C(27) - C(28) - C(31)	119.5(7)
C(24) - O(1) - Ru(1)	89.5(4)	C(29) - C(28) - C(27)	119.8(7)
C(24) - O(2) - Ru(1)	91.7(4)	C(29) - C(28) - C(31)	120.6(7)
C(31) - O(3) - Ru(2)	87.8(4)	C(30) - C(29) - C(28)	120.1(7)
C(31) - O(4) - Ru(2)	92.8(4)	C(29) - C(30) - C(25)	120.6(7)
C(20) - O(7) - C(23)	114.8(11)	O(3) - C(31) - Ru(2)	63.2(4)
C(14) - N(1) - C(6)	121.3(6)	O(3) - C(31) - O(4)	120.8(7)
C(14) - N(1) - C(17)	120.1(6)	O(3) - C(31) - C(28)	120.3(7)
C(17) - N(1) - C(6)	115.6(6)	O(4) - C(31) - Ru(2)	57.7(4)
C(2) - C(1) - Ru(1)	134.9(6)	O(4) - C(31) - C(28)	118.8(7)
C(1) - C(2) - C(3)	127.2(8)	C(28) - C(31) - Ru(2)	175.8(6)
C(4) - C(3) - C(2)	120.6(7)	O(5) - C(32) - Ru(1)	178.8(7)
C(4) - C(3) - C(8)	118.0(7)	O(6) - C(33) - Ru(2)	177.6(6)

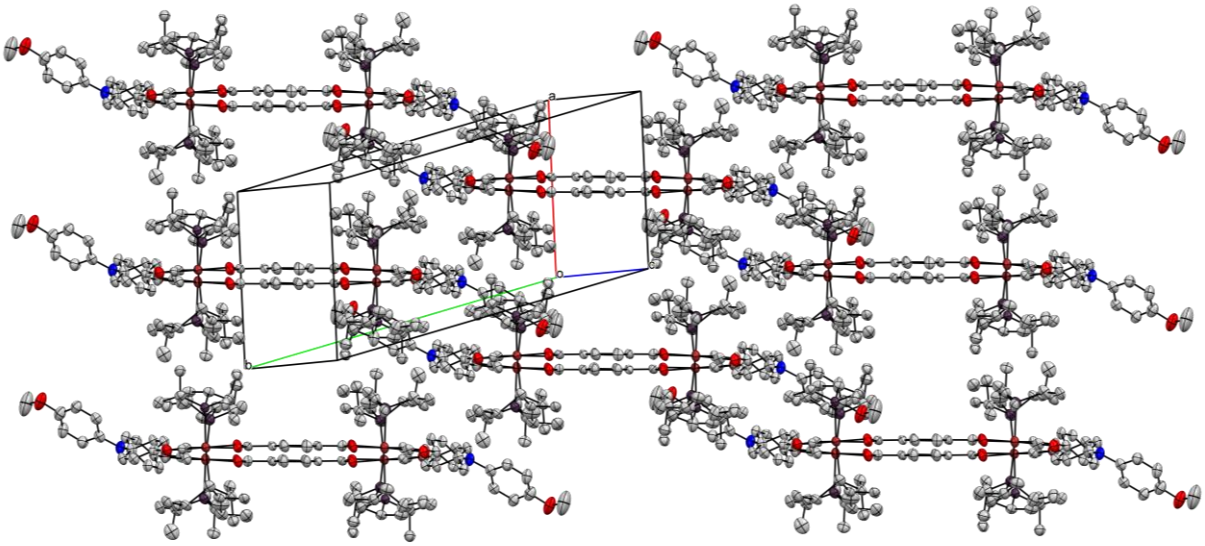

Figure S34. Packing diagram of individual **2-NB** molecules in the crystal. Benzene solvate molecules as well as hydrogen atoms have been removed for clarity reasons. Ellipsoids are drawn at a 50% probability level.

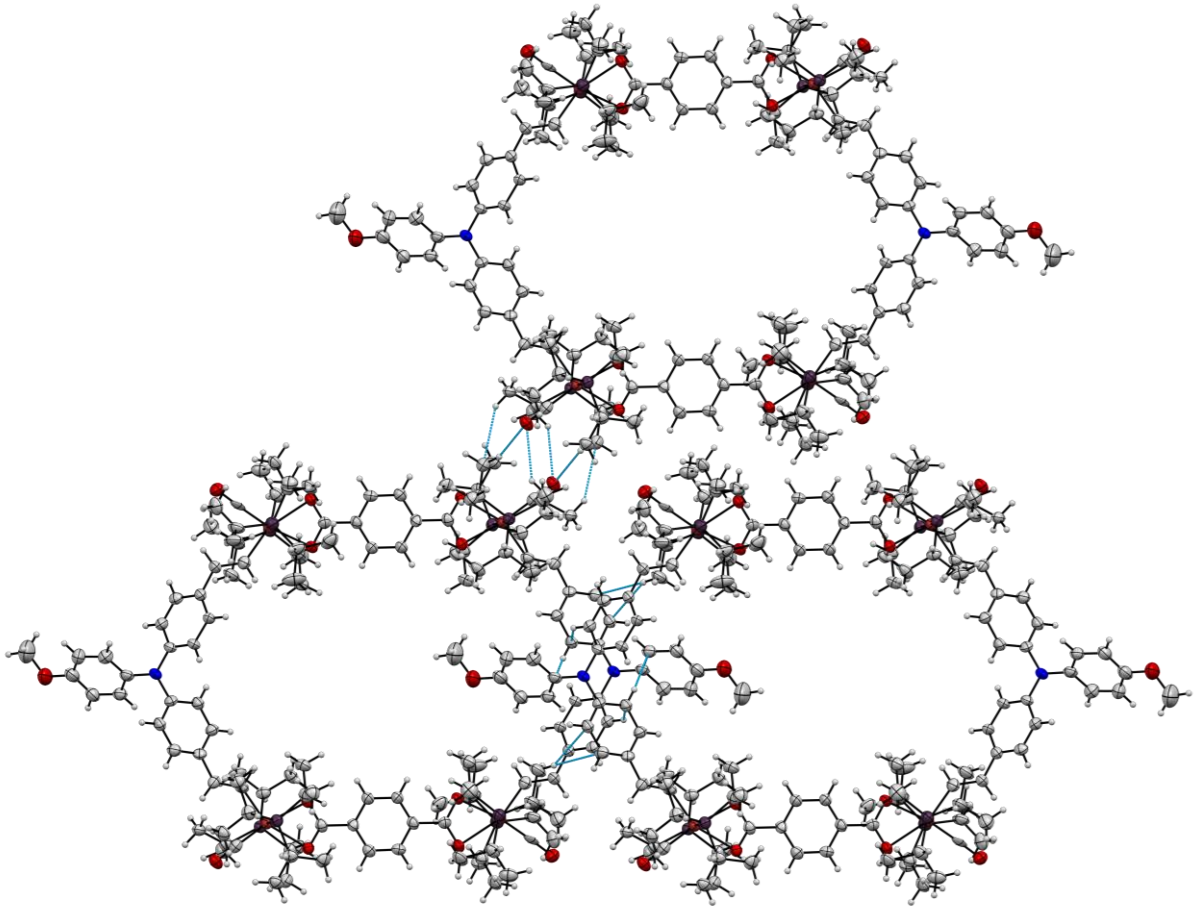

Figure S35. Hydrogen bonding motifs in the molecular structure of metallacycle **2-NB**. Benzene solvate molecules have been removed for clarity reasons. Ellipsoids are drawn at a 50% probability level.

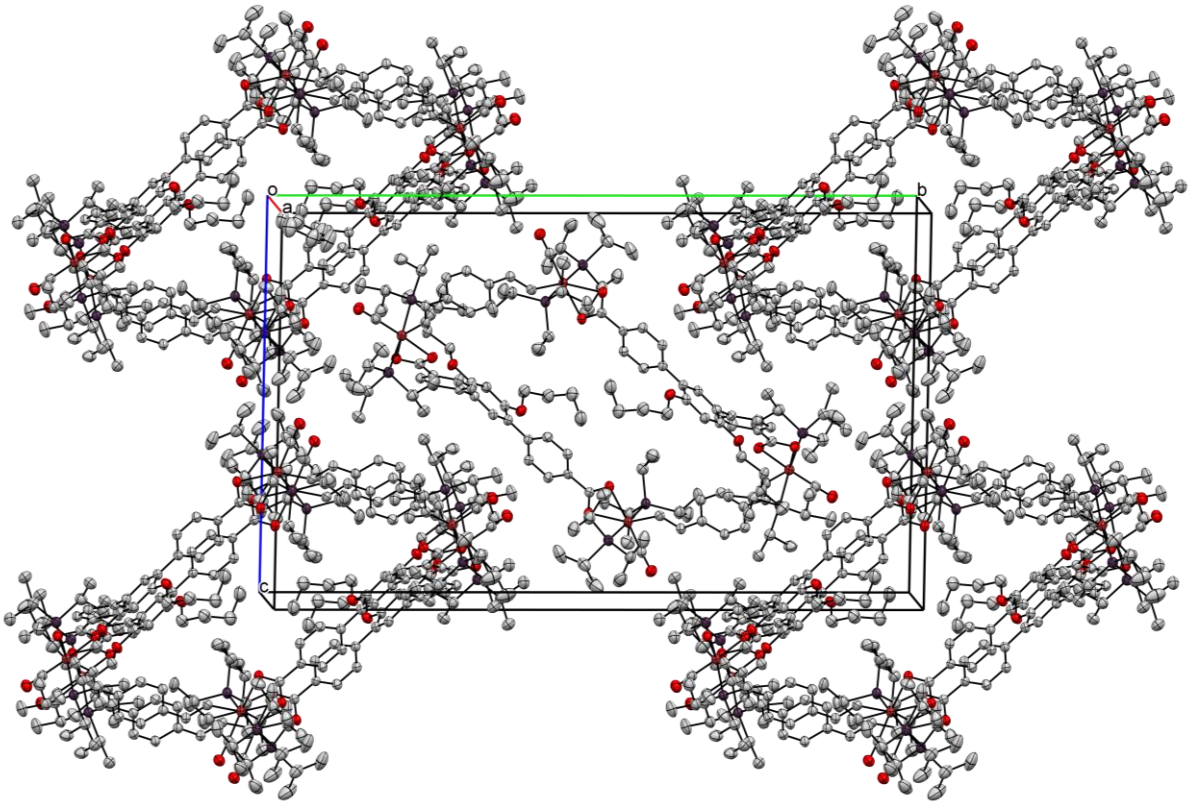

Figure S36. Packing diagram of individual **2-BT** molecules in the crystal. Benzene solvate molecules as well as hydrogen atoms have been removed for clarity reasons. Ellipsoids are drawn at a 50% probability level.

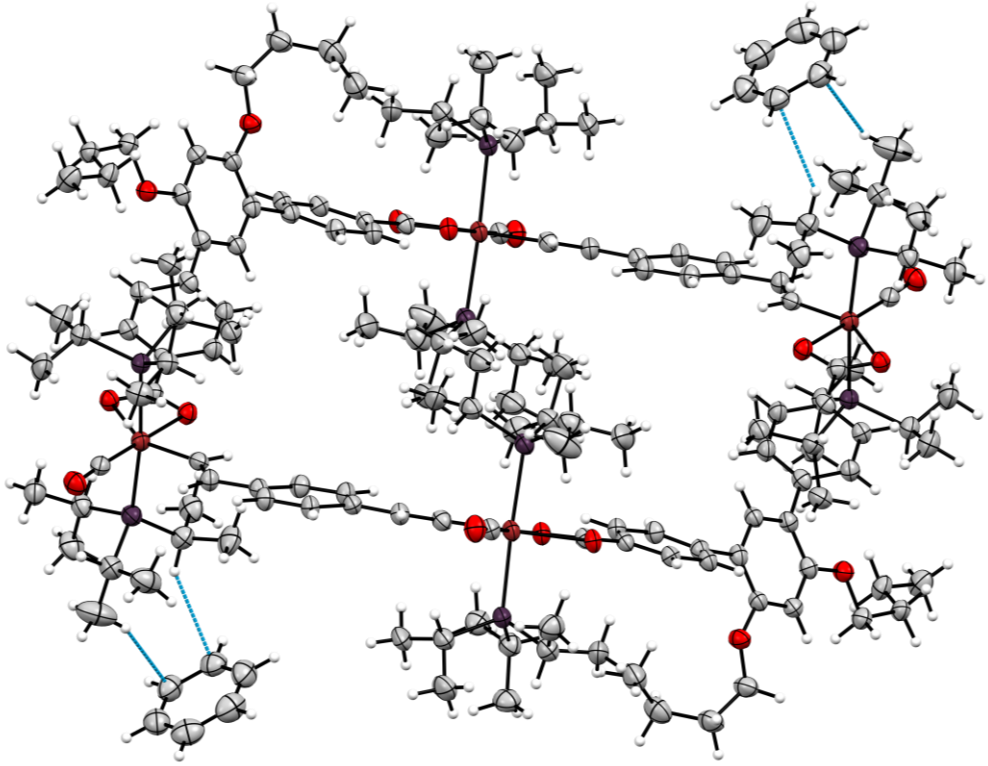

Figure S37. Hydrogen bonding motif in the molecular structure of metallacycle **2-BT**. Benzene solvate molecules have been removed for clarity reasons. Ellipsoids are drawn at a 50% probability level.

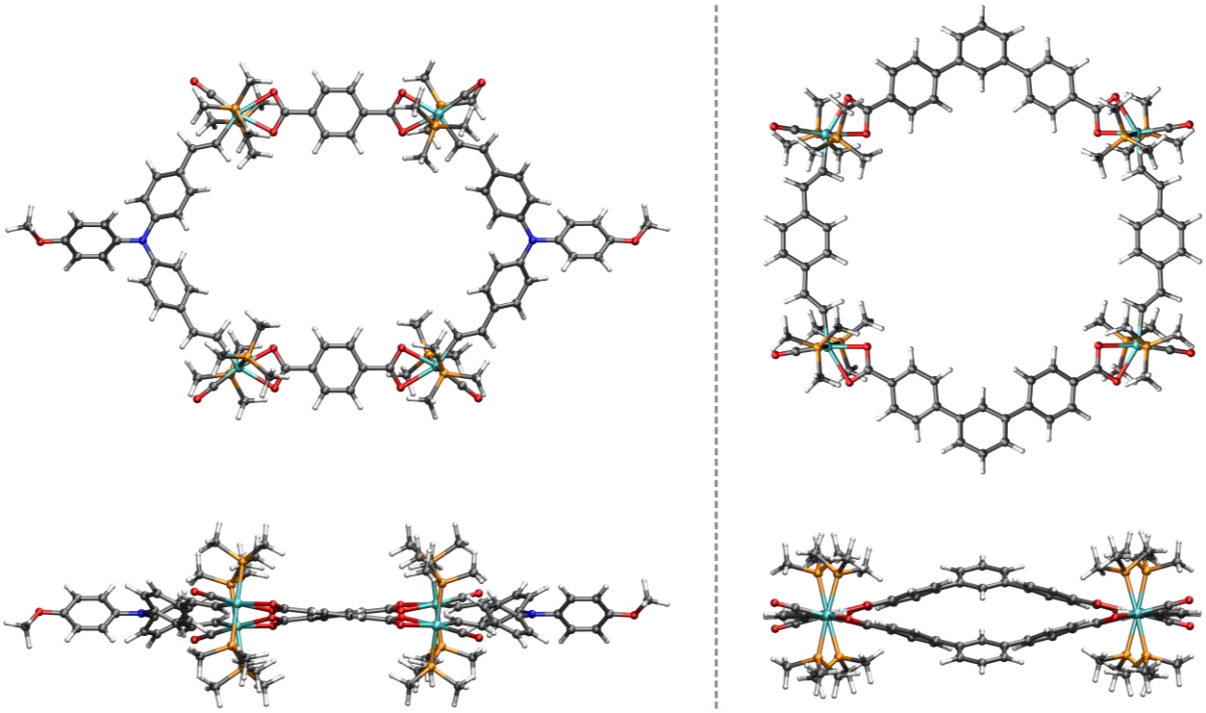

Figure S38. DFT-optimized structures of model compounds **2-NB^{Me}** (left) and **2-BT^{Me}** (right).

Cyclic Voltammetry

Compound 2-BT

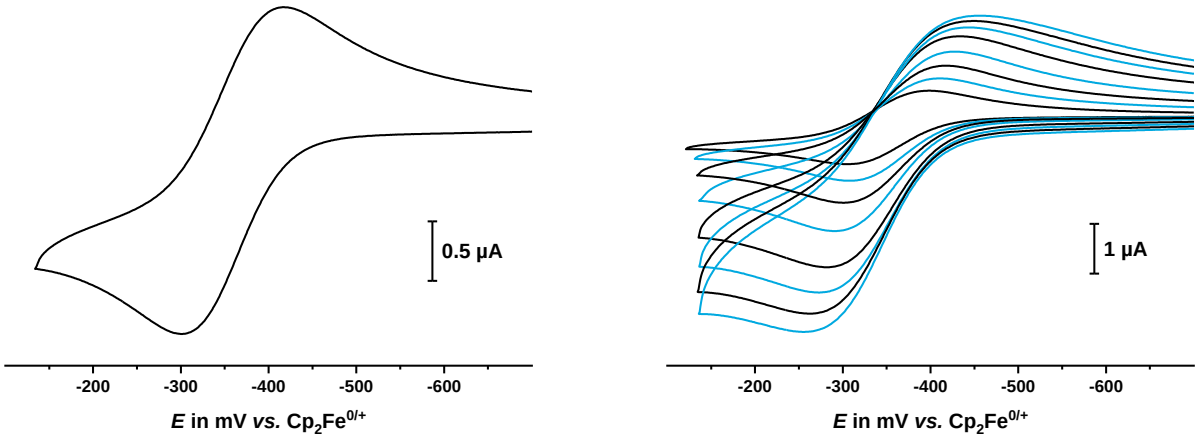

Figure S39. Cyclic voltammograms for the first composite wave of macrocycle **2-BT** at v = 100 mV/s (left) and at v = 25, 50, 100, 200, 400, 600, 800, 1000 mV/s (right) in CH_2Cl_2/^{n}Bu$_4$NBAr^{F24}.

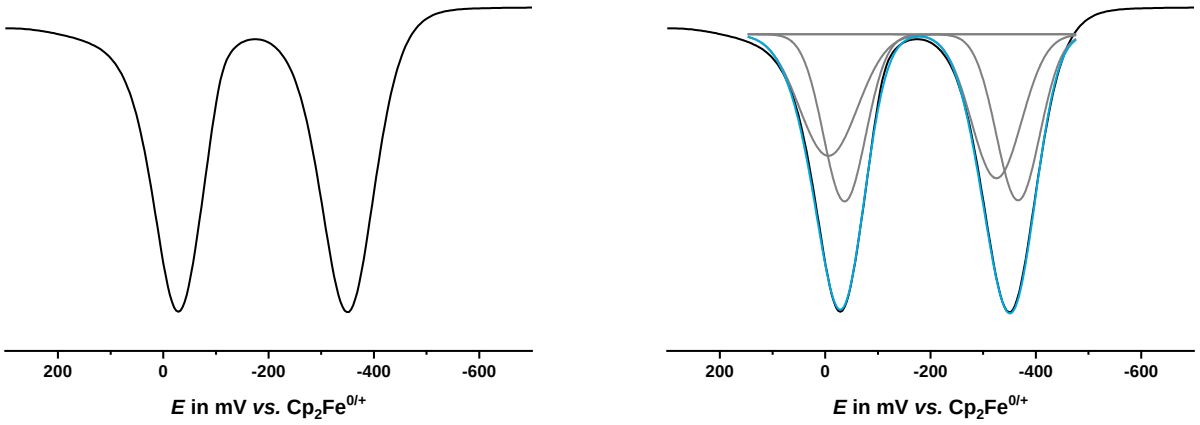

Figure S40. Square wave voltammogram of macrocycle **2-BT** (left) with deconvolution (right), measured in CH_2Cl_2/^{n}Bu$_4$NBAr^{F24}.

Compound 2-BTO:

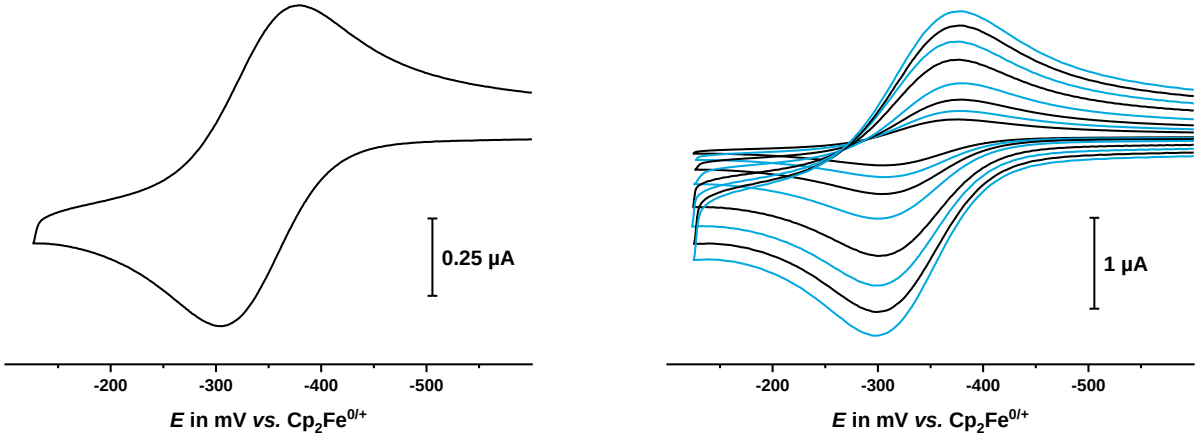

Figure S41. Cyclic voltammograms for the first composite wave of macrocycle **2-BTO** at v = 100 mV/s (left) and at v = 25, 50, 100, 200, 400, 600, 800, 1000 mV/s (right) in CH_2Cl_2/^{n}Bu$_4$NBAr^{F24}.

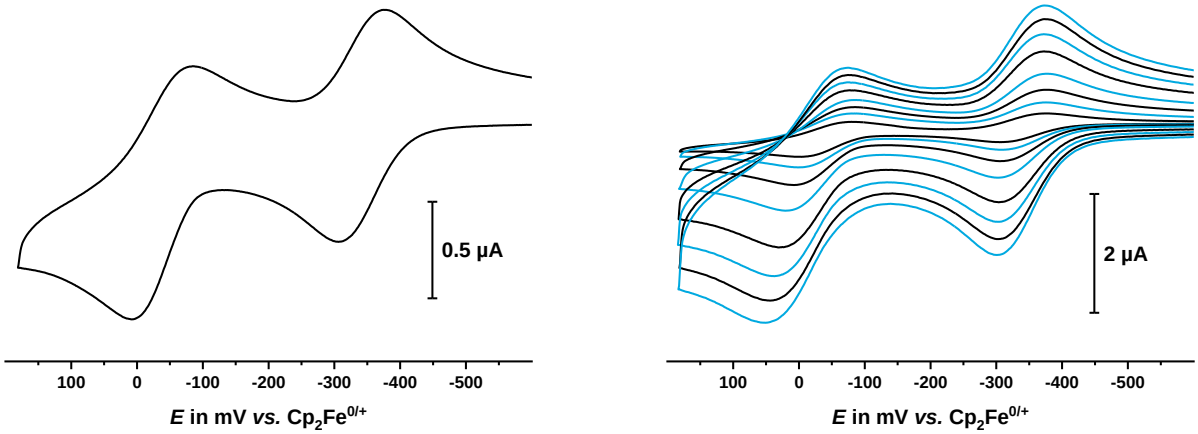

Figure S42. Cyclic voltammograms for the first two composite waves of macrocycle **2-BTO** at v = 100 mV/s (left) and at v = 25, 50, 100, 200, 400, 600, 800, 1000 mV/s (right) in CH_2Cl_2/^{n}Bu$_4$NBAr^{F24}.

Table S7. Data of the cyclovoltammetric measurements for macrocycle **2-BTO** at different scan rates, measured in $CH_2Cl_2/^nBu_4NBAr^{F24}$.

ν in mV/s	$E_{1/2}^{0/2+}$ in mV	$\Delta E_p^{0/2+}$ in mV	$E_{1/2}^{2+/4+}$ in mV	$\Delta E_p^{2+/4+}$ in mV	ΔE in mV
25	-340	71	-41	82	382
50	-342	68	-42	85	384
100	-341	69	-38	93	380
200	-340	75	-33	106	372
400	-338	69	-23	107	361
600	-337	70	-19	112	356
800	-338	73	-16	120	354
1000	-337	73	-11	127	348

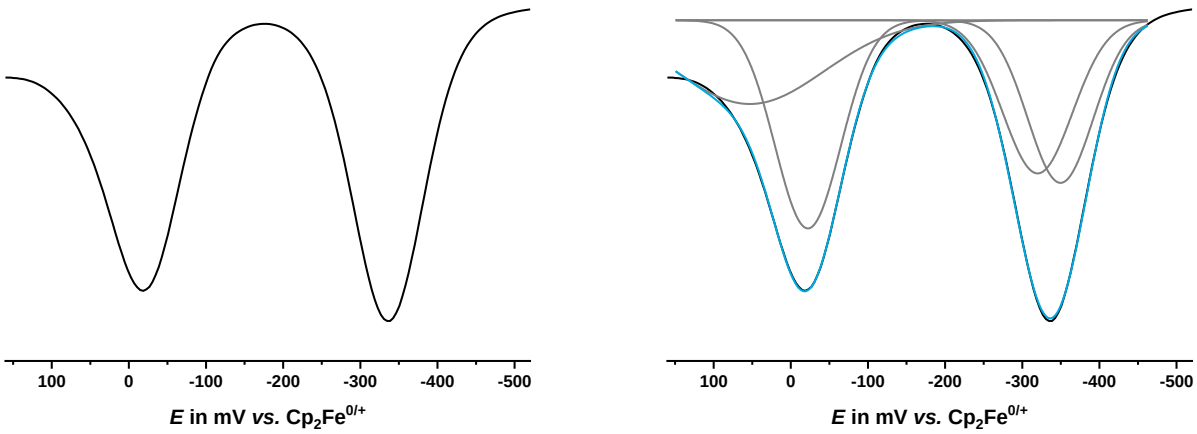

Figure S43. Square wave voltammogram of macrocycle **2-BTO** (left) with deconvolution (right), measured in $CH_2Cl_2/^nBu_4NBAr^{F24}$.

Compound 2-BTE:

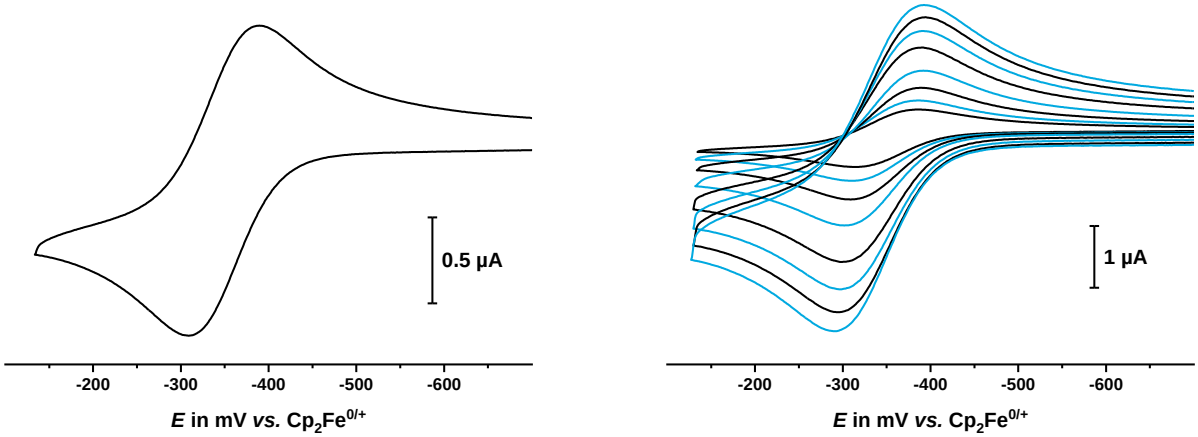

Figure S44. Cyclic voltammograms for the first composite wave of macrocycle **2-BTE** at v = 100 mV/s (left) and at v = 25, 50, 100, 200, 400, 600, 800, 1000 mV/s (right) in CH_2Cl_2/^{n}Bu$_4$NBAr^{F24}.

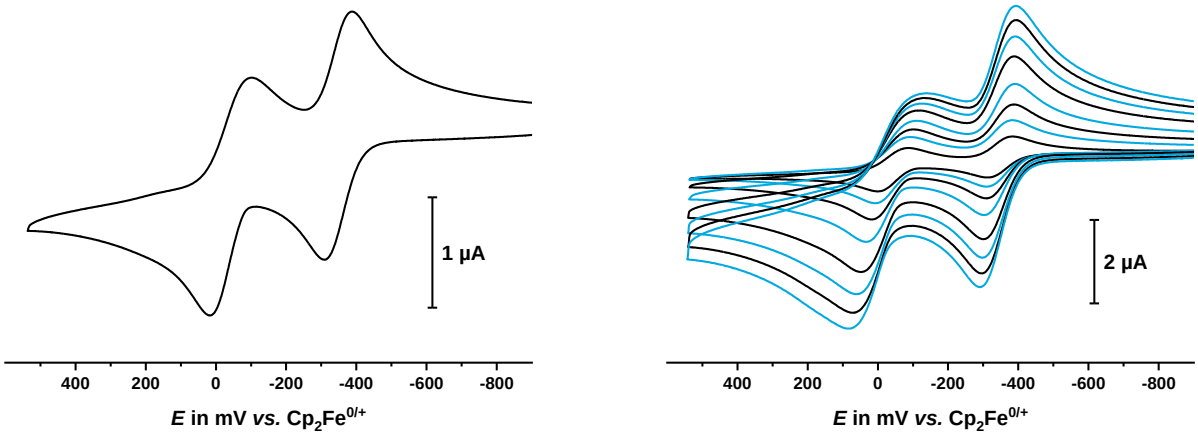

Figure S45. Cyclic voltammograms for the first two composite waves of macrocycle **2-BTE** at v = 100 mV/s (left) and at v = 25, 50, 100, 200, 400, 600, 800, 1000 mV/s (right) in CH_2Cl_2/^{n}Bu$_4$NBAr^{F24}.

Table S8. Data of the cyclovoltammetric measurements for macrocycle **2-BTE** at different scan rates, measured in $CH_2Cl_2/^nBu_4NBAr^{F24}$.

ν in mV/s	$E_{1/2}^{0/2+}$ in mV	$\Delta E_p^{0/2+}$ in mV	$E_{1/2}^{2+/4+}$ in mV	$\Delta E_p^{2+/4+}$ in mV	ΔE in mV
25	-350	71	-43	88	306
50	-348	78	-42	100	306
100	-349	81	-41	119	306
200	-347	90	-38	144	309
400	-345	90	-35	166	310
600	-344	94	-33	189	311
800	-344	99	-31	206	312
1000	-342	101	-27	222	316

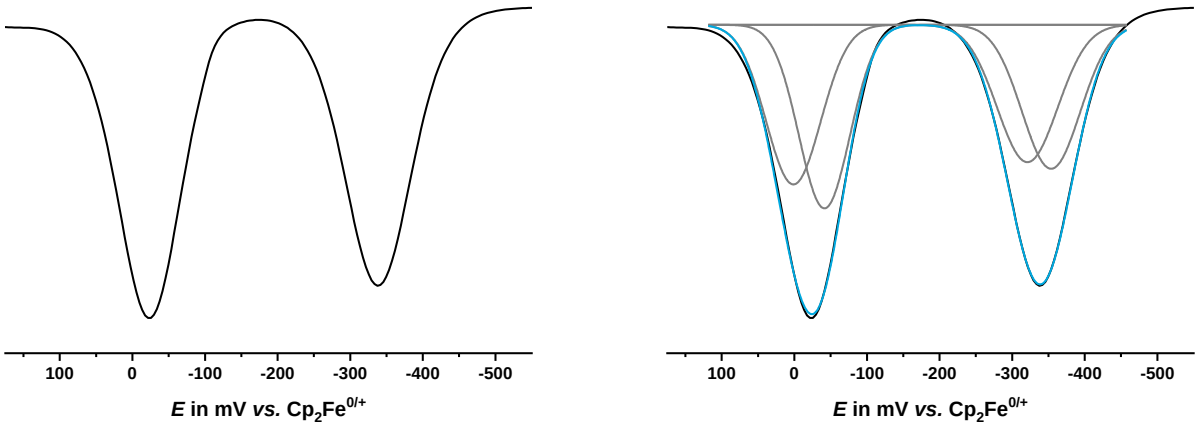

Figure S46. Square wave voltammogram of macrocycle **2-BTE** (left) with deconvolution (right), measured in $CH_2Cl_2/^nBu_4NBAr^{F24}$.

Compound 2-BN:

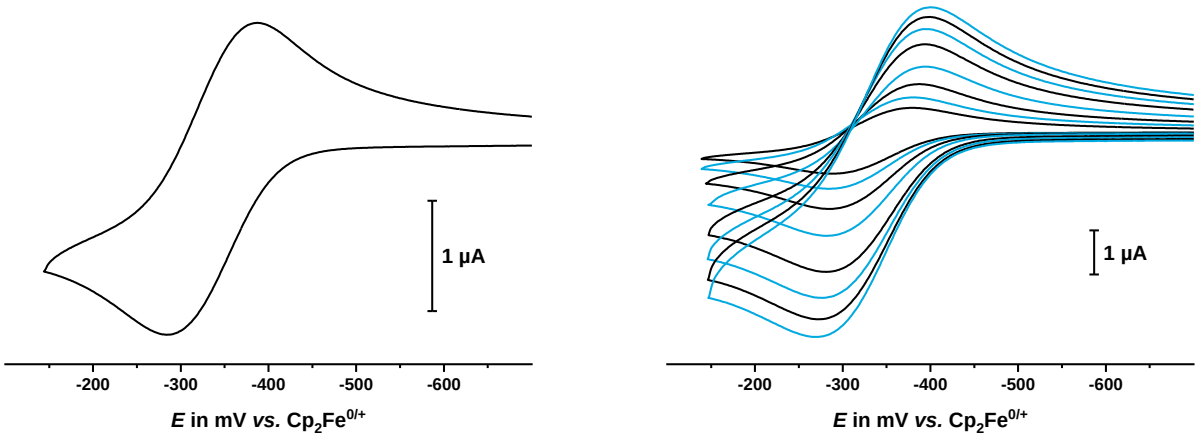

Figure S47. Cyclic voltammograms for the first composite wave of macrocycle **2-BN** at v = 100 mV/s (left) and at v = 25, 50, 100, 200, 400, 600, 800, 1000 mV/s (right) in CH_2Cl_2/^{n}Bu$_4$NBAr^{F24}.

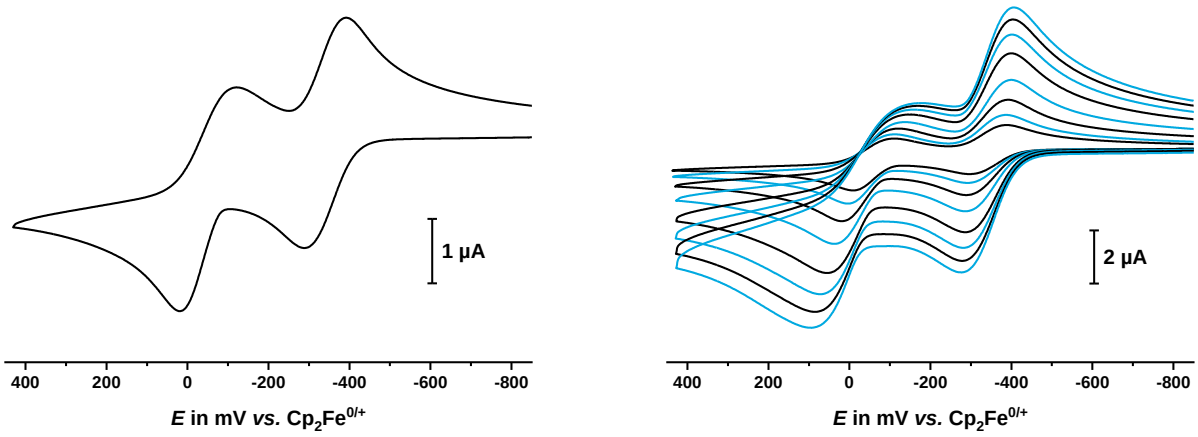

Figure S48. Cyclic voltammograms for the first two composite waves of macrocycle **2-BN** at v = 100 mV/s (left) and at v = 25, 50, 100, 200, 400, 600, 800, 1000 mV/s (right) in CH_2Cl_2/^{n}Bu$_4$NBAr^{F24}.

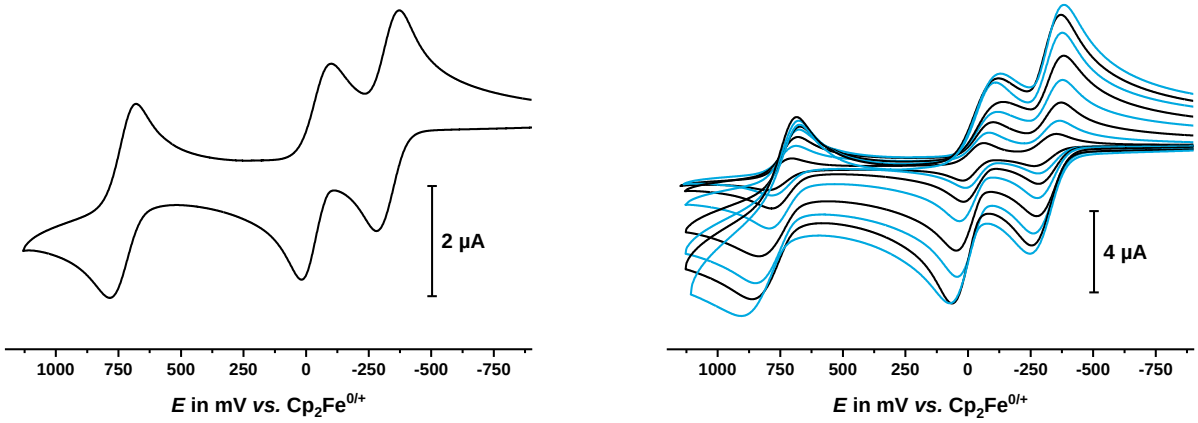

Figure S49. Cyclic voltammograms for the first three composite waves of macrocycle **2-BN** at v = 100 mV/s (left) and at v = 25, 50, 100, 200, 400, 600, 800, 1000 mV/s (right) in CH_2Cl_2/^{n}Bu$_4$NBAr^{F24}.

Table S9. Data of the cyclovoltammetric measurements for macrocycle **2-BN** at different scan rates, measured in $CH_2Cl_2/^nBu_4NBAr^{F24}$.

v in mV/s	$E_{1/2}^{0/2+}$ in mV	$\Delta E_p^{0/2+}$ in mV	$E_{1/2}^{2+/4+}$ in mV	$\Delta E_p^{2+/4+}$ in mV	$E_{1/2}^{4+/6+}$ in mV	$\Delta E_p^{4+/6+}$ in mV
25	-319	92	-47	102	752	99
50	-332	96	-54	115	735	97
100	-336	103	-51	140	733	104
200	-338	112	-50	175	735	119
400	-337	113	-46	204	755	164
600	-336	120	-43	232	762	175
800	-335	126	-42	256	774	179
1000	-335	132	-41	271	784	182

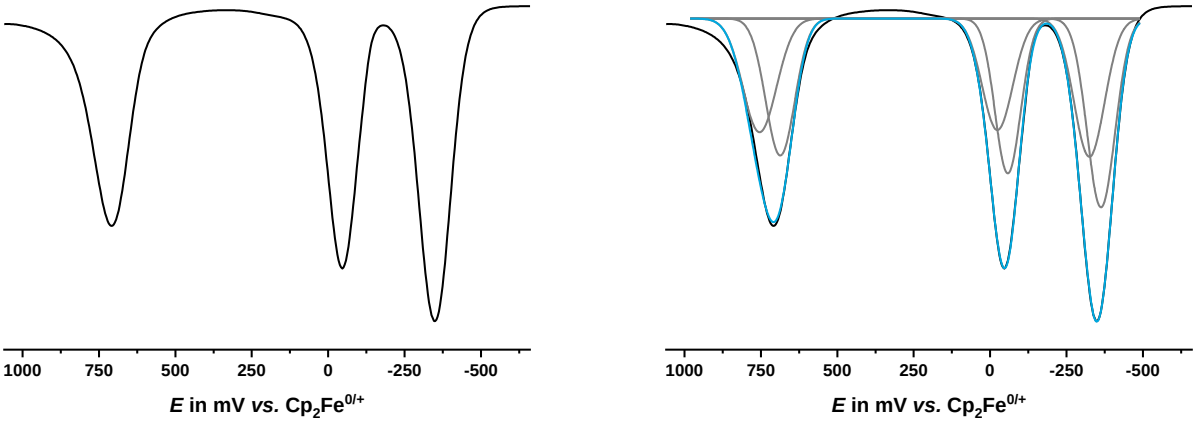

Figure S50. Square wave voltammogram of macrocycle **2-BN** (left) with deconvolution (right), measured in $CH_2Cl_2/^nBu_4NBAr^{F24}$.

Compound 2-NB:

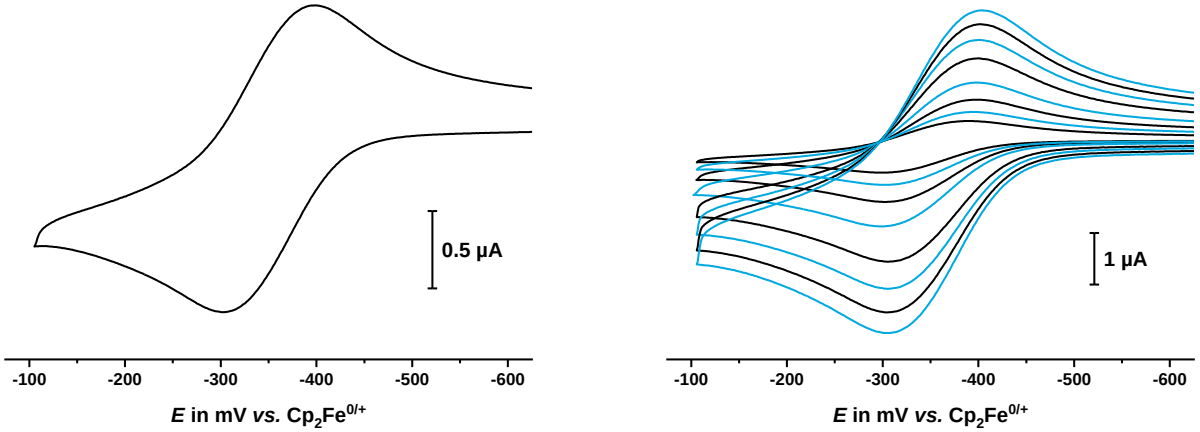

Figure S51. Cyclic voltammograms for the first composite wave of macrocycle **2-NB** at v = 100 mV/s (left) and at v = 25, 50, 100, 200, 400, 600, 800, 1000 mV/s (right) in CH_2Cl_2/^{n}Bu$_4$NBAr^{F24}.

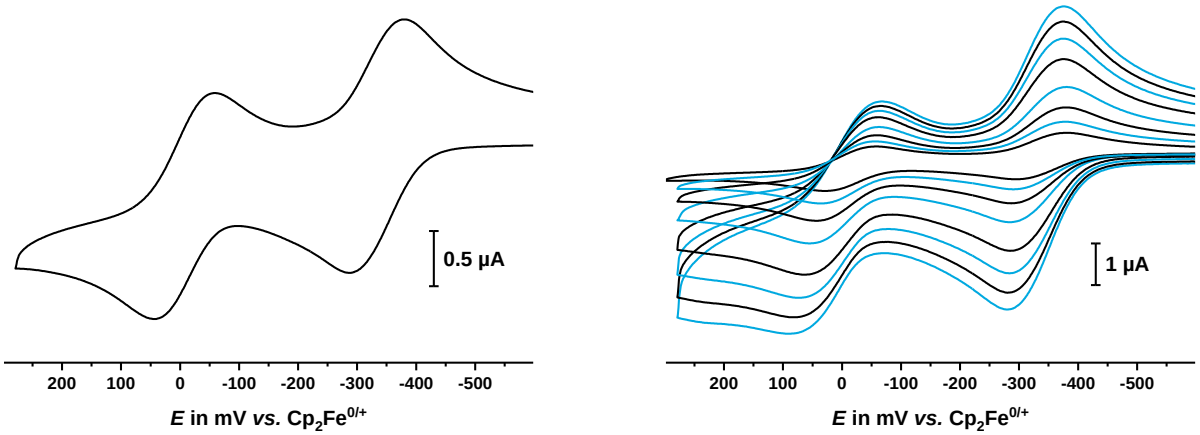

Figure S52. Cyclic voltammograms for the first two composite waves of macrocycle **2-NB** at v = 100 mV/s (left) and at v = 25, 50, 100, 200, 400, 600, 800, 1000 mV/s (right) in CH_2Cl_2/^{n}Bu$_4$NBAr^{F24}.

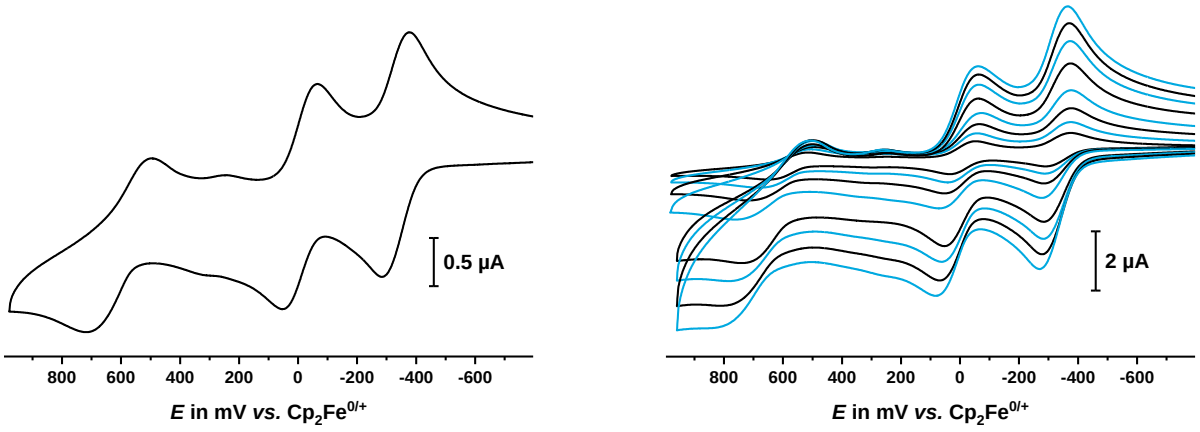

Figure S53. Cyclic voltammograms for the first two composite waves of macrocycle **2-NB** at v = 100 mV/s (left) and at v = 25, 50, 100, 200, 400, 600, 800, 1000 mV/s (right) in CH_2Cl_2/^{n}Bu$_4$NBAr^{F24}.

Table S10. Data of the cyclovoltammetric measurements for macrocycle **2-NB** at different scan rates, measured in $CH_2Cl_2/^nBu_4NBAr^{F24}$.

v in mV/s	$E_{1/2}^{0/2+}$ in mV	$\Delta E_p^{0/2+}$ in mV	$E_{1/2}^{2+/4+}$ in mV	$\Delta E_p^{2+/4+}$ in mV	$E_{1/2}^{4+/6+}$ in mV	$\Delta E_p^{4+/6+}$ in mV
25	-346	90	-93	95	501	135
50	-349	93	-10	94	593	175
100	-350	96	-7	102	605	227
200	-348	99	-1	117	627	271
400	-345	95	8	124	647	238
600	-345	95	13	138	668	284
800	-343	97	18	150	686	311
1000	-343	100	23	157	707	343

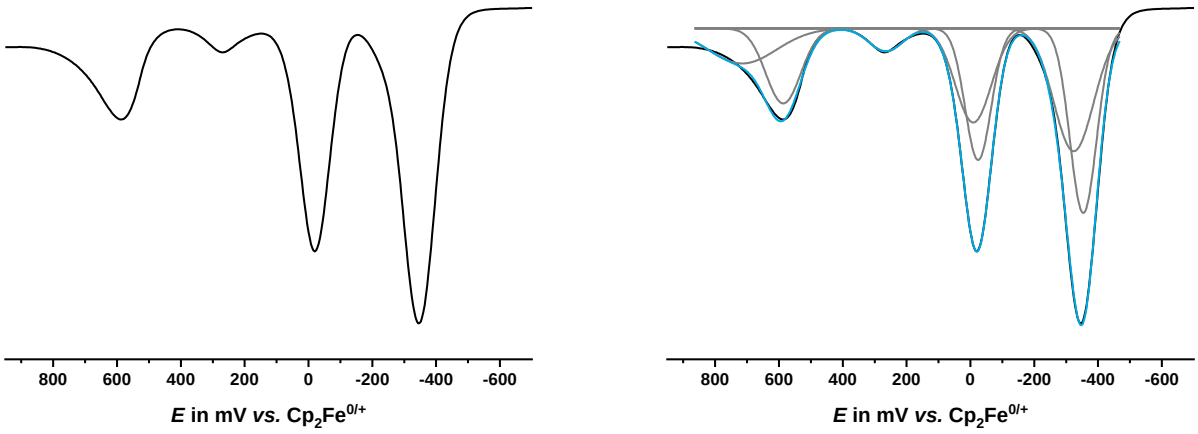

Figure S54. Square wave voltammogram of macrocycle **2-NB** (left) with deconvolution (right), measured in $CH_2Cl_2/^nBu_4NBAr^{F24}$.

Spectroelectrochemistry

Compound 2-BT:

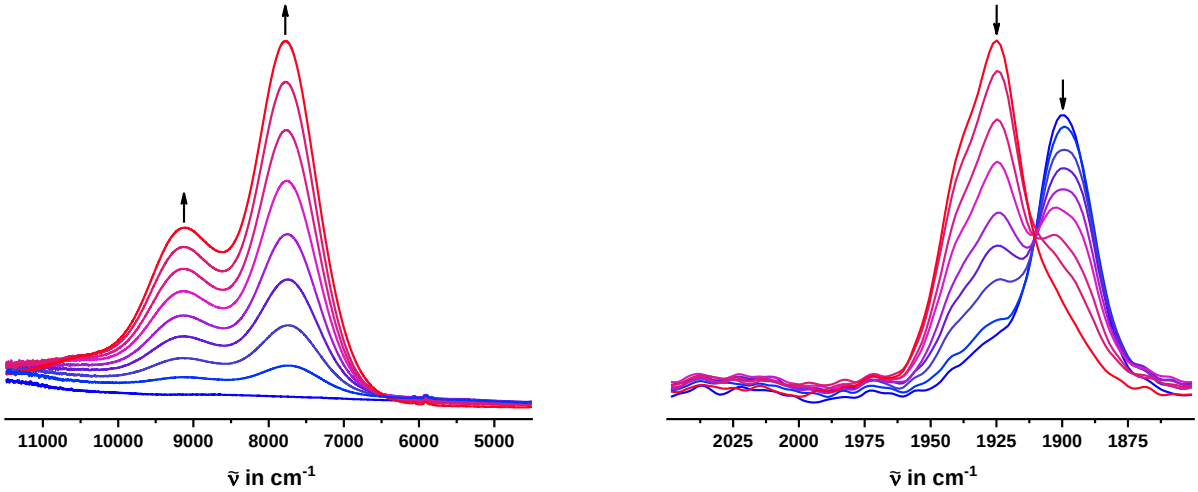

Figure S55. Changes in the IR spectra of **2-BT** upon oxidation to **2-BT**$^{2+}$, measured in $CH_2Cl_2/^nBu_4NPF_6$.

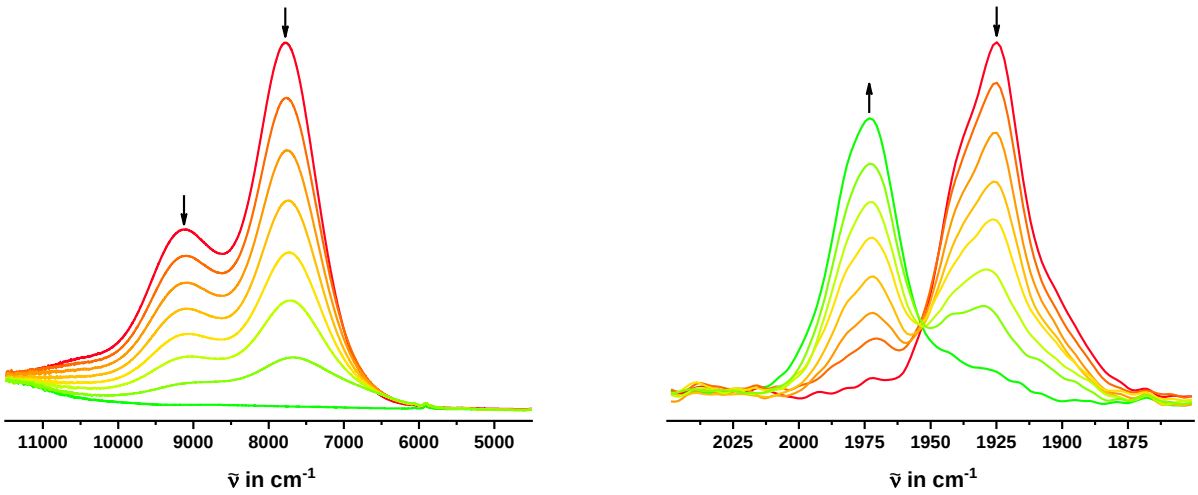

Figure S56. Changes in the IR spectra of **2-BT**$^{2+}$ upon oxidation to **2-BT**$^{4+}$, measured in $CH_2Cl_2/^nBu_4NPF_6$.

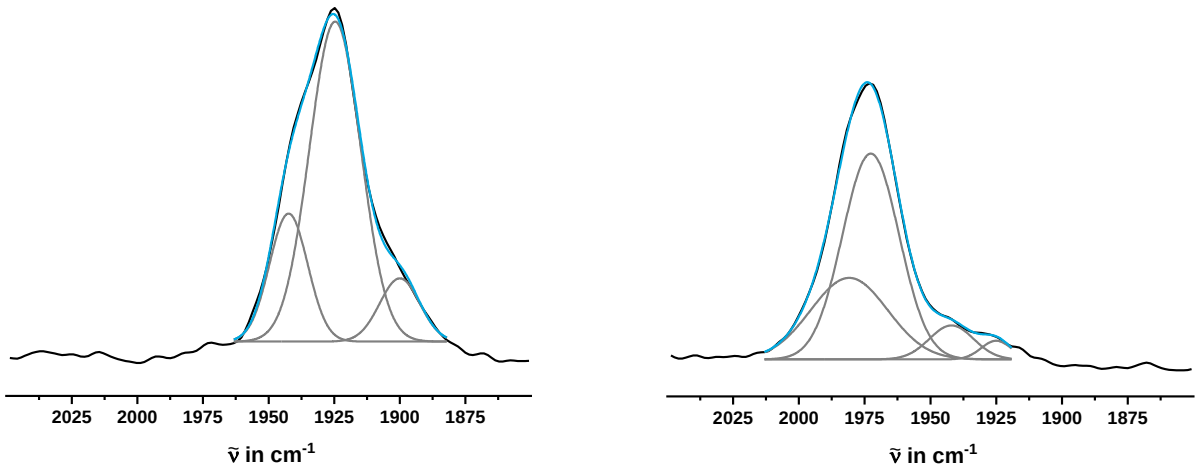

Figure S57. Deconvolutions of the Carbonyl bands of **2-BT**$^{2+}$ (left) and **2-BT**$^{4+}$ (right).

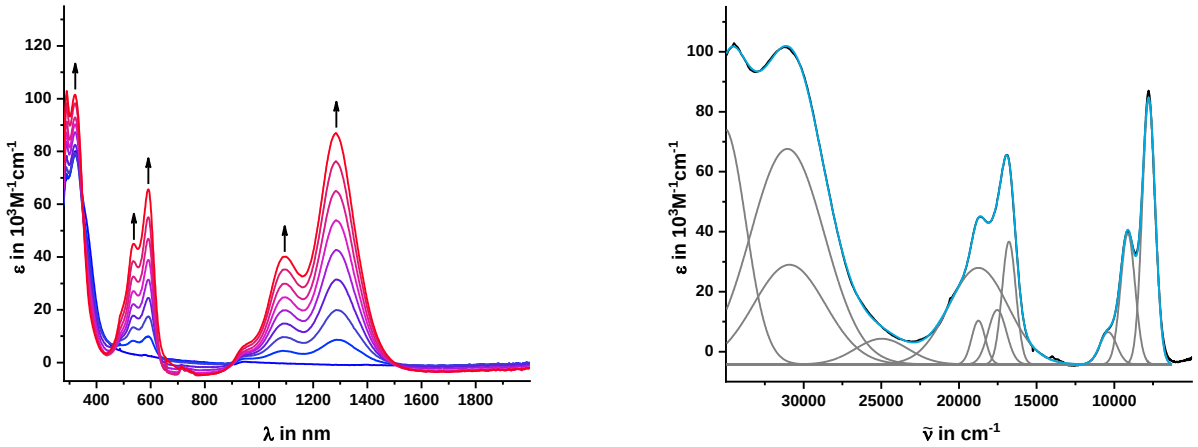

Figure S58. Changes in the UV/Vis/NIR spectra of **2-BT** upon oxidation to **2-BT**$^{2+}$ (left) and deconvolution (right), measured in CH_2Cl_2/^{n}Bu$_4$NPF$_6$.

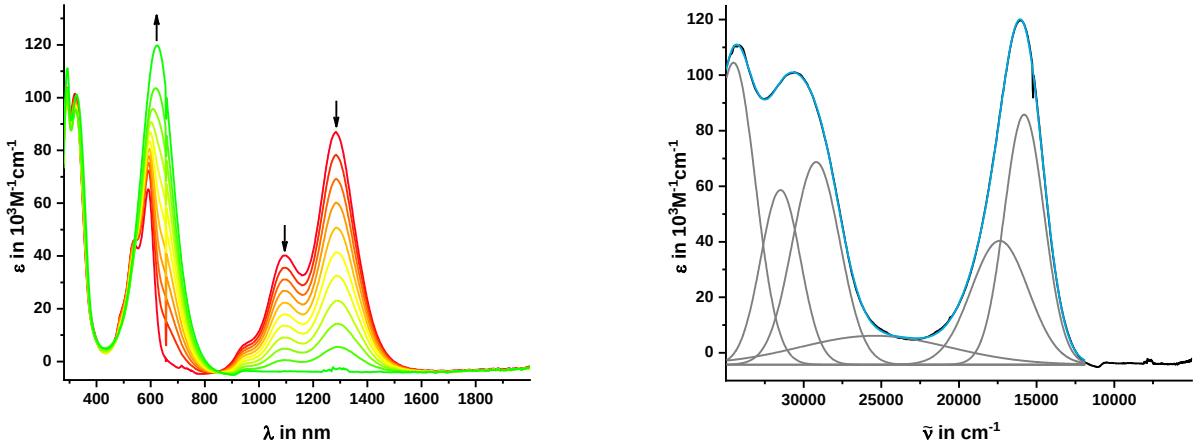

Figure S59. Changes in the UV/Vis/NIR spectra of **2-BT**$^{2+}$ upon oxidation to **2-BT**$^{4+}$ (left) and deconvolution (right), measured in CH_2Cl_2/^{n}Bu$_4$NPF$_6$.

Compound 2-BTO:

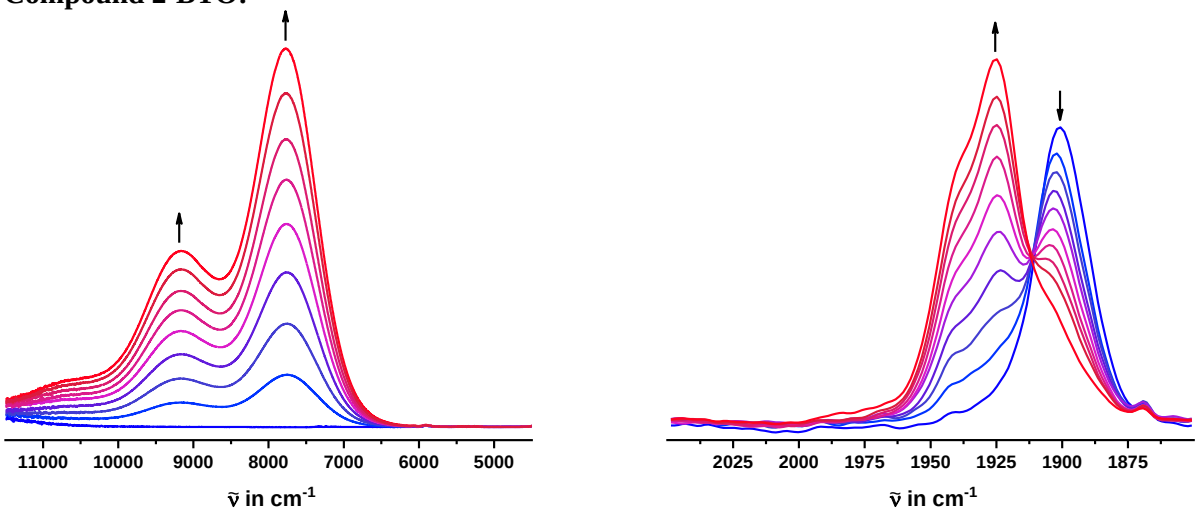

Figure S60. Changes in the IR spectra of **2-BTO** upon oxidation to **2-BTO^{2+}**, measured in CH_2Cl_2/^{n}Bu$_4$NPF$_6$.

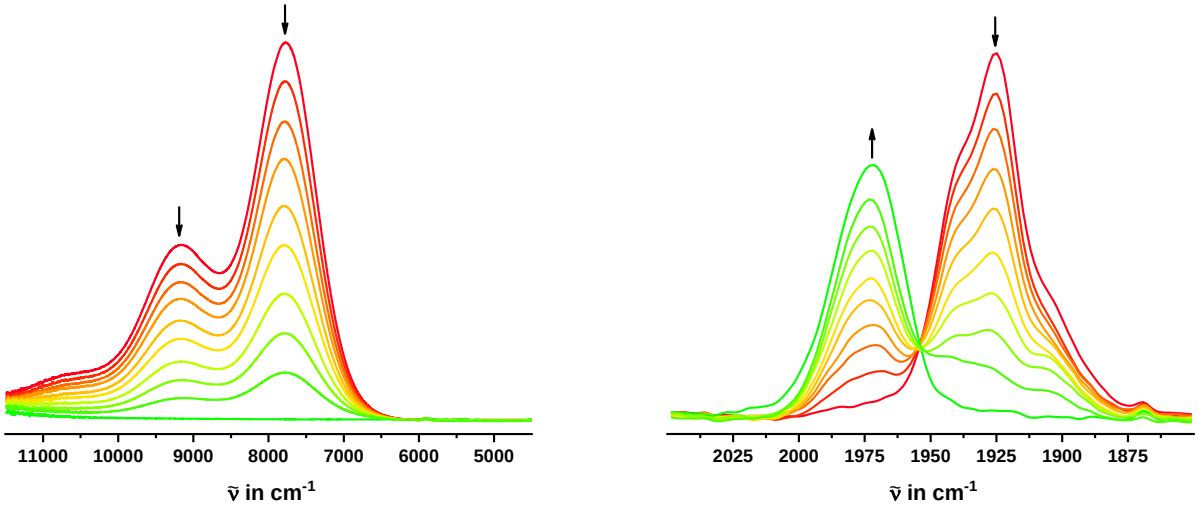

Figure S61. Changes in the IR spectra of **2-BTO^{2+}** upon oxidation to **2-BTO^{4+}**, measured in CH_2Cl_2/^{n}Bu$_4$NPF$_6$.

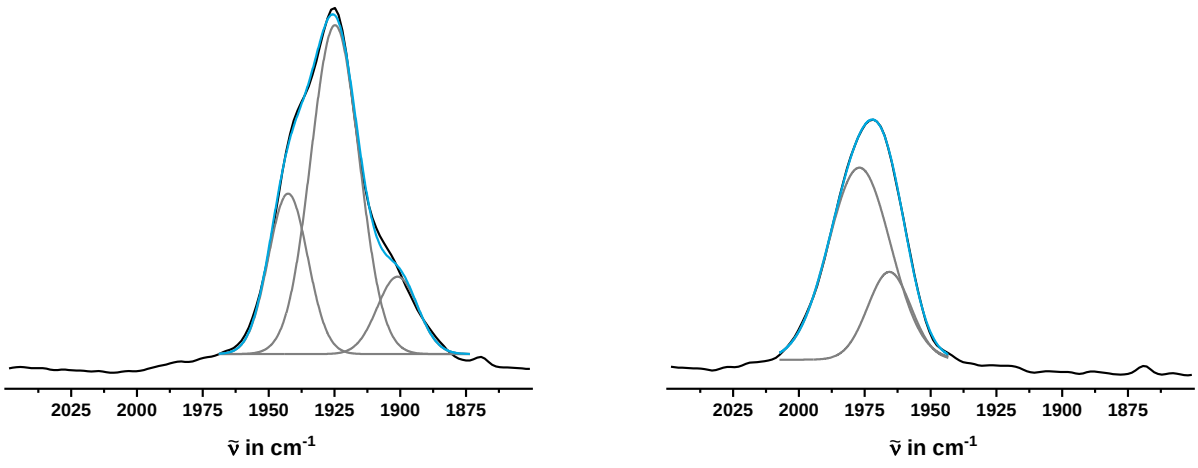

Figure S62. Deconvolutions of the Carbonyl bands of **2-BTO^{2+}** (left) and **2-BTO^{4+}** (right).

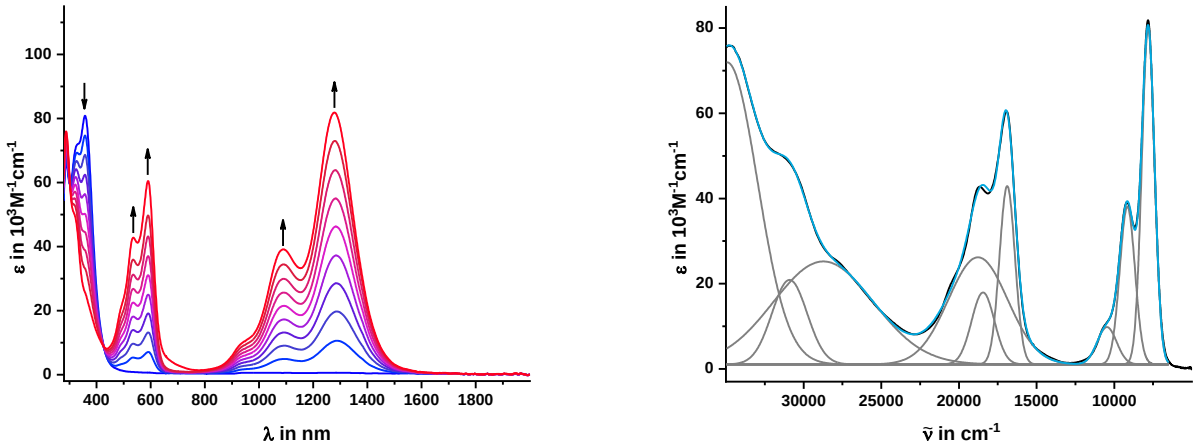

Figure S63. Changes in the UV/Vis/NIR spectra of **2-BTO** upon oxidation to **2-BTO**$^{2+}$ (left) and deconvolution (right), measured in CH_2Cl_2/^{n}Bu$_4$NPF$_6$.

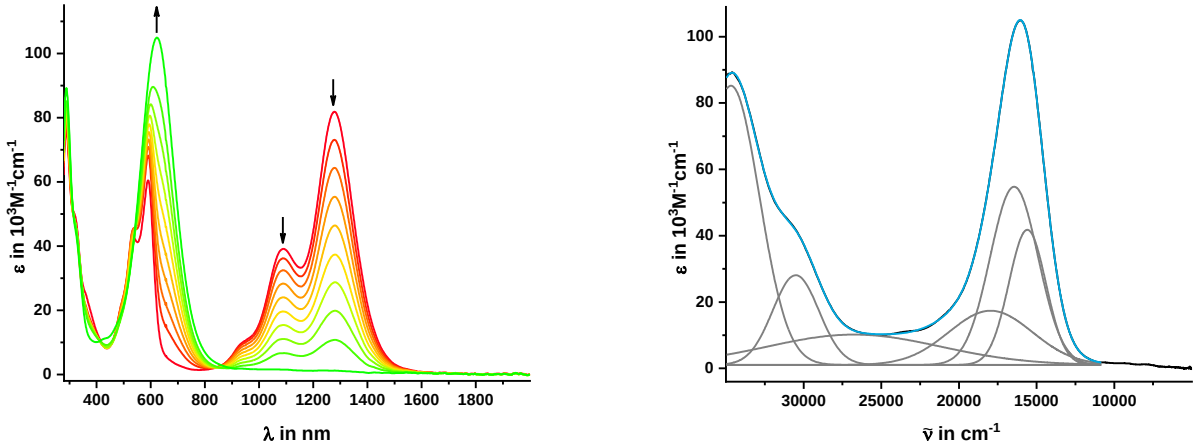

Figure S64. Changes in the UV/Vis/NIR spectra of **2-BTO**$^{2+}$ upon oxidation to **2-BTO**$^{4+}$ (left) and deconvolution (right), measured in CH_2Cl_2/^{n}Bu$_4$NPF$_6$.

Compound 2-BTE:

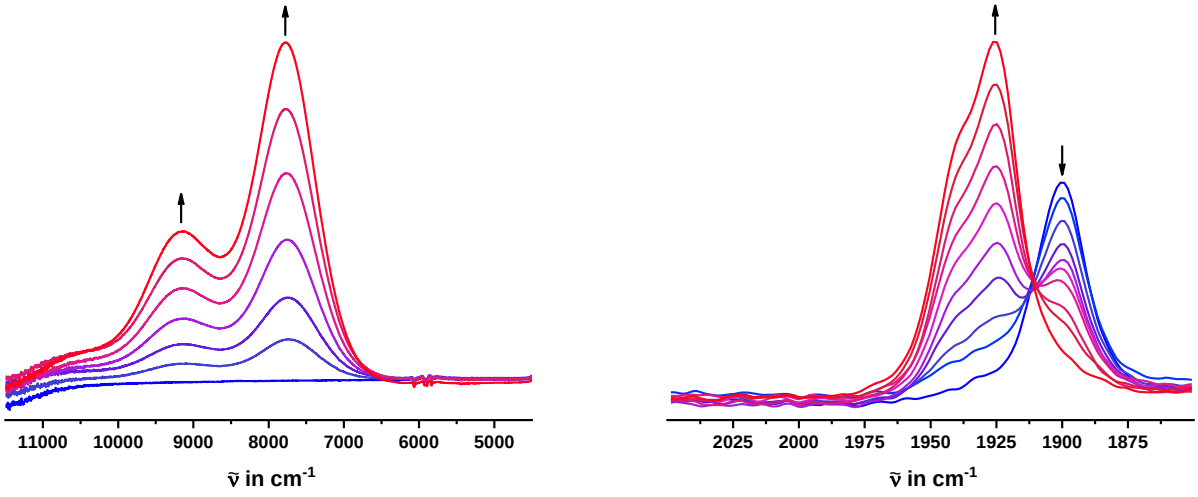

Figure S65. Changes in the IR spectra of **2-BTE** upon oxidation to **2-BTE**$^{2+}$, measured in $CH_2Cl_2/^nBu_4NPF_6$.

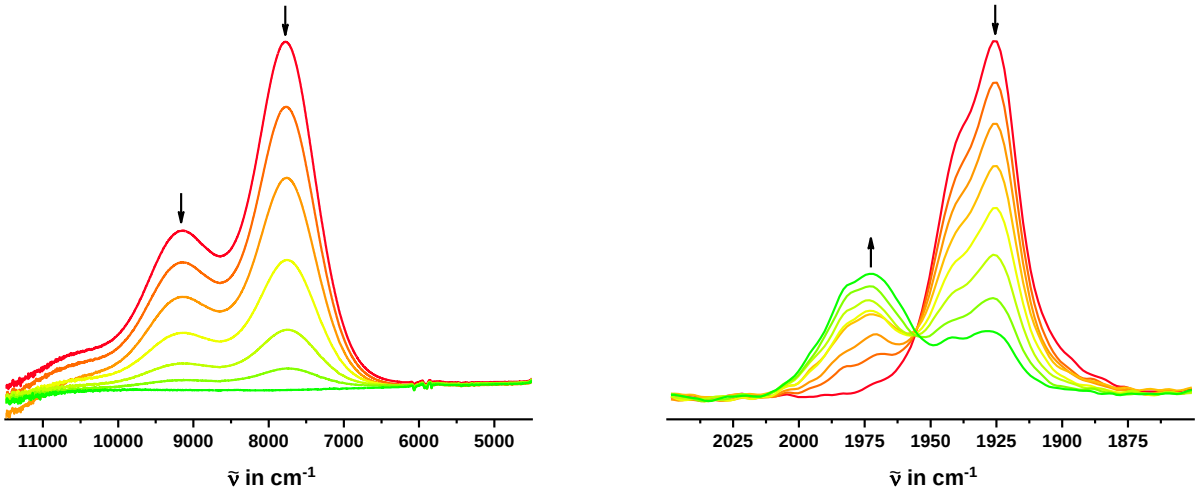

Figure S66. Changes in the IR spectra of **2-BTE**$^{2+}$ upon oxidation to **2-BTE**$^{4+}$, measured in $CH_2Cl_2/^nBu_4NPF_6$.

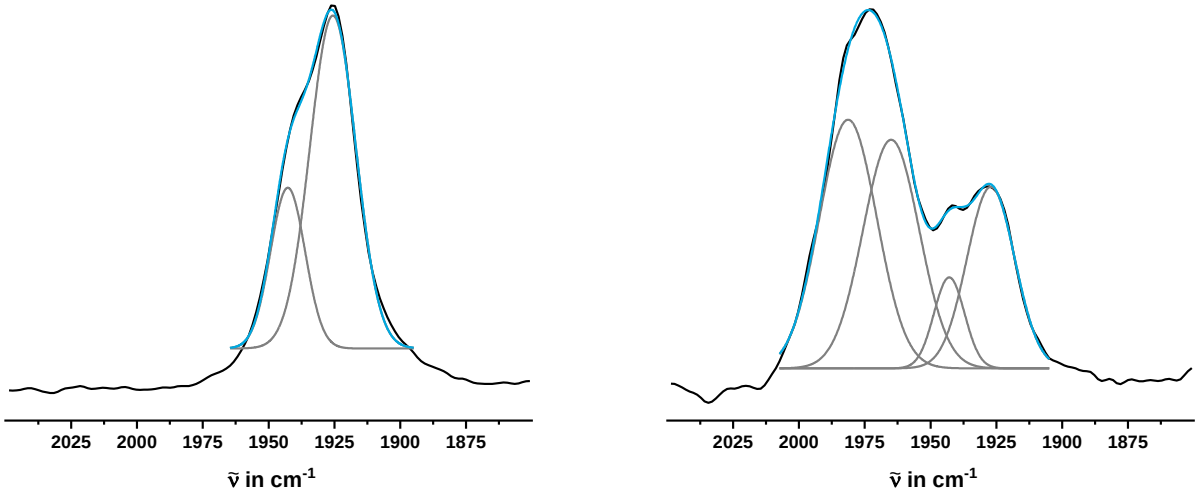

Figure S67. Deconvolutions of the Carbonyl bands of **2-BTE**$^{2+}$ (left) and **2-BTE**$^{4+}$ (right).

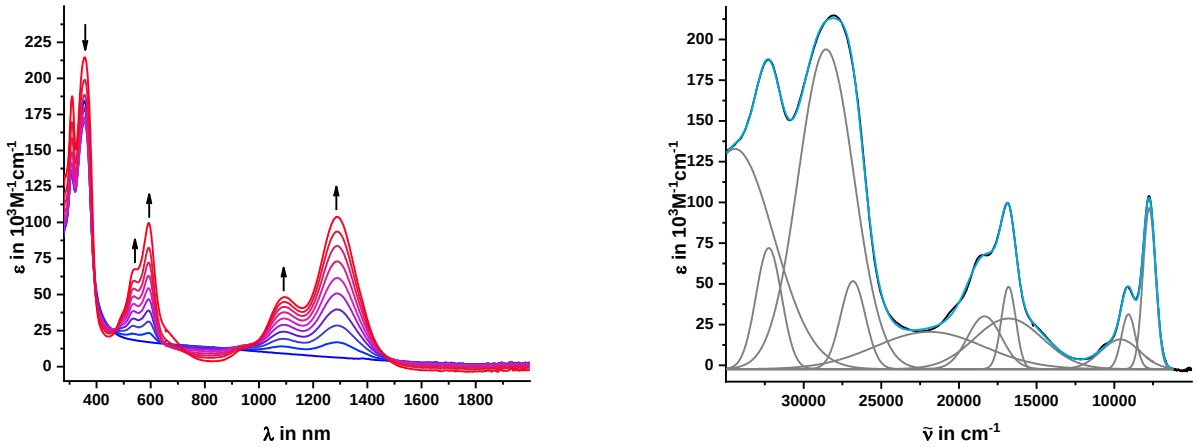

Figure S68. Changes in the UV/Vis/NIR spectra of **2-BTE**$^{2+}$ upon oxidation to **2-BTE**$^{4+}$ (left) and deconvolution (right), measured in CH_2Cl_2/^{n}Bu$_4$NPF$_6$.

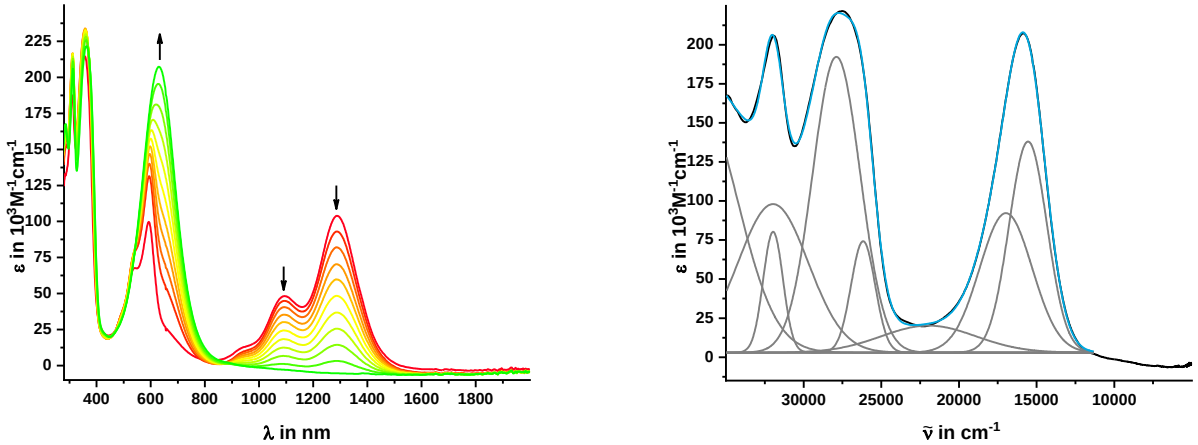

Figure S69. Changes in the UV/Vis/NIR spectra of **2-BTE**$^{2+}$ upon oxidation to **2-BTE**$^{4+}$ (left) and deconvolution (right), measured in CH_2Cl_2/^{n}Bu$_4$NPF$_6$.

Compound 2-BN:

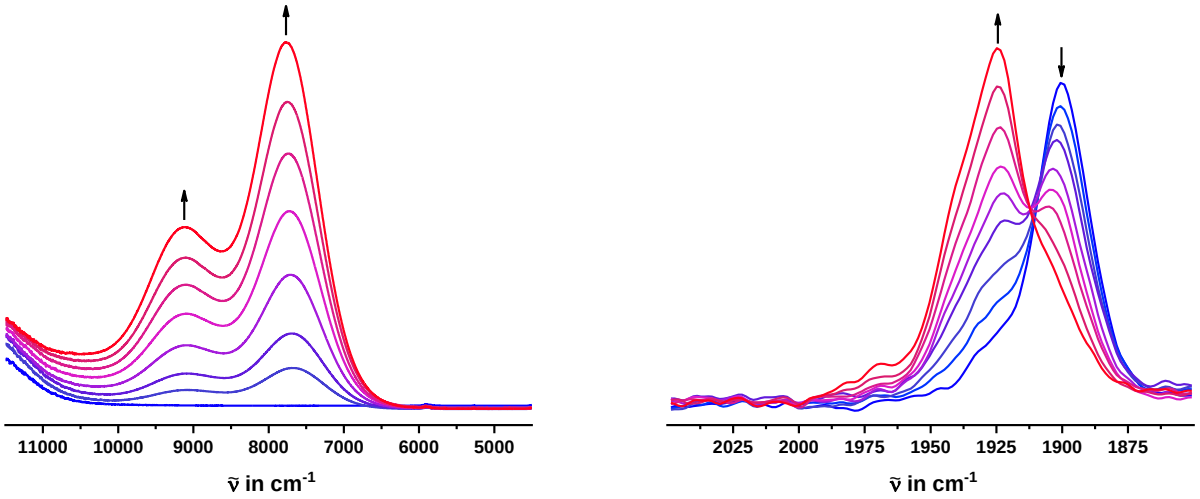

Figure S70. Changes in the IR spectra of **2-BN** upon oxidation to **2-BN**$^{2+}$, measured in $CH_2Cl_2/^nBu_4NPF_6$.

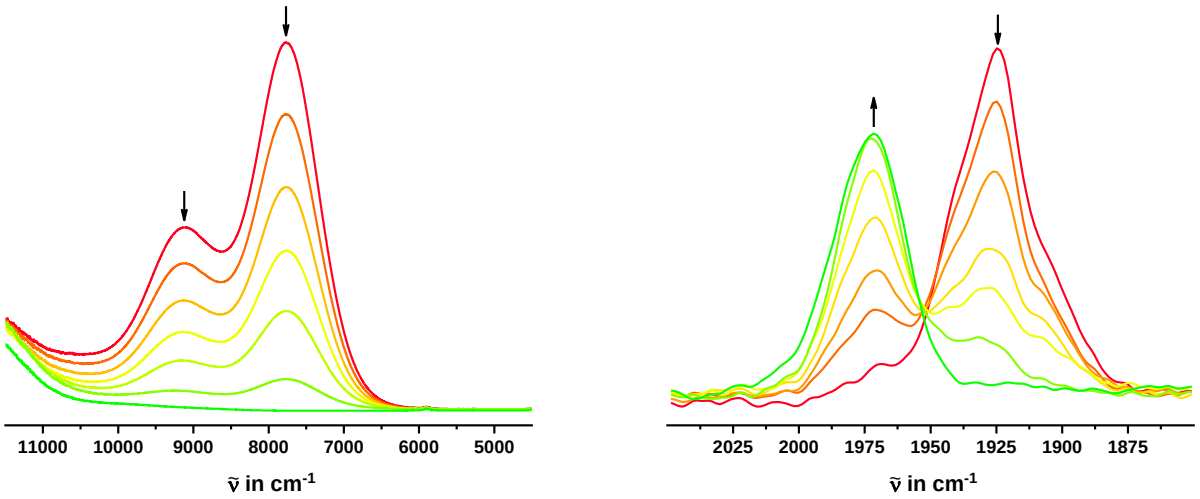

Figure S71. Changes in the IR spectra of **2-BN**$^{2+}$ upon oxidation to **2-BN**$^{4+}$, measured in $CH_2Cl_2/^nBu_4NPF_6$.

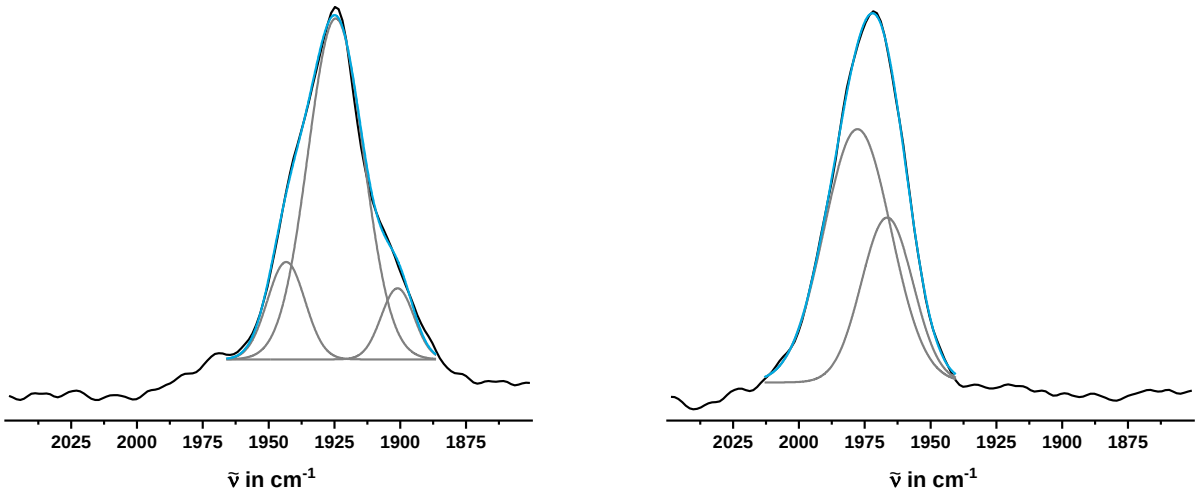

Figure S72. Deconvolutions of the Carbonyl bands of **2-BN**$^{2+}$ (left) and **2-BN**$^{4+}$ (right).

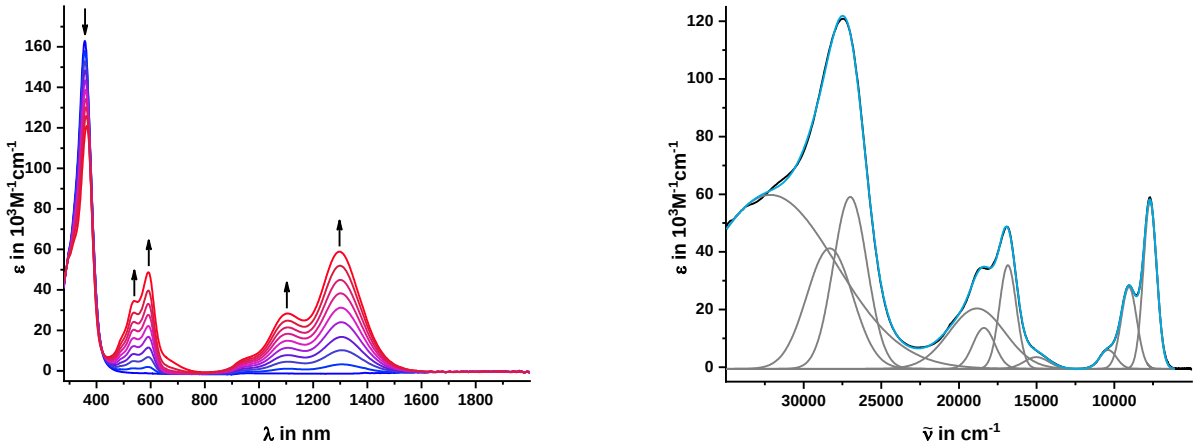

Figure S73. Changes in the UV/Vis/NIR spectra of **2-BN**$^{2+}$ upon oxidation to **2-BN**$^{4+}$ (left) and deconvolution (right), measured in CH_2Cl_2/^{n}Bu$_4$NPF$_6$.

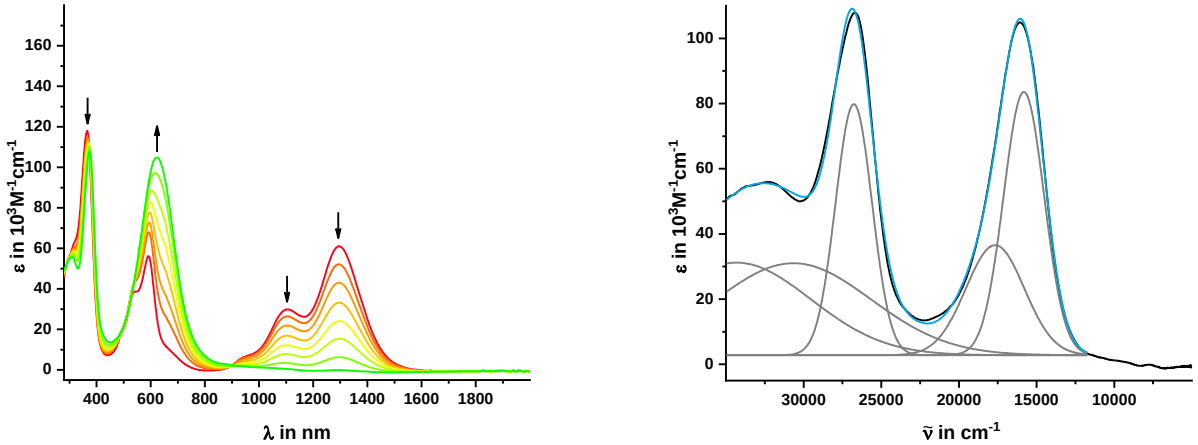

Figure S74. Changes in the UV/Vis/NIR spectra of **2-BN**$^{2+}$ upon oxidation to **2-BN**$^{4+}$ (left) and deconvolution (right), measured in CH_2Cl_2/^{n}Bu$_4$NPF$_6$.

Compound 2-NB:

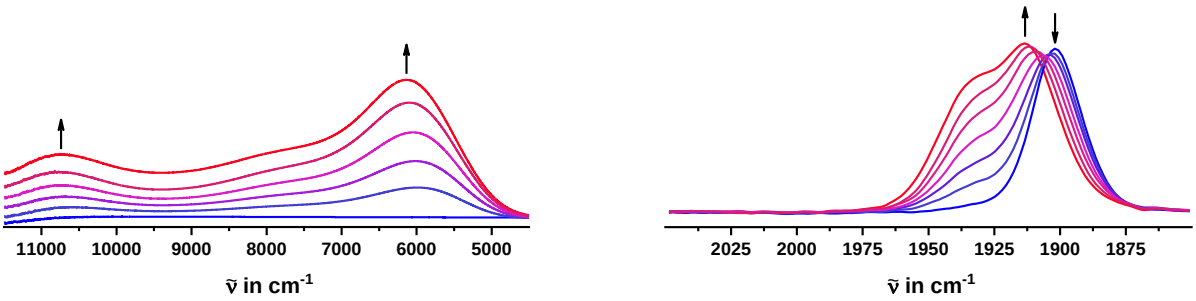

Figure S75. Changes in the IR spectra of **2-NB** upon oxidation to **2-NB**$^{2+}$, measured in $CH_2Cl_2/^nBu_4NPF_6$.

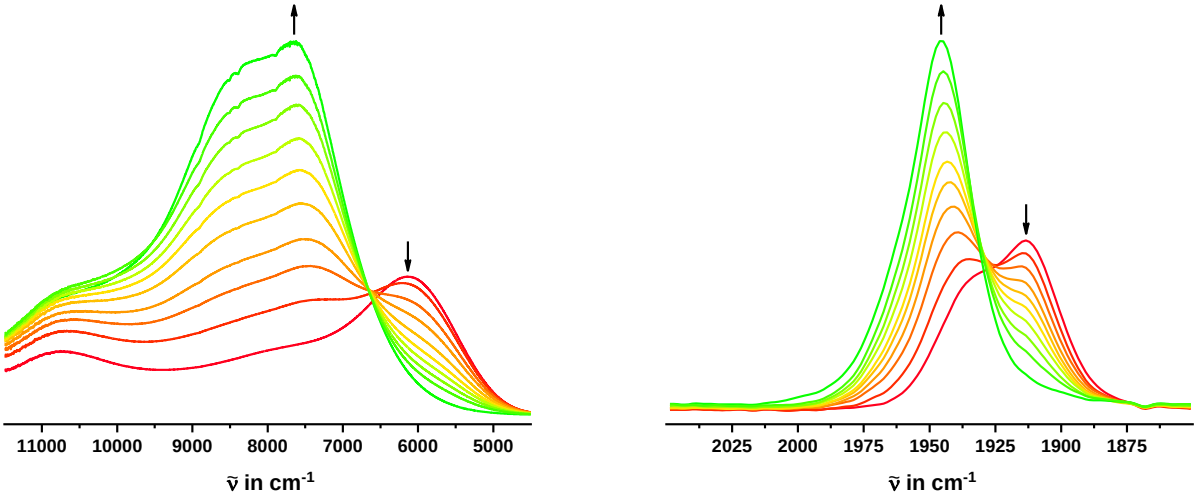

Figure S76. Changes in the IR spectra of **2-NB**$^{2+}$ upon oxidation to **2-NB**$^{4+}$, measured in $CH_2Cl_2/^nBu_4NPF_6$.

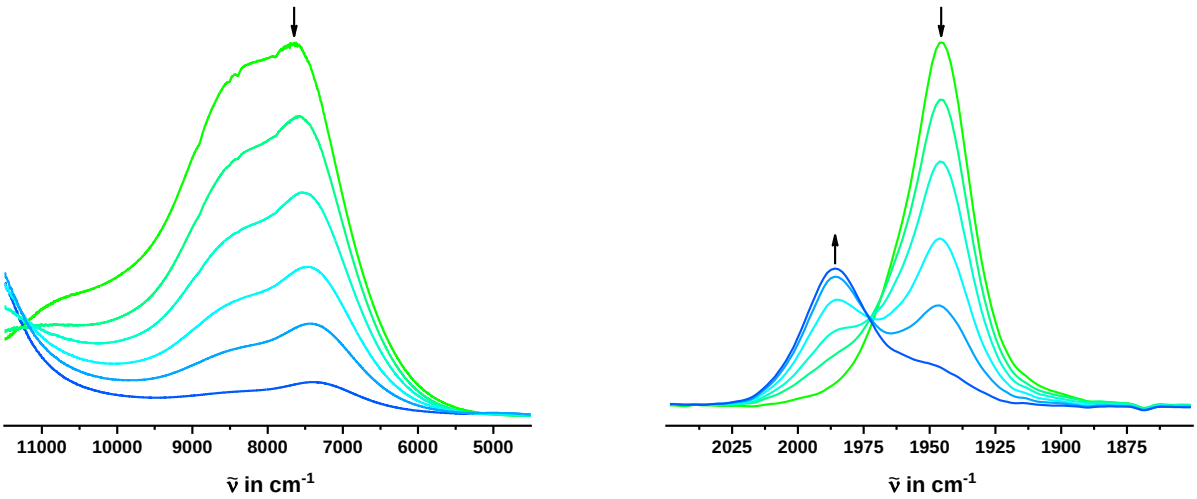

Figure S77. Changes in the IR spectra of **2-NB**$^{4+}$ upon oxidation to **2-NB**$^{6+}$, measured in $CH_2Cl_2/^nBu_4NPF_6$.

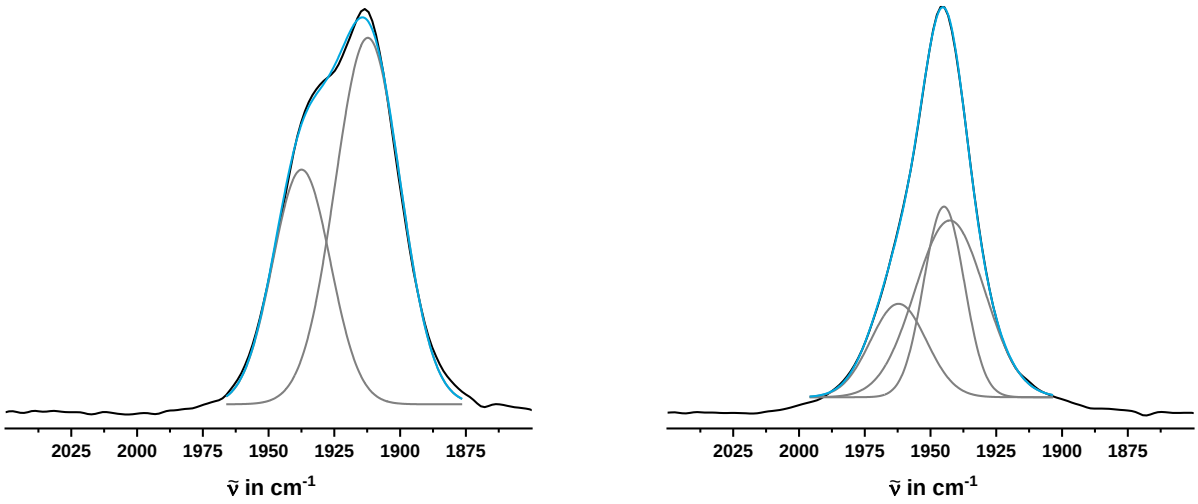

Figure S78. Deconvolutions of the Carbonyl bands of **2-NB**$^{2+}$ (left) and **2-NB**$^{4+}$ (right).

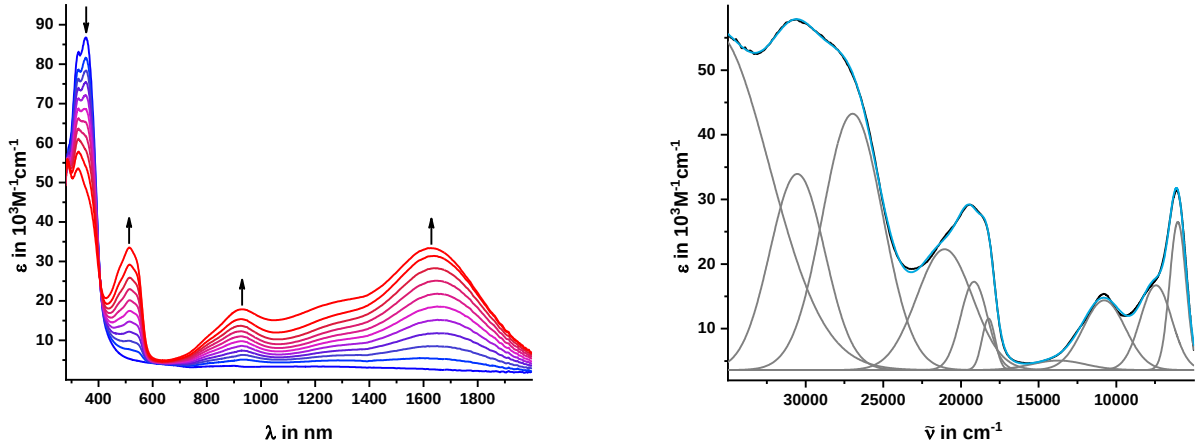

Figure S79. Changes in the UV/Vis/NIR spectra of **2-NB** upon oxidation to **2-NB**$^{2+}$ (left) and deconvolution (right), measured in CH_2Cl_2/^{n}Bu$_4$NPF$_6$.

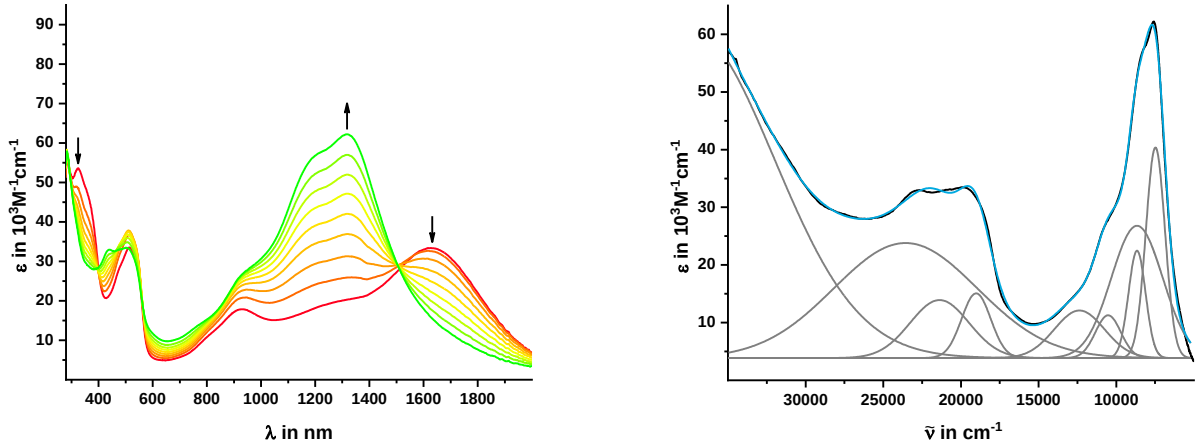

Figure S80. Changes in the UV/Vis/NIR spectra of **2-NB**$^{2+}$ upon oxidation to **2-NB**$^{4+}$ (left) and deconvolution (right), measured in CH_2Cl_2/^{n}Bu$_4$NPF$_6$.

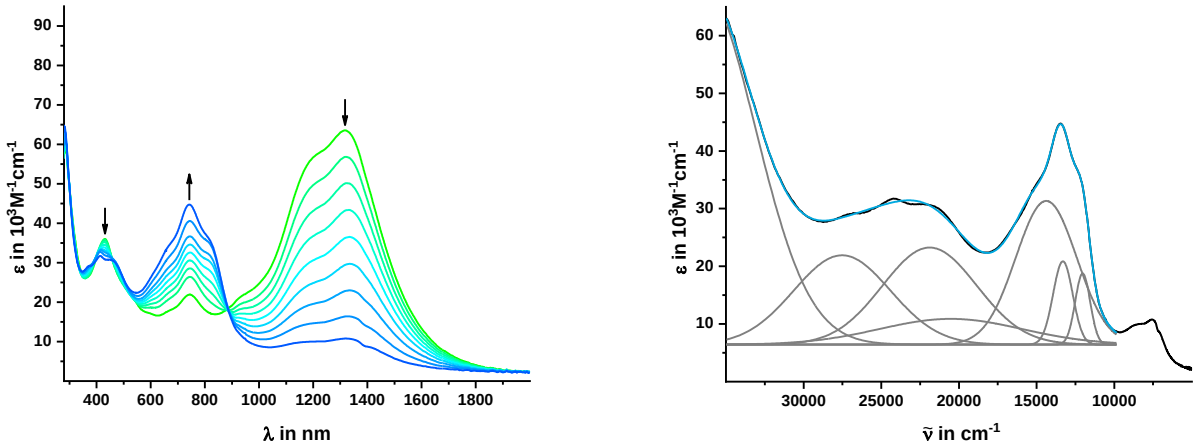

Figure S81. Changes in the UV/Vis/NIR spectra of **2-NB**$^{4+}$ upon oxidation to **2-NB**$^{6+}$ (left) and deconvolution (right), measured in CH_2Cl_2/^{n}Bu$_4$NPF$_6$.

EPR Spectroscopy

Compound 2-BT:

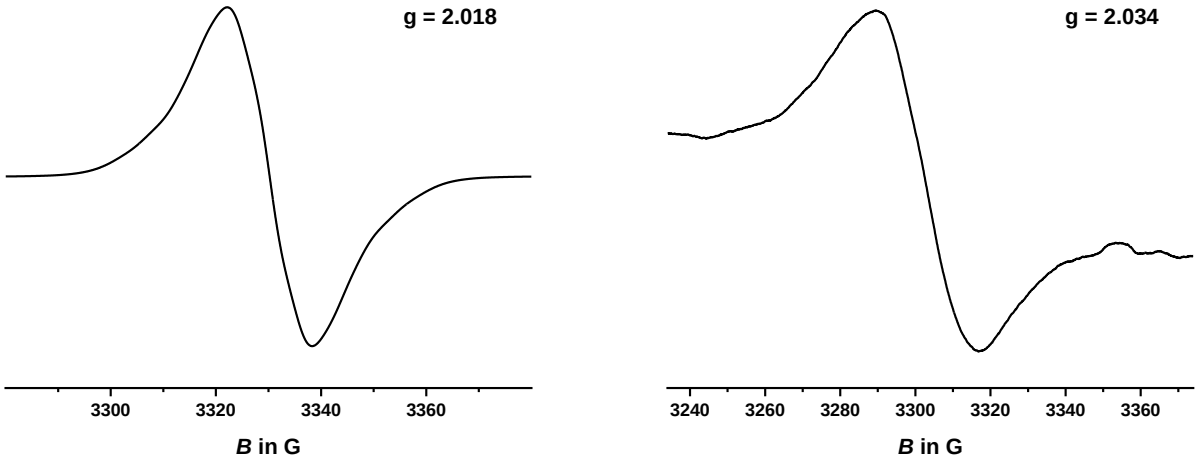

Figure S82. EPR spectra of **2-BT**$^{2+}$ (left) and **2-BT**$^{4+}$ (right) at room temperature.

Compound 2-BTO:

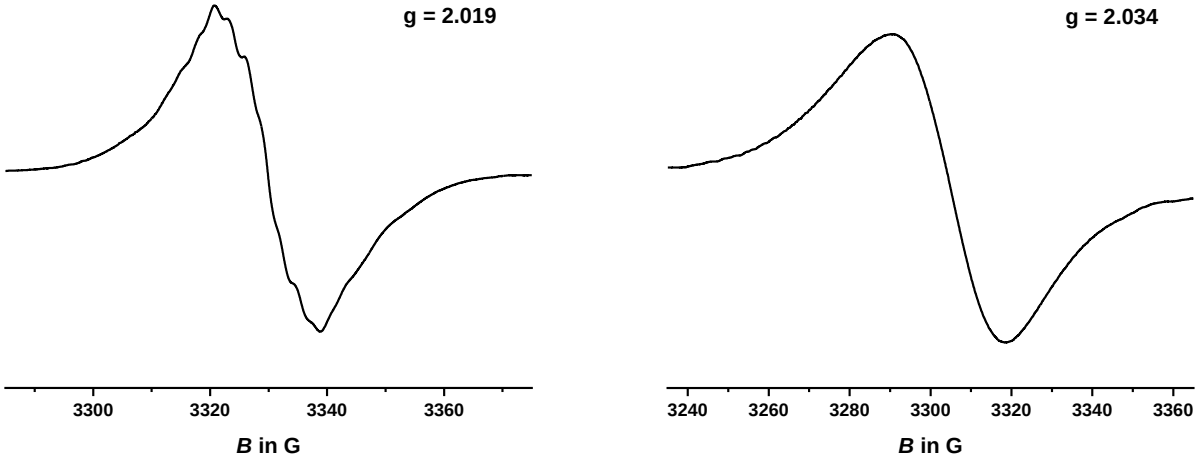

Figure S83. EPR spectra of **2-BTO**$^{2+}$ (left) and **2-BTO**$^{4+}$ (right) at room temperature.

Compound 2-BTE:

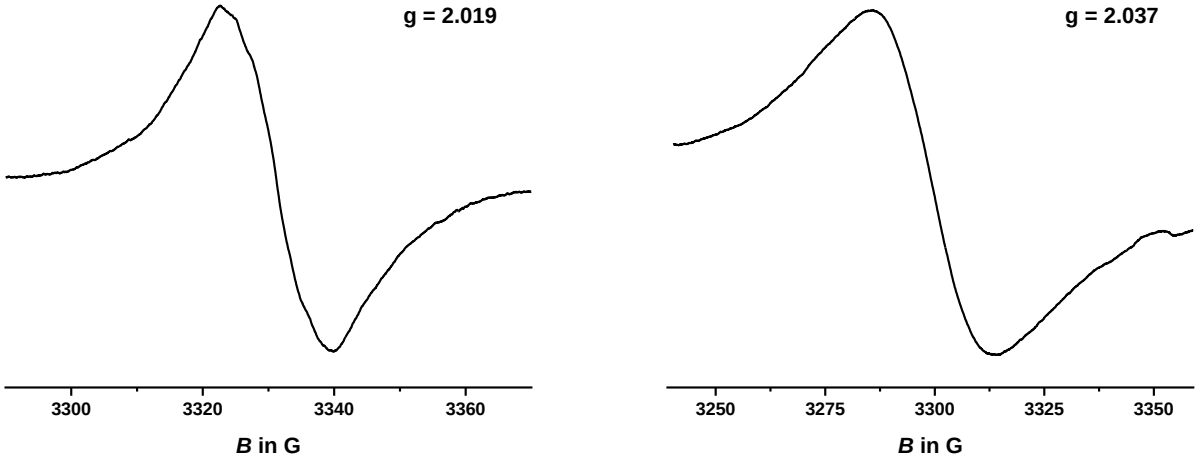

Figure S84. EPR spectra of **2-BTE**$^{2+}$ (left) and **2-BTE**$^{4+}$ (right) at room temperature.

Compound 2-BN:

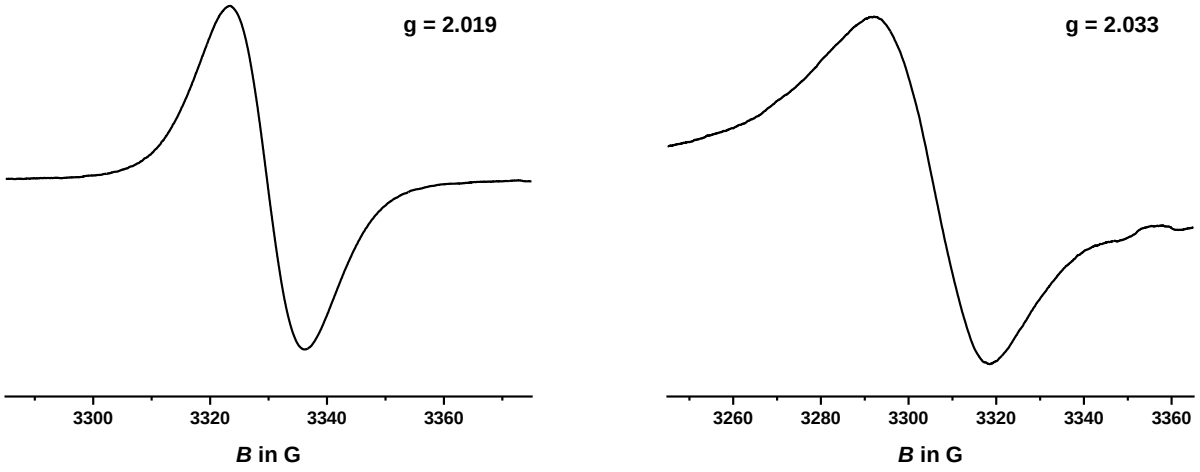

Figure S85. EPR spectra of **2-BN**$^{2+}$ (left) and **2-BN**$^{2+}$ (right) at room temperature.

Compound 2-NB

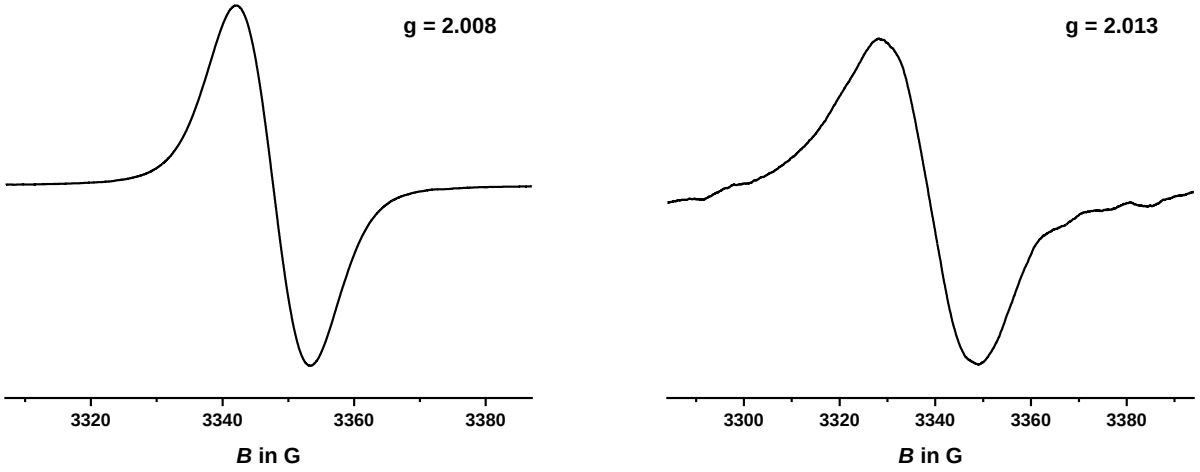

Figure S86. EPR spectra of **2-NB**$^{2+}$ (left) and **2-NB**$^{4+}$ (right) at room temperature.

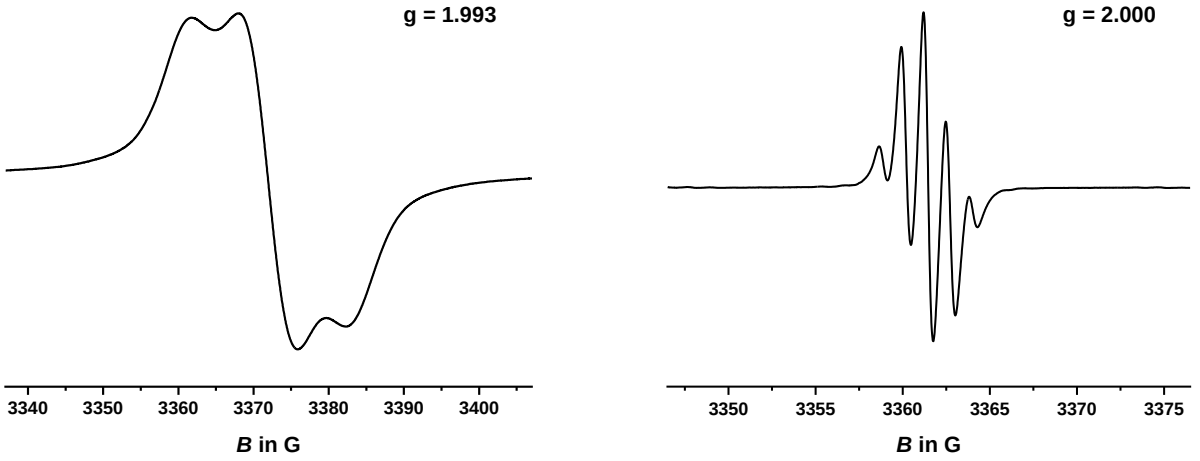

Figure S87. EPR spectra of **2-NB**$^{6+}$ (left) and of thianthrenium hexafluoroantimonate (right) at room temperature.

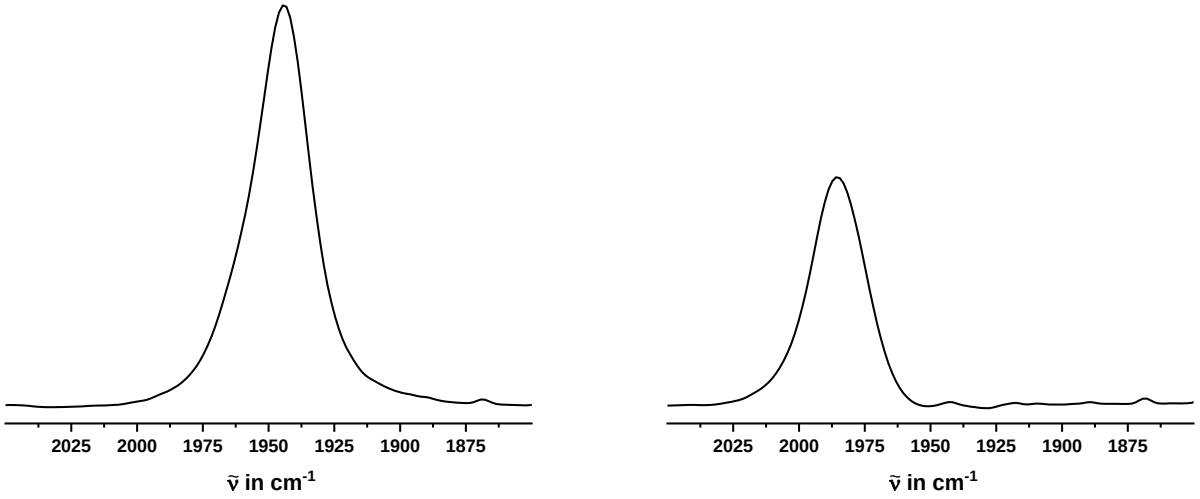

Figure S88. Carbonyl bands of **2-NB^{4+}** (left) and **2-NB^{6+}** (right) generated via chemical oxidation with the appropriate number of equivalents of thianthrenium hexafluoroantimonate in CH_2Cl_2.

References

(1) Dolomanov, O.V.; Bourhis, L. J.; Gildea, R. J.; Howard, J. A. K.; Puschmann, H. J. Appl. Cryst., **2009**, 42 (2), 339-341.

(2) Sheldrick, G.M. Acta Cryst. **2015**, A71, 3-8.

(3) Sheldrick, G.M. Acta Cryst. **2015**, C71, 3-8.